FAILURE CRITERIA FOR FUNCTIONALLY GRADED MATERIALS AND APPLICATION OF GTN MODEL USING FINITE ELEMENTS

by

Alpay Oral

B.S., M.E., Boğaziçi University, 2001

M.S., M.E., Boğaziçi University, 2003

Submitted to the Institute for Graduate Studies in
Science and Engineering in partial fulfillment of
the requirements for the degree of
Doctor of Philosophy

Graduate Program in Mechanical Engineering
Boğaziçi University
2010

To my father, Şeref Oral

ACKNOWLEDGEMENTS

I would like to express my gratitude to my thesis supervisor Prof. Günay Anlaş for his guidance, advice and endless goodwill during my study. I am also grateful to Prof. John Lambros for his significant support and guidance during my stay at the University of Illinois. It has been a pleasure to know them and to work with them.

I would like to thank to my thesis committee members, Dr. Cahit Can Aydıner, Dr. Nuri Ersoy, Dr. Hilmi Luş, and Dr. Ziad Moumni for their kind help.

The financial support of the Scientific and Technological Research Council of Turkey (TÜBİTAK) through research fellowship (code 2214) is greatly acknowledged. The support gave me an opportunity to do research at the University of Illinois at Urbana-Champaign.

I am also thankful to all faculty & staff members and students, who made my years at the Boğaziçi University unforgettable.

Special thanks and appreciation go to my dear wife Ayşe Hande Oral who said 'yes' and never looked back. I thank my mother Özgül Oral and my sister Elif Özlem Aydin for their endless support and for sharing my hopeless times during this study. Finally, there is one person that I missed longingly; my father Şeref Oral. He was and will always be in my heart.

ABSTRACT

FAILURE CRITERIA FOR FUNCTIONALLY GRADED MATERIALS AND APPLICATION OF GTN MODEL USING FINITE ELEMENTS

Functionally Graded Materials (FGMs) are special composites with a point to point continuous property variation. In this thesis, failure of laboratory scale FGMs is modeled using Gurson - Tvergaard - Needleman (GTN) model.

Stress, energy, strain based (e.g. MTS, G, S criteria) and cohesive zone models that are used for failure modeling of FGMs are reviewed. GTN model originally used for failure of homogeneous materials is studied in detail. Because it is extremely difficult, if not possible, to obtain a closed form GTN yield function for a non homogeneous material, numerical implementation of GTN model is considered, and Abaqus is used for computational analyses. The validity of results are first checked by resolving a problem from literature using Abaqus.

GTN model is numerically implemented to two different FGM specimens to study and predict failure. One of the FGM specimens is titanium monoboride / titanium (TiB / Ti) single edge notched bending (SENB) specimen, and the other one is a gradually ultraviolet irradiated polyethylene carbon monoxide (ECO) co-polymer single edge notched tension (SENT) specimen. It is concluded that GTN model is promising for failure simulations of FGMs with a proper selection of model parameters.

ÖZET

ÖZELLİKLERİ FONKSİYONEL OLARAK DEĞİŞEN MALZEMELER İÇİN HASAR KRİTERLERİ VE GTN MODELİNİN SONLU ELEMANLAR KULLANILARAK UYGULANMASI

Özellikleri fonksiyonel olarak değişen malzemeler (FGMs) bir noktadan diğer bir noktaya özellikleri sürekli değişim gösteren özel amaçlı kompozitlerdir. Bu tezde, laboratuvar ölçekli FGM'lerin hasarı Gurson - Tvergaard - Needleman (GTN) modeli kullanılarak modellenmiştir.

Özellikleri fonksiyonel olarak değişen malzemelerin hasar modellemesinde kullanılan gerilim, enerji, gerinim esaslı modeller (örneğin, MTS, G, S kriterleri) ve kohezif bölge modeli gözden geçirilmiştir. Orjinal olarak homojen malzemelerin hasarı için kullanılan GTN modeli detaylı bir şekilde çalışılmıştır. Homojen olmayan malzemeler için kapalı form GTN akma fonksiyonu elde edilmesi çok güç olduğundan, GTN modelinin nümerik olarak hesaplanmasına karar verilmiş ve sayısal analizlerde Abaqus kullanılmıştır. Abaqus ile elde edilen sonuçların doğruluğu literatürdeki bir problemin sonuçları ile karşılaştırılarak sınanmıştır.

GTN modelinin nümerik olarak uygulanması ile iki farklı tip FGM numunesinin hasarı çalışılmıştır. Bu numunelerden bir tanesi titanyum monoborit/titanyum (TiB / Ti) tek kenar çentikli eğilme numunesi, diğeri ise aşamalı olarak morötesi ışınımına maruz kalmış polietilen karbonmonoksit (ECO) kopolimer tek kenar çentikli çekme numunesidir. GTN modelinin uygun model parametrelerinin seçilmesi ile FGM'lerin hasar simülasyonlarında başarılı olduğu sonucuna varılmıştır.

TABLE OF CONTENTS

LIST OF FIGURES

LIST OF TABLES

LIST OF SYMBOLS/ABBREVIATIONS

E	Young's modulus
E_{cer}	Young's modulus of ceramic phase
E_{FGM}	Young's modulus of FGM
E_{met}	Young's modulus of metal phase
$\dot{E}_{ij}$	Macroscopic strain rate components
f	Void volume fraction
f_0	Initial void volume fraction
f_c	Critical void volume fraction
f_F	Failure void volume fraction
f_n	Volume fraction of void nucleating particles
f_U	Ultimate void volume fraction
G	Shear modulus
n	Power hardening exponent
$q_{1,2,3}$	Pressure sensitive yield function coefficients
s_n	Standard deviation for void nucleation
T_{ij}	Normalized macroscopic stress components
V_{cer}	Volume fraction of ceramic phase
V_{met}	Volume fraction of metal phase
v_i	Velocity components
$\dot{W}$	Dissipation energy
w_Φ	Weight for objective function Φ_3
w_ϕ	Weight for objective function ϕ_3
δ_{ij}	Kronecker delta
ϵ_n	Mean nucleation strain
$\dot{\epsilon}_{ij}$	Microscopic strain rate components
$\dot{\epsilon}'_{ij}$	Microscopic deviatoric strain rate components
$\dot{\epsilon}^P_{eqv}$	Equivalent plastic strain rate
ρ	Density

Σ'_{ij}	Macroscopic deviatoric stress components
Σ_{eqv}	Macroscopic equivalent stress
Σ_h	Macroscopic hydrostatic stress
σ_{ij}	Microscopic stress components
σ'_{ij}	Microscopic deviatoric stress components
σ_0	Initial yield stress
σ_Y	Current flow stress
$\Phi_{1,2,3}$	Objective functions for tensile, fracture, and both tests together (difference between squares of variables)
$\phi_{1,2,3}$	Objective functions for tensile, fracture, and both tests together (least squares sense)
$\phi_{cylindrical}$	Pressure sensitive yield function for a cylindrical void
$\phi_{spherical}$	Pressure sensitive yield function for a spherical void

CMOD	Crack mouth opening displacement
FGM	Functionally graded material
GTN	Gurson-Tvergaard-Needleman

1. INTRODUCTION

Metal-ceramic composites usually in the form of ceramic coatings on metals are designed to benefit from heat, oxidation, wear and corrosion resistance of ceramics, and to benefit from the toughness and strength of metals. But, due to a distinct interface between metal and ceramic components, such composites are vulnerable to failure because of high residual stresses and poor interfacial bonding caused by the interfacial mismatch. This problem is tried to be overcome by varying material properties gradually from metal to ceramic. This continuous change in properties improves the thermal and mechanical behaviors of the system. Materials that have a continuous change of properties from one point to another with a specific gradient are called functionally graded materials (FGMs). FGMs are therefore special composites, and they may be used in applications involving severe thermal gradients, high wear such as aerospace engine components, cutting tools and electronic circuit boards. The behavior of FGMs under different loading conditions should be well understood. In the following literature review, studies on failure of FGMs which will be the main scope of the dissertation is summarized.

1.1. Literature Review

Researchers studied fracture of functionally graded materials for different geometries and loading conditions analytically, numerically and experimentally. Early studies on fracture of FGMs were mainly focused on obtaining crack-tip stress and displacement fields and stress intensity factors analytically and/or numerically [1–6]. Crack propagation directions of pre-cracked specimens which is a mode of failure were widely investigated. There are many criteria that were proposed for homogeneous materials to predict propagation direction of an existing crack. They are implemented to functionally graded materials in [7–11]. Those criteria can be grouped under three main groups: *i*) energy-based criteria, *ii*) stress-based criteria and *iii*) strain-based criteria. For all criteria the critical condition refers to one of the extremum of the stated parameter, i.e., stress, energy, or strain. The toughness of the material are also varying within FGMs as a result of nonhomogeneity. This is not taken into account by any of these criteria. For example, the toughness can be maximum where the maximum tangential stress occurs around the crack-tip. Therefore, failure may be mispredicted by directly using failure models cited above.

A different technique to simulate failure is the use of so-called cohesive zone modeling implemented to finite element method. The basis of cohesive zone models was founded on the works of Barenblatt [12, 13] and Dugdale [14]. Barenblatt assumed that there are atomic cohesive traction and the magnitude of the traction depends on the new free surface opening displacement due to failure. Dugdale used a similar cohesive zone model but he considered the traction to be constant and invariant with crack opening. The traction produces a closure and they can occur in normal and shear directions. Cohesive zone elements do not represent any physical material, but describe cohesive forces that occur when material elements are being pulled. Cohesive zone elements are placed between continuum (bulk) elements, as shown in Figure 1.1. When the body is loaded, these cohesive zone elements open in order to simulate failure in the body. Since the failure path can only follow these elements, failure strongly depends on the presence of cohesive zone elements. Therefore, failure is mesh dependent, but refining the mesh reduces this problem.

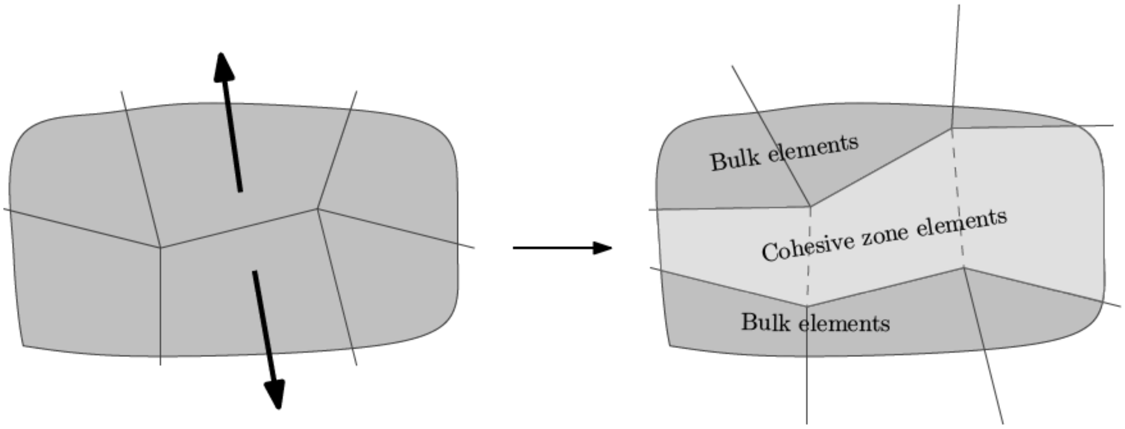

Figure 1.1. Cohesive zone elements in bulk elements

Cohesive zones simulate damage mechanisms in a specimen, leading to a cohesive zone law between the traction and opening displacement. These laws are; *i*) polynomial cohesive zone laws, *ii*) piece-wise linear cohesive zone laws, *iii*) exponential cohesive zone laws, and *iv*) rigid-linear cohesive zone laws as shown in Figure 1.2 [15]. The maximum traction is the cohesive strength (separation stress), and the area under the traction and opening displacement curve is the cohesive energy. As the cohesive surfaces separate, the traction first increases until a maximum is reached, and subsequently the traction decreases to zero, that results in local separation. This holds for both normal and tangential directions. The initial stiffness of the cohesive zone model has a large influence on the overall elastic deformation and should be very high in order to obtain realistic results.

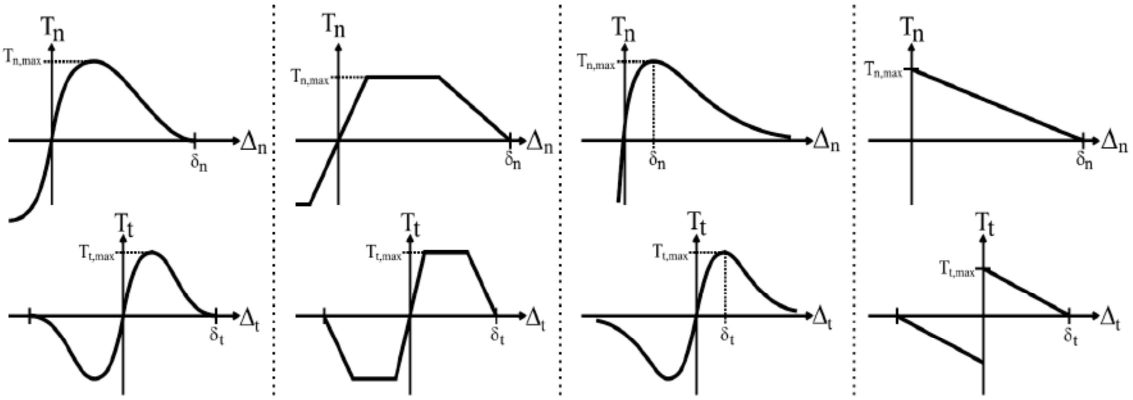

(a) (b) (c) (d)

Figure 1.2. (a) Polynomial, (b) piece-wise linear, (c) exponential, (d) rigid-linear cohesive zone laws. Cohesive zone laws for normal and tangential directions in upper and lower rows, respectively [15]

Cohesive zone models are also used for functionally graded materials to study failure in FGMs. Tvergaard [16], studied the crack growth in a functionally graded material with linearly varying material properties between two dissimilar elastic–plastic homogeneous solids. His analysis is based on the assumption that crack growth remains on the initial crack plane, which is parallel to functionally graded interface layer. Crack growth resistance curves and the dependence of the steady–state fracture toughness on mode–mixity are obtained for different material variations and crack locations. Jin *et al.* [17, 18] developed a new volume-fraction-based cohesive zone model for FGMs. They studied quasi-static Mode-I crack growth for compact-tension and single edge-bending specimens using finite elements. They calibrated cohesive parameters using experimentally measured load vs. crack extension response. Wang and Nakamura [19] proposed a power law relationship between separation energy and separation stress. The feasibility of the model was examined in a dynamic fracture analysis of an FGM double cantilever beam (DCB) specimen. Then, the proposed criterion was implemented to a more complex model: A functionally graded protective layer on a substrate subjected to a high velocity rod impact was considered causing multiple crack initiations and propagations. They investigated the influence of material gradation on energy absorption. Zhang and Paulino [20] studied dynamic fracture behavior of homogeneous and functionally graded materials. They obtained fracture path and crack propagation speeds using finite elements for an edge–cracked FGM beam and for an FGM plate with two edge notches under impact loading. The former was under Mode-I loading and the latter was under mixed-mode loading. A good agreement was observed between numerical and experimental results. Kandula *et al.* [21, 22] examined dynamic and quasi-static fracture of functionally graded materials under Mode-I loading. Numerical model is validated with experimental results for an edge cracked specimen by comparing the time evolution of crack tip location under dynamic loading. Then, a parametric study of dynamic failure of a titanium monoboride / titanium (TiB / Ti) FGM was performed by Kandula *et al.* [21] using cohesive zone model. A great sensitivity of the crack motion to the gradient of the cohesive failure parameters between the metallic and the ceramic components was observed in [21]. Kandula *et al.* [22] obtained reaction force and crack extension as a function of applied displacement using cohesive zone model for a gradually ultraviolet irradiated polyethylene carbon monoxide co-polymer (laboratory scale FGM) single edge tension specimen under quasi-static loading. Computational results for different cohesive zone parameters were compared to the experimental results given by Abanto-Bueno [23], and a reasonable agreement was obtained.

The main drawbacks of using cohesive zone elements in modeling failure can be listed as follows:

- Direction of failure propagation strongly depends on where the cohesive zone elements exist.
- Mesh dependency.

- Artificial compliance along element boundary is introduced [19, 20].
- Cohesive zone law fails to provide predictions when peak separation stress is too high when compared with yield stress [19].
- Crack-tip stress singularity weakens due to cohesive surface separation [20].
- Cohesive zone law needs improvement in order to describe a mixed-mode decohesion process [20].

So called the Gurson - Tvergaard - Needleman (GTN) failure model used for homogeneous materials originally developed by Gurson [24, 25], then by Tvergaard and Needleman [26–28]. GTN model that predicts failure as a result of void nucleation, growth and coalescence, is a more physically based model. Pressure sensitive yield functions developed by Gurson [24, 25] for cylindrical and spherical voids are as follows:

$$\Phi_{cylindrical} = \frac{\Sigma_{eqv}^2}{\sigma_Y^2} + 2f\cosh\left(\frac{\sqrt{3}\Sigma_{11}}{\sigma_Y}\right) - 1 - f^2 = 0 \text{ (for axisymmetry)}, \quad (1.1a)$$

$$\Phi_{spherical} = \frac{\Sigma_{eqv}^2}{\sigma_Y^2} + 2f\cosh\left(-\frac{3}{2}\frac{\Sigma_h}{\sigma_Y}\right) - 1 - f^2 = 0 \quad (1.1b)$$

respectively, where f is void volume fraction, σ_Y is tensile flow stress in matrix material, Σ_{11} is macroscopic radial stress in symmetry plane,

$$\Sigma_{eqv} = \left(\frac{3}{2}\Sigma'_{ij}\Sigma'_{ij}\right)^{1/2}, \quad (1.2a)$$

$$\Sigma_h = -\frac{\Sigma_{11} + \Sigma_{22} + \Sigma_{33}}{3}, \quad (1.2b)$$

$$\Sigma'_{ij} = \Sigma_{ij} - \delta_{ij}\frac{\Sigma_{kk}}{3}. \quad (1.2c)$$

Σ_{eqv}, Σ_h, Σ'_{ij} are macroscopic equivalent von Mises, hydrostatic and deviatoric stresses, respectively. Detailed derivations of these yield functions are given in chapter 2. Stress carrying capacity vanishes ($\Sigma_{eqv} = \Sigma_h = \Sigma_{11} = 0$) when $f = 1$, and yield functions simplify to von Mises yield function when $f = 0$. Stress responses for different void volume fractions are plotted in Figures 1.3 (a)-(b) for cylindrical and spherical voids. Stress carrying capacity decreases with increasing void volume fraction. Modifications to the yield functions in Equations 1.1a-b and void volume fraction evolution laws are proposed by Tvergaard and Needleman [26–28] and are explained in detail section 2.3.

In literature, there are numerous studies on predicting failure using GTN model. Therefore, some of the milestones in the use of GTN model are summarized here in chronological order. The first attempt that uses GTN model is a numerical analysis of failure in a round tensile test specimen [28] where failure initiates at the center of the specimen, and grows in a zig-zaged path. Stress-strain response, deformed shape and void volume fraction variation are evaluated. The first numerical implementation of GTN model to a fracture mechanics problem is introduced by Aoki *et al.* [29]. In their study, effects of microvoids on crack blunting and extent of the HRR field (elastic-plastic stress field in power hardening materials developed by Hutchinson-Rice-Rosengren) are investigated. Aravas and McMeeking [30] attracted attention on the choice of GTN model parameters, and estimated crack-tip opening displacement at fracture initiation for a blunting crack with a cylindrical void ahead. Aravas [31] presented an unconditionally stable Euler backward scheme for numerical integration of GTN model equations. Sun *et al.* [32] predicted load-displacement responses of notched round tensile specimens. Then, J-resistance curves were obtained for a compact tension fracture specimen using the GTN model parameters obtained from tensile tests. It was noted that using GTN model for simulation of larger crack growth was difficult due to great distortion of the elements at the crack-tip. First implementation of GTN model using 3D finite elements was done for simulation of failure of crack growth in a three point bending steel specimen by Narasimhan *et al.* [33]. Crack tunneling was well predicted in numerical analysis when the void volume fraction variation was examined through specimen thickness. Xia and Shih [34, 35] suggested the use GTN model together with finite elements in front of the crack by a layer of similarly-sized elements to simulate crack growth which are called computational cells. The size of these elements were chosen to be in the order of the crack-tip opening displacement. Effects of initial void volume fraction, power hardening exponent and initial yield strain on opening stresses and fracture resistance curves were studied. Kuna and Sun [36] compared the numerical results obtained by three dimensional primitive cubic, body centered cubic and hexagonal unit cell models under constant triaxial stresses

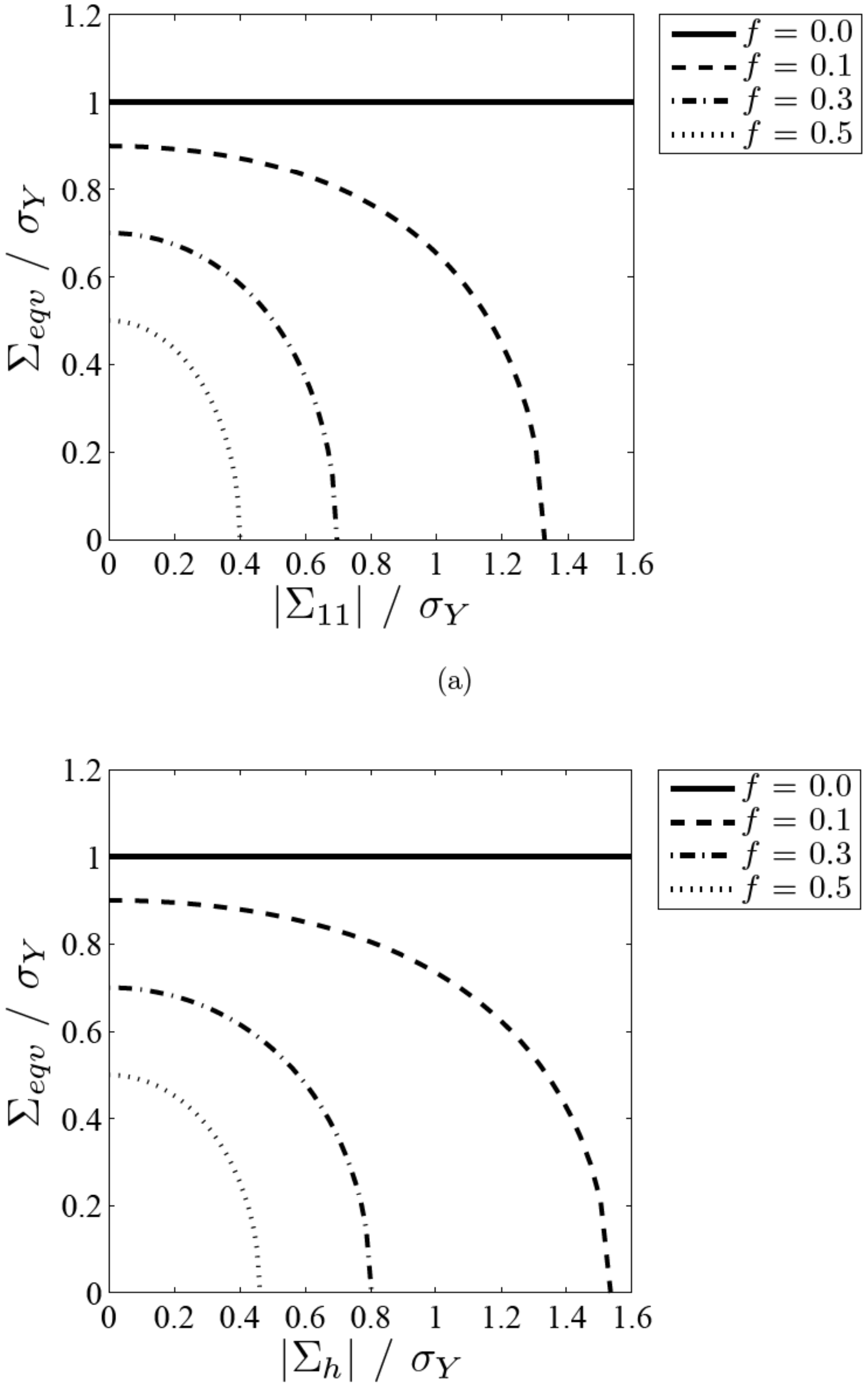

(a)

(b)

Figure 1.3. Gurson yield functions (a) for a cylindrical void, and (b) for a spherical void, plotted using Equations 1.1a and 1.1b

(hydrostatic stress/equivalent von Mises stress) with the results obtained by GTN model. Then, GTN model parameters were calibrated accordingly for these different unit cell models. First sensitivity analysis for GTN model parameters were carried out by Zhang [37] where selection of GTN model parameters and non-uniqueness problem of GTN model parameters are emphasized. Up to mid-'90s, GTN model was generally used for modeling failure of ferrous alloys. Pardeon *et al.* [38] studied the failure of tensile bars numerically and experimentally with different notch radii made of copper rather than ferrous alloys to figure out the effect of stress triaxiality. Many researchers still study GTN model for improving the model capabilities and for simulating failure of different type of materials under various loading conditions.

1.2. Scope of the Dissertation

The objective of this study is to model failure of functionally graded materials (FGMs) using the damage model originally proposed by Gurson [24, 25], and then developed by Tvergaard and Needleman [26–28]. An attempt to develop a pressure sensitive yield function for a non-homogeneous medium in closed form analytically similar to the one developed by Gurson [24, 25] for homogeneous materials is presented and discussed in chapter 2. As a result of difficulties encountered in such a closed form formulation, computational implementation of Gurson - Tvergaard - Needleman (GTN) model is considered and used.

Abaqus has a built-in GTN failure simulation module. In chapter 3, GTN model parameters that are required for use of Abaqus are summarized, and effects of these parameters on stress - strain response of a uniaxial tensile specimen are discussed. In the same chapter, a three point bending of a steel specimen problem from literature is revisited for verification of the results obtained using finite elements. Mesh size dependency of this module is discussed in the same chapter.

In chapter 4, failure of two different types of FGM specimens are studied. One of these specimens is titanium monoboride / titanium (TiB / Ti) FGM single edge notched bending specimen which was investigated by Jin *et al.* [17, 18] using cohesive zone model. The other one is gradually ultraviolet irradiated polyethylene carbon monoxide co-polymer (laboratory scale FGM) single edge notched tension specimen which was studied experimentally by Abanto-Bueno [23] and numerically (cohesive zone model) by Kandula *et al.* [22]. The failure of these specimens are studied in detail computationally using GTN model, and the results are compared to numerical and experimental ones that are available. In the last chapter, the outcomes of this study are summarized and discussed.

2. GURSON YIELD FUNCTIONS

In the following sections, Gurson yield functions are derived in detail for cylindrical and spherical voids [24, 25]. Modifications for the yield function and evolution laws for void volume fraction that are proposed by Tvergaard and Needleman [26–28] are discussed. A derivation of pressure sensitive yield function for FGMs similar to the one obtained by Gurson [24, 25] for a cylindrical void is presented and the difficulties in obtaining a closed form solution are explained.

Voids are formed either by grain boundary misfits caused by straining or by accident through faulty processing. Gurson [24, 25] developed yield functions for cylindrical and spherical voids in a ductile medium. The yield functions are derived in detail for a long circular cylindrical void, and for a spherical void separately in a homogeneous plastic material in this section. Derivations are handled using a continuum approach even in the presence of a void within the body. Yield functions are obtained in terms of stresses and void volume fraction, but resulting yield surfaces are not functions of only equivalent von Mises stress, but also of hydrostatic stress although the common belief in classical plasticity is that plastic yielding is independent of hydrostatic stress. The yield function for spherical voids is extensively used for homogeneous ductile metallic materials literature [28–33].

The yield and flow relations of the matrix material are:

$$\begin{aligned}
\frac{3}{2}\sigma'_{ij}\sigma'_{ij} &= \sigma_Y^2, && (2.1)\\
\sigma'_{ij}(\dot{\boldsymbol{\epsilon}}) &= \frac{\sqrt{\frac{2}{3}}\sigma_Y\dot{\epsilon}_{ij}}{(\dot{\epsilon}_{kl}\dot{\epsilon}_{kl})^{1/2}} \quad \text{(Prandtl-Reuss relation-See Appendix A)}, && (2.2)\\
\dot{\epsilon}_{ij} &= \frac{1}{2}\left(\frac{\partial v_i}{\partial x_j}+\frac{\partial v_j}{\partial x_i}\right), && (2.3)\\
\dot{\epsilon}_{kk} &= 0. && (2.4)
\end{aligned}$$

where σ_Y is the tensile flow stress in the matrix material, σ'_{ij} is the microscopic deviatoric stress field that is $\sigma'_{ij} = \sigma_{ij} - \delta_{ij}\dfrac{\sigma_{kk}}{3}$, $\dot{\epsilon}_{ij}$ is the microscopic strain rate field and v_i is the velocity field.

2.1. Long Circular Cylindrical Voids

The geometry of a cylindrical void is similar to a long hollow cylinder as shown in Figure 2.1.

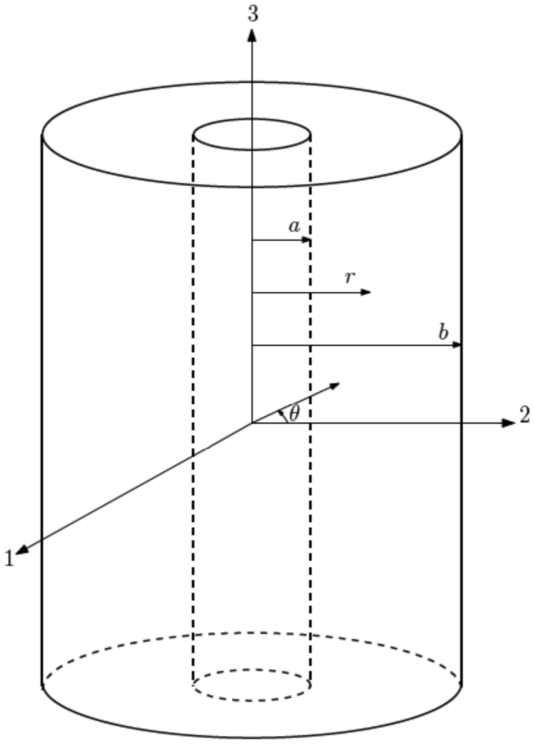

Matrix material is between a and b.

Figure 2.1. Long circular cylindrical void geometry

The velocity and the resulting strain rate fields are seperated into three separate parts for purpose of analysis; they are:

(i) Plane strain,
(ii) Uniform axial deformation,
(iii) General dilatation.

Velocity and strain rate fields for each part are derived separately in the following sections:

2.1.1. Plane Strain

The plane strain problem with no volumetric change ($\dot{\epsilon}_{kk} = 0$) is presented in this section. An angular dependence is assumed for stresses and velocities, and they can be written as

$$\sigma_{rr} = \bar{\sigma}_{rr}\ \cos(2\theta), \tag{2.5a}$$

$$\sigma_{\theta\theta} = \bar{\sigma}_{\theta\theta}\ \cos(2\theta), \tag{2.5b}$$

$$\sigma_{r\theta} = \bar{\sigma}_{r\theta}\ \sin(2\theta), \tag{2.5c}$$

$$v_r = \bar{v}_r\ \cos(2\theta), \tag{2.5d}$$

$$v_\theta = \bar{v}_\theta\ \sin(2\theta) \tag{2.5e}$$

where barred quantities depend only on r. Field equations will be obtained in terms of barred quantities. Equilibrium equations along r and θ are

$$\frac{\mathrm{d}\bar{\sigma}_{rr}}{\mathrm{d}r} + \frac{\bar{\sigma}_{rr} - \bar{\sigma}_{\theta\theta}}{r} + \frac{2\bar{\sigma}_{r\theta}}{r} = 0, \tag{2.6a}$$

$$\frac{\mathrm{d}\bar{\sigma}_{r\theta}}{\mathrm{d}r} + \frac{2(\bar{\sigma}_{r\theta} - \bar{\sigma}_{\theta\theta})}{r} = 0. \tag{2.6b}$$

Incompressibility relation is ($\cos(2\theta)$ terms drop)

$$\bar{\dot{\epsilon}}_{rr} + \bar{\dot{\epsilon}}_{\theta\theta} = \frac{\mathrm{d}\bar{v}_r}{\mathrm{d}r} + \frac{2\bar{v}_\theta + \bar{v}_r}{r} = 0, \tag{2.7}$$

and two constitutive relations are

$$\bar{\sigma}_{\theta\theta} - \bar{\sigma}_{rr} = 2G\left(\frac{2\bar{v}_\theta + \bar{v}_r}{r} - \frac{\mathrm{d}\bar{v}_r}{\mathrm{d}r}\right), \tag{2.8a}$$

$$\bar{\sigma}_{r\theta} = G\left(\frac{\mathrm{d}\bar{v}_\theta}{\mathrm{d}r} - \frac{2\bar{v}_r + \bar{v}_\theta}{r}\right) \tag{2.8b}$$

where G is shear modulus. Constitutive relations, Equations 2.8a and 2.8b are substituted into equilibrium equations along r and θ axes (Equations 2.6a and 2.6b) using incompressibility relation, Equation 2.7, and the following ordinary differential equation in terms of $\bar{v}_r$ is obtained.

$$r^4\frac{\mathrm{d}^4\bar{v}_r}{\mathrm{d}r^4}+6r^3\frac{\mathrm{d}^3\bar{v}_r}{\mathrm{d}r^3}-3r^2\frac{\mathrm{d}^2\bar{v}_r}{\mathrm{d}r^2}-9r\frac{\mathrm{d}\bar{v}_r}{\mathrm{d}r}+9\bar{v}_r=0. \tag{2.9}$$

The general solution for Equation 2.9 is

$$\bar{v}_r=C_1r^3+C_2r+C_3r^{-1}+C_4r^{-3} \tag{2.10}$$

where C_i are constants. $\bar{v}_\theta$ is obtained as shown below substituting Equation 2.10 into Equation 2.7:

$$\bar{v}_\theta=-2C_1r^3-C_2r+C_4r^{-3}. \tag{2.11}$$

Combining Equations 2.10, 2.11 with Equations 2.5d and 2.5e, approximate velocities v_r and v_θ under plane stress conditions are obtained.

$$v_r=(C_1r^3+C_2r+C_3r^{-1}+C_4r^{-3})\cos(2\theta), \tag{2.12a}$$

$$v_\theta=(-2C_1r^3-C_2r+C_4r^{-3})\sin(2\theta). \tag{2.12b}$$

The resulting strain rate field is

$$\begin{aligned}\dot{\epsilon}_{rr} = \bar{\dot{\epsilon}}_{rr}\cos(2\theta) &= \frac{\partial v_r}{\partial r} = \frac{\mathrm{d}\bar{v}_r}{\mathrm{d}r}\cos(2\theta) \\ &= (3C_1 r^2 + C_2 - C_3 r^{-2} - 3C_4 r^{-4})\cos(2\theta), \end{aligned} \tag{2.13a}$$

$$\begin{aligned}\dot{\epsilon}_{\theta\theta} = \bar{\dot{\epsilon}}_{\theta\theta}\cos(2\theta) &= \frac{1}{r}\frac{\partial v_\theta}{\partial \theta} + \frac{v_r}{r} = \left(\frac{2\bar{v}_\theta}{r} + \frac{\bar{v}_r}{r}\right)\cos(2\theta) = -\dot{\epsilon}_{rr} \\ &= (-3C_1 r^2 - C_2 + C_3 r^{-2} + 3C_4 r^{-4})\cos(2\theta), \end{aligned} \tag{2.13b}$$

$$\begin{aligned}\dot{\epsilon}_{r\theta} = \bar{\dot{\epsilon}}_{r\theta}\sin(2\theta) &= \frac{1}{2}\left(\frac{1}{r}\frac{\partial v_r}{\partial \theta} + \frac{\partial v_\theta}{\partial r} - \frac{v_\theta}{r}\right) = \left(-\frac{2\bar{v}_r}{r} + \frac{\mathrm{d}\bar{v}_\theta}{\mathrm{d}r} - \frac{\bar{v}_\theta}{r}\right)\sin(2\theta) \\ &= -(3C_1 r^2 + C_2 + C_3 r^{-2} + 3C_4 r^{-4})\sin(2\theta). \end{aligned} \tag{2.13c}$$

In this section approximate velocity field along r and θ directions are obtained for plane strain with no dilatation. This field is compatible and incompressible and therefore is admissible.

2.1.2. Uniform Axial Deformation

It is useful to introduce a new quantity, macroscopic strain rate field, $\dot{E}_{ij}$ which is the volumetric average of microscopic strain rate field as given in the following equation:

$$\dot{E}_{ij} = \frac{1}{V}\int_V \dot{\epsilon}_{ij} dV. \tag{2.14}$$

Microscopic ($\dot{\epsilon}_{zz}$) and macroscopic ($\dot{E}_{33}$) strain rates along the axial direction are equal for uniform axial deformation. Shearing rates along axial direction is related to macroscopic strain rates $\dot{E}_{13}$ and $\dot{E}_{23}$. A rotation of the $r-\theta$ plane around the axial direction, z, that results in $\dot{E}_{13}$=0 will simplify equations without a loss in generality. After this rotation, new polar angle γ is measured from the new 2^* axis. The velocity field for this problem can be written in this new coordinate system as follows:

$$v_r = \bar{v}_r \, z \, \cos(\gamma), \tag{2.15a}$$

$$v_\gamma = -\bar{v}_r \, z \, \sin(\gamma), \tag{2.15b}$$

$$v_z = \bar{v}_z \, \cos(\gamma). \tag{2.15c}$$

Field equations in the new coordinate system are equilibrium equation along axial directio:

$$\frac{\partial \sigma_{rz}}{\partial r} + \frac{1}{r}\frac{\partial \sigma_{\gamma z}}{\partial \gamma} + \frac{\partial \sigma_{zz}}{\partial z} + \frac{\sigma_{rz}}{r} = 0, \tag{2.16}$$

three constitutive relations:

$$\sigma_{rz} = 2G\dot{\epsilon}_{rz}, \tag{2.17a}$$

$$\sigma_{\gamma z} = 2G\dot{\epsilon}_{\gamma z}, \tag{2.17b}$$

$$\sigma_{zz} = 0, \tag{2.17c}$$

and two strain rate-velocity relations:

$$\dot{\epsilon}_{rz} = \frac{1}{2}\left(\frac{\partial v_z}{\partial r} + \frac{\partial v_r}{\partial z}\right), \tag{2.18a}$$

$$\dot{\epsilon}_{\gamma z} = \frac{1}{2}\left(\frac{\partial v_\gamma}{\partial z} + \frac{1}{r}\frac{\partial v_z}{\partial \gamma}\right). \tag{2.18b}$$

When v_r, Equation 2.15a and v_z, Equation 2.15c are substituted into Equation 2.18a, and combined with Equation 2.17a, σ_{rz} can be rewritten in terms of $\bar{v}_r$ and $\bar{v}_z$ as follows

$$\sigma_{rz} = G \, \cos(\gamma)\left(\bar{v}_r + \frac{\mathrm{d}\bar{v}_z}{\mathrm{d}r}\right). \tag{2.19}$$

Similarly, $\sigma_{\gamma z}$ can be rewritten in terms of $\bar{v}_r$ and $\bar{v}_z$ as shown below

$$\sigma_{\gamma z} = -G\,\sin(\gamma)\left(\bar{v}_r + \frac{\bar{v}_z}{r}\right). \tag{2.20}$$

Using Equations 2.19 and 2.20, equilibrium equation along axial direction, Equation 2.16 becomes

$$\frac{\mathrm{d}^2\bar{v}_z}{\mathrm{d}r^2} + \frac{1}{r}\frac{\mathrm{d}\bar{v}_z}{\mathrm{d}r} - \frac{\bar{v}_z}{r^2} + \frac{\mathrm{d}\bar{v}_r}{\mathrm{d}r} = 0 \tag{2.21}$$

In the equation above, $\bar{v}_r$ and $\bar{v}_z$ are independent quantities, therefore they go to zero separately. Then, the general solution for Equation 2.21 is

$$\bar{v}_r = constant \equiv V^*_{32}, \tag{2.22a}$$

$$\bar{v}_z = C_5 r + C_6 r^{-1} \tag{2.22b}$$

where C_5, C_6 and V^*_{32} are constants and V^*_{32} is shearing velocity per unit axial length. Combining Equations 2.15 and 2.22, velocity field as a result of uniform axial deformation can be obtained as follows:

$$v_r = V^*_{32}\,z\,\cos(\gamma), \tag{2.23a}$$

$$v_\gamma = -V^*_{32}\,z\,\sin(\gamma), \tag{2.23b}$$

$$v_z = (C_5 r + C_6 r^{-1})\,\cos(\gamma). \tag{2.23c}$$

Resulting strain rate field is

$$\dot{\epsilon}_{rz} = \frac{1}{2}\left(\frac{\partial v_z}{\partial r} + \frac{\partial v_r}{\partial z}\right) = \frac{1}{2}\left(C_5 - C_6 r^{-2} + V^*_{32}\right)\,\cos(\gamma), \tag{2.24a}$$

$$\dot{\epsilon}_{\gamma z} = \frac{1}{2}\left(\frac{\partial v_\gamma}{\partial z} + \frac{1}{r}\frac{\partial v_z}{\partial \gamma}\right) = -\frac{1}{2}\left(C_5 + C_6 r^{-2} + V^*_{32}\right)\,\sin(\gamma), \tag{2.24b}$$

$$\dot{\epsilon}_{r\gamma} = \frac{1}{2}\left(\frac{\partial v_\gamma}{\partial r} - \frac{v_\gamma}{r} + \frac{1}{r}\frac{\partial v_r}{\partial \gamma}\right) = 0. \tag{2.24c}$$

2.1.3. General Dilatation

The velocity field considering general dilatation is derived from three-dimensional incompressibility with no angular dependence and considering uniform axial deformation. Strain rate field is,

$$\dot{\epsilon}_{rr} = \frac{\mathrm{d}v_r^D}{\mathrm{d}r}, \quad \dot{\epsilon}_{\theta\theta} = \frac{v_r^D}{r}, \quad \dot{\epsilon}_{zz} = \dot{E}_{33} \tag{2.25}$$

where the superscript D denotes dilatation. Equation 2.25 results in

$$\dot{\epsilon}_{kk} = \frac{\mathrm{d}v_r^D}{\mathrm{d}r} + \frac{v_r^D}{r} + \dot{E}_{33} = 0. \tag{2.26}$$

The velocity field solution without angular dependence is

$$v_r^D = C_7 r^{-1} - \frac{r}{2}\dot{E}_{33}, \tag{2.27a}$$

$$v_\theta^D = 0, \tag{2.27b}$$

$$v_z^D = \dot{E}_{33} z. \tag{2.27c}$$

where C_7 is constant. Resulting strain rate field is

$$\dot{\epsilon}_{rr}^D = \frac{\mathrm{d}v_r^D}{\mathrm{d}r} = -C_7 r^{-2} - \frac{1}{2}\dot{E}_{33}, \tag{2.28a}$$

$$\dot{\epsilon}_{\theta\theta} = \frac{v_r^D}{r} = C_7 r^{-2} - \frac{1}{2}\dot{E}_{33}. \tag{2.28b}$$

2.1.4. General Velocity and Strain Rate Fields

One gets the general form of the velocity and strain rate fields superposing velocity and strain rate fields obtained from *i*) plane strain, *ii*) uniform axial deformation and *iii*) general dilatation analyses. Velocity field is

$$\begin{aligned} v_r &= (C_1 r^3 + C_2 r + C_3 r^{-1} + C_4 r^{-3})\, \cos(2\theta) \\ &\quad + C_7 r^{-1} - \frac{1}{2}\dot{E}_{33} r + V_{32}^{*}\, z\, \cos(\gamma), \end{aligned} \tag{2.29a}$$

$$v_\theta = (-2C_1 r^3 - C_2 r + C_4 r^{-3})\, \sin(2\theta) - V_{32}^{*}\, z\, \sin(\gamma), \tag{2.29b}$$

$$v_z = (C_5 r + C_6 r^{-1})\, \cos(\gamma) + \dot{E}_{33} z. \tag{2.29c}$$

Similarly, strain rate field is

$$\begin{aligned} \dot{\epsilon}_{rr} &= \frac{\partial v_r}{\partial r} \\ &= (3C_1 r^2 + C_2 - C_3 r^{-2} - 3C_4 r^{-4})\, \cos(2\theta) - C_7 r^{-2} - \frac{1}{2}\dot{E}_{33}, \end{aligned} \tag{2.30a}$$

$$\begin{aligned} \dot{\epsilon}_{\theta\theta} &= \frac{1}{r}\frac{\partial v_\theta}{\partial \theta} + \frac{v_r}{r} \\ &= (-3C_1 r^2 - C_2 + C_3 r^{-2} + 3C_4 r^{-4})\, \cos(2\theta) + C_7 r^{-2} - \frac{1}{2}\dot{E}_{33}, \end{aligned} \tag{2.30b}$$

$$\dot{\epsilon}_{zz} = \frac{\partial v_z}{\partial z} = \dot{E}_{33}, \tag{2.30c}$$

$$\begin{aligned}\dot{\epsilon}_{r\theta} &= \frac{1}{2}\left(\frac{1}{r}\frac{\partial v_r}{\partial \theta} + \frac{\partial v_\theta}{\partial r} - \frac{v_\theta}{r}\right) \\ &= -(3C_1 r^2 + C_2 + C_3 r^{-2} + 3C_4 r^{-4})\ \sin(2\theta), \qquad (2.30\text{d})\end{aligned}$$

$$\begin{aligned}\dot{\epsilon}_{rz} &= \frac{1}{2}\left(\frac{\partial v_z}{\partial r} + \frac{\partial v_r}{\partial z}\right) \\ &= \frac{1}{2}(C_5 - C_6 r^{-2} + V_{32}^*)\ \cos(\gamma), \qquad (2.30\text{e})\end{aligned}$$

$$\begin{aligned}\dot{\epsilon}_{\theta z} &= \frac{1}{2}\left(\frac{\partial v_\theta}{\partial z} + \frac{1}{r}\frac{\partial v_z}{\partial \theta}\right) \\ &= -\frac{1}{2}(C_5 + C_6 r^{-2} + V_{32}^*)\ \sin(\gamma). \qquad (2.30\text{f})\end{aligned}$$

Boundary conditions on the outer surface for velocities v_i in terms of macroscopic strain rates must be obtained to determine constants C_1 through C_7 in Equations 2.29 - 2.30. In general, boundary conditions are in the following form:

$$v_i\Big|_s = \dot{E}_{ik} x_k\Big|_s. \qquad (2.31)$$

Therefore,

$$v_r\Big|_s = \dot{E}_{rr} b + \dot{E}_{rz} z, \qquad (2.32\text{a})$$

$$v_\theta\Big|_s = \dot{E}_{\theta r} b + \dot{E}_{\theta z} z, \qquad (2.32\text{b})$$

$$v_z\Big|_s = \dot{E}_{zr} b + \dot{E}_{zz} z. \qquad (2.32\text{c})$$

Before obtaining boundary conditions, a transformation is required between cartesian and polar coordinate systems to obtain microscopic strain rate field (in polar coordinates) in terms of macroscopic strain rate field (in cartesian coordinates). The transformation is not ordinary because θ is measured from the 2 - axis instead of the 1 - axis (See Figure 2.2).

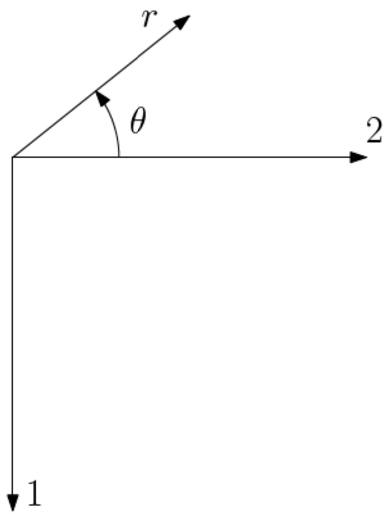

Figure 2.2. Polar coordinates where θ is measured from 2 - axis

Transformation matrix for the coordinate systems in Figure 2.2 is

$$\boldsymbol{T} = \begin{bmatrix} \cos(\frac{\pi}{2}+\theta) & \cos(\theta) \\ \cos(\pi+\theta) & \cos(\frac{\pi}{2}+\theta) \end{bmatrix} = \begin{bmatrix} -\sin(\theta) & \cos(\theta) \\ -\cos(\theta) & -\sin(\theta) \end{bmatrix} \tag{2.33}$$

Transformations for the 1^{st}-order velocity tensor, $\boldsymbol{v}$,and for the 2^{nd}-order macroscopic strain rate tensor, $\dot{\boldsymbol{E}}$ are given as follows:

$$\boldsymbol{v}_{polar} = \boldsymbol{T}\boldsymbol{v}_{cart.}, \tag{2.34}$$

$$\dot{\boldsymbol{E}}_{polar} = \boldsymbol{T}\dot{\boldsymbol{E}}_{cart.}\boldsymbol{T}^T. \tag{2.35}$$

Using the transformations above, one gets

$$v_r = -v_1\sin(\theta) + v_2\cos(\theta), \tag{2.36a}$$

$$v_\theta = -v_1\cos(\theta) - v_2\sin(\theta), \tag{2.36b}$$

$$\dot{E}_{rr} = \dot{E}_{11}\sin^2(\theta) + \dot{E}_{22}\cos^2(\theta) - 2\dot{E}_{12}\sin(\theta)\cos(\theta), \tag{2.37a}$$

$$\dot{E}_{\theta\theta} = \dot{E}_{11}\cos^2(\theta) + \dot{E}_{22}\sin^2(\theta) + 2\dot{E}_{12}\sin(\theta)\cos(\theta), \tag{2.37b}$$

$$\dot{E}_{r\theta} = (\dot{E}_{11} - \dot{E}_{22})\sin(\theta)\cos(\theta) + \dot{E}_{12}(\sin^2(\theta) - \cos^2(\theta)). \tag{2.37c}$$

Similarly, $\dot{E}_{rz}$ and $\dot{E}_{\theta z}$ are obtained using a similar transformation.

$$\dot{E}_{rz} = -V_{31}^{*}\sin(\gamma) + V_{32}^{*}\cos(\gamma) \tag{2.38a}$$

$$\dot{E}_{\theta z} = -V_{31}^{*}\cos(\gamma) - V_{32}^{*}\sin(\gamma) \tag{2.38b}$$

$$\dot{E}_{zz} = \dot{E}_{33} \tag{2.38c}$$

Axial strain rates are obtained considering uniform axial deformation in section 2.1.2 and the derivations are handled in a different coordinate system denoted by * where $\dot{E}_{13}$=0. $\dot{E}_{rz}$ and $\dot{E}_{\theta z}$ are expressed in terms of shearing velocities per unit axial length V_{31}^{*} and V_{32}^{*}.

Boundary conditions can be obtained by substituting Equations 2.37-2.38 into Equations 2.32a-2.32c and taking into account that $\dot{E}_{12}$ and V_{31}^{*} (remember that $\dot{E}_{13}$=0 in * superscripted coordinate system) are 0, as follows:

$$v_r = \dot{E}'b\cos(2\theta) + \frac{1}{2}(\dot{E}_{22} + \dot{E}_{11})b + V_{32}^{*}z\cos(\gamma), \tag{2.39a}$$

$$v_\theta = -\dot{E}'b\sin(2\theta) - V_{32}^{*}z\sin(\gamma), \tag{2.39b}$$

$$v_z = V_{23}^{*}b\cos(\gamma) + \dot{E}_{33}z \tag{2.39c}$$

where

$$\dot{E}' = \frac{1}{2}(\dot{E}_{22} - \dot{E}_{11}) \tag{2.40}$$

and V_{23}^{*} is shear velocity parallel to the 3 - axis and it is similar to V_{32}^{*}. Another boundary condition is zero shear strain rate on the void surface.

$$\dot{\epsilon}_{r\theta}|_{r=a} = 0, \tag{2.41a}$$

$$\dot{\epsilon}_{rz}|_{r=a} = 0. \tag{2.41b}$$

General velocity field equations, Equations 2.29 and velocity boundary condition, Equations 2.39 give

$$C_1 b^2 + C_2 + C_3 b^{-2} + C_4 b^{-4} = \dot{E}', \tag{2.42a}$$

$$C_7 b^{-1} - \frac{1}{2}\dot{E}_{33} b = \frac{1}{2}(\dot{E}_{11} + \dot{E}_{22}) b, \tag{2.42b}$$

$$C_5 + C_6 b^{-2} = V_{23}^*. \tag{2.42c}$$

From Equation 2.42b, C_7 can be solved

$$C_7 = \dot{E} b^2 \tag{2.43}$$

where $\dot{E} = \frac{1}{2}(\dot{E}_{11} + \dot{E}_{22} + \dot{E}_{33})$. Substituting $\dot{\epsilon}_{r\theta}$ and $\dot{\epsilon}_{rz}$, Equations 2.30d-2.30e into Equations 2.41a and 2.41b yields the following two equations:

$$3C_1 a^2 + C_2 + C_3 a^{-2} + 3C_4 a^{-4} = 0, \tag{2.44a}$$

$$C_5 - C_6 a^{-2} = -V_{32}^*, \tag{2.44b}$$

C_5 and C_6 are uniquely determined from Equations 2.42c and 2.44b:

$$C_5 = \frac{V_{23}^* - f V_{32}^*}{1 + f}, \tag{2.45}$$

$$C_6 = \frac{a^2 (V_{23}^* + V_{32}^*)}{1 + f} \tag{2.46}$$

where

$$f = \frac{a^2}{b^2} \qquad \text{(void volume fraction for a cylindrical void).} \tag{2.47}$$

Notice that there are four unknowns, C_1 through C_4 and two equations, namely Equations 2.42a and 2.44a are left. Therefore the system is indeterminate. In Gurson's study the velocity field is taken to be linear in r for such a type of problem. Hence the $C_1 r^3$ term violates this intuition. Therefore it is proposed that C_1 goes to zero. Wen and Hwang [39] denied this intuition and presented a correction. Their work also includes the missed relation between C_i and macroscopic quantities: $2C_1b^2 + C_2 - C_4b^{-4} = \dot{E}'$. Here, Gurson yield criterion will be explained disregarding these corrections. Letting C_1 be equal to zero, C_3 and C_4 are expressed in terms of C_2 and known macroscopic quantities. Then C_2 is determined numerically letting $C_2 = C_2'(f)\dot{E}'$ and using the minimization of dissipation energy $\dot{W}$;

$$\dot{W} = \frac{1}{V}\int_V \sigma'_{ij}\dot{\epsilon}_{ij}\, dV = \frac{1}{V}\int_V \sqrt{\frac{2}{3}}\sigma_Y \sqrt{\dot{\epsilon}_{ij}\dot{\epsilon}_{ij}}\, dV. \tag{2.48}$$

Solving Equations 2.42a and 2.44a for C_3 and C_4 in terms of C_2 letting $C_1 = 0$ gives

$$C_3 = \frac{b^2}{3-f}(3\dot{E}' - (3-f^2)C_2), \tag{2.49}$$

$$C_4 = \frac{a^2b^2}{3-f}(C_2(1-f) - \dot{E}'). \tag{2.50}$$

Rewrite microscopic strain rates Equations 2.30a, 2.30b, 2.30d in a compact form.

$$\dot{\epsilon}_{rr} = \bar{\dot{\epsilon}}_{rr}\cos(2\theta) - \dot{E}\lambda^{-1} - \frac{1}{2}\dot{E}_{33} \tag{2.51a}$$

$$\dot{\epsilon}_{\theta\theta} = -\bar{\dot{\epsilon}}_{rr}\cos(2\theta) + \dot{E}\lambda^{-1} - \frac{1}{2}\dot{E}_{33} \tag{2.51b}$$

$$\dot{\epsilon}_{r\theta} = \bar{\dot{\epsilon}}_{r\theta}\sin(2\theta) \tag{2.51c}$$

where $\lambda = \frac{r^2}{b^2}$. Applying the form $C_2 = C_2'(f)\dot{E}'$ it can be shown that

$$\bar{\dot{\epsilon}}_{rr} = \dot{E}'\left(C_2'(1+A) - \frac{3(\lambda - f)}{\lambda^2(3-f)}\right) \tag{2.52a}$$

$$\bar{\dot{\epsilon}}_{r\theta} = -\dot{E}'\left(C_2'(1-A) + \frac{3(\lambda - f)}{\lambda^2(3-f)}\right) \tag{2.52b}$$

where

$$A = \frac{\lambda(3-f^2) - 3f(1-f)}{\lambda^2(3-f)}. \tag{2.53}$$

Empirical forms of C_2' is obtained fitting finite number of data points for $0 \leq$

$f \leq 0.5$ and for very small f (≤ 0.01) while minimizing $\dot{W}$. It is cumbersome to deal with the velocity and strain rate fields in this form. Therefore a simpler form is considered that results when strain rate boundary conditions Equation 2.41a and 2.41b are omitted and dependence of $\bar{\dot{\epsilon}}_{rr}, \bar{\dot{\epsilon}}_{r\theta}, \bar{\dot{\epsilon}}_{rz}$ and $\bar{\dot{\epsilon}}_{\theta z}$ on λ is eliminated. This results

$$\bar{\dot{\epsilon}}_{rr} = \dot{E}', \tag{2.54a}$$

$$\bar{\dot{\epsilon}}_{r\theta} = -\dot{E}', \tag{2.54b}$$

$$C_2' = 1, \tag{2.54c}$$

$$\bar{\dot{\epsilon}}_{rz} = \frac{1}{2}(V_{23}^* + V_{32}^*) = \dot{E}_{23}^*, \tag{2.54d}$$

$$\bar{\dot{\epsilon}}_{\theta z} = -\frac{1}{2}(V_{23}^* + V_{32}^*) = -\dot{E}_{23}^*. \tag{2.54e}$$

Strain rate field 2.30 takes the following form using above equations:

$$\dot{\epsilon}_{rr} = \dot{E}' \cos(2\theta) - \dot{E} b^2 r^{-2} - \frac{\dot{E}_{33}}{2} \tag{2.55a}$$

$$\dot{\epsilon}_{\theta\theta} = -\dot{E}' \cos(2\theta) + \dot{E} b^2 r^{-2} - \frac{\dot{E}_{33}}{2} \tag{2.55b}$$

$$\dot{\epsilon}_{zz} = \dot{E}_{33} \tag{2.55c}$$

$$\dot{\epsilon}_{r\theta} = -\dot{E}' \sin(2\theta) \tag{2.55d}$$

$$\dot{\epsilon}_{rz} = \dot{E}_{23}^* \cos(\gamma) \tag{2.55e}$$

$$\dot{\epsilon}_{\theta z} = -\dot{E}_{23}^* \sin(\gamma) \tag{2.55f}$$

Axisymmetric deformation is studied for the rest of the analysis which is the simplest case. Macroscopic stress field Σ_{ij} is the areal average of the microscopic stress field σ_{ij}. Σ_{ij} is work conjugate of $\dot{E}_{ij}$ and these can be formulated as follows:

$$\Sigma_{ij} = \frac{1}{A} \int_A \sigma_{ij} dS, \tag{2.56}$$

$$\dot{W} = \Sigma_{ij} \dot{E}_{ij}. \tag{2.57}$$

The yield locus of Σ_{ij} has the properties of convexity and normality. Therefore $\delta\Sigma_{ij}\, \dot{E}_{ij} = 0$. This results the following relation between $\dot{W}$ and Σ_{ij} using the above

Equation 2.57.

$$\delta\dot{W} = \Sigma_{ij}\,\delta\dot{E}_{ij} \quad \Rightarrow \quad \Sigma_{ij} = \frac{\partial\dot{W}}{\partial\dot{E}_{ij}} \tag{2.58}$$

Tensile yield stress σ_Y is assumed constant in the matrix and the following normalization is used.

$$T_{ij} = \frac{\Sigma_{ij}}{\sigma_Y} \tag{2.59}$$

The stress and strain rate systems are

$$\begin{aligned} T_{11} = T_{22}, \quad T_{eqv} = |T_{33} - T_{11}|, && (2.60a)\\ \dot{E}_{12} = \dot{E}_{21} = \dot{E}_{13} = \dot{E}_{31} = \dot{E}_{23} = \dot{E}_{32} = 0, &&\\ \dot{E}_{11} = \dot{E}_{22} \quad \Rightarrow \quad \dot{E}' = 0, && (2.60b)\end{aligned}$$

therefore

$$\dot{\epsilon}_{ij}\dot{\epsilon}_{ij} = 2\dot{E}^2\lambda^{-2} + \frac{3\dot{E}_{33}^2}{2} \tag{2.60c}$$

due to axisymmetry. Combining Equations 2.48, 2.58, 2.59, 2.60a and 2.60c results

$$\begin{aligned} T_{11} &= \frac{1}{\sigma_Y}\frac{\partial\dot{W}}{\partial\dot{E}_{11}} = \frac{1}{\sqrt{3}}\frac{1}{V}\int_V \dot{E}\lambda^{-2}\left(\dot{E}\lambda^{-2} + \frac{3}{4}\dot{E}_{33}^2\right)^{-1/2} dV, && (2.61a)\\ T_{33} &= \frac{1}{\sigma_Y}\frac{\partial\dot{W}}{\partial\dot{E}_{33}} = \frac{1}{\sqrt{3}}\frac{1}{V}\int_V \left(\dot{E}\lambda^{-2} + \frac{3}{2}\dot{E}_{33}\right)\left(\dot{E}\lambda^{-2} + \frac{3}{4}\dot{E}_{33}^2\right)^{-1/2} dV, && (2.61b)\\ T_{eqv} &= T_{33} - T_{11} = \frac{\sqrt{3}}{2}\frac{1}{V}\int_V \dot{E}_{33}\left(\dot{E}\lambda^{-2} + \frac{3}{4}\dot{E}_{33}^2\right)^{-1/2} dV. && (2.61c)\end{aligned}$$

The following changes of variables are used

$$x \equiv \dot{E}\lambda^{-1}, \quad g \equiv \frac{3}{4}\dot{E}_{33}, \tag{2.62a}$$

$$\begin{aligned}\frac{1}{V}\int_V dV &= \frac{1}{\pi b^2 L}\int_0^L\int_0^{2\pi}\int_a^b dr d\theta dz \\ &= \int_f^1 d\lambda = \int_{\dot{E}/f}^{\dot{E}} \frac{-\dot{E}}{x^2} d\lambda \quad \text{(for axial symmetry).} \qquad (2.62b)\end{aligned}$$

Using the above variables, T_{eqv} Equation 2.61c and T_{11} Equation 2.61a can be rewritten as follows

$$T_{eqv} = g^{1/2}\dot{E}\int_{\dot{E}}^{\dot{E}/f} x^{-2}(x^2+g^2)^{-1/2}dx = \frac{\sqrt{\dot{E}^2+g}-\sqrt{\dot{E}^2+gf^2}}{\sqrt{g}} \qquad (2.63a)$$

$$T_{11} = \frac{1}{\sqrt{3}}\int_{\dot{E}}^{\dot{E}/f}(x^2+g)^{-1/2}dx = \frac{1}{\sqrt{3}}\ln\left(\frac{\sqrt{\dot{E}^2+gf^2}+\dot{E}}{f(\sqrt{\dot{E}^2+g}+\dot{E})}\right) \qquad (2.63b)$$

Eliminating $\dot{E}$ and g from Equations 2.63a and 2.63b gives an equation in T_{eqv}, T_{11} and f that is the Gurson's yield function for cylindrical void. The resulting yield function for axisymmetry is

$$\Phi_{cylindrical} = \frac{\Sigma_{eqv}^2}{\sigma_Y^2} + 2f\cosh\left(\frac{\sqrt{3}\Sigma_{11}}{\sigma_Y}\right) - 1 - f^2 = 0 \qquad (2.64)$$

where f is void volume fraction, σ_Y is tensile flow stress in matrix material, Σ_{11} is radial stress in symmetry plane,

$$\Sigma_{eqv} = T_{eqv}\sigma_Y = \left(\frac{3}{2}\Sigma'_{ij}\Sigma'_{ij}\right)^{1/2}, \qquad (2.65a)$$

$$\Sigma'_{ij} = \Sigma_{ij} - \delta_{ij}\frac{\Sigma_{kk}}{3}. \qquad (2.65b)$$

Σ_{eqv}, Σ'_{ij} are macroscopic equivalent von Mises and deviatoric stresses, respectively.

2.2. Spherical Voids

The spherical void geometry is shown in Figure 2.3. The approximate velocity field is split into two parts; shape change at constant volume (v_i^s), and volume change at constant shape (v_i^v). The total velocity field is

$$v_i = v_i^s + v_i^v. \tag{2.66}$$

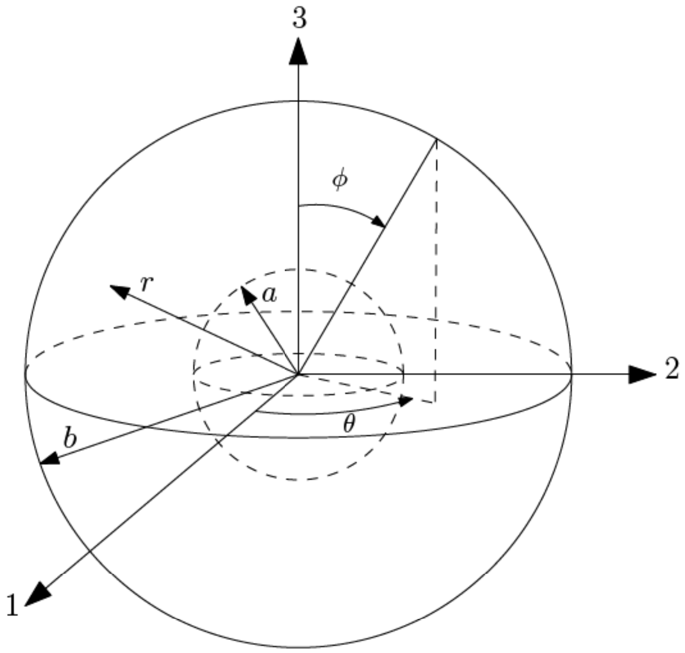

Figure 2.3. Spherical void geometry

The microscopic strain rate field ϵ_{ij} calculated from v_i must be incompressible and v_i must meet external boundary conditions in terms of $\dot{E}_{ij}$. The boundary conditions are separated as follows since velocity field Equation 2.66 is constructed separately.

$$v_i^s|_S = \dot{E}'_{ij} x_j|_S \tag{2.67}$$

$$v_i^v|_S = \left.\frac{\dot{E}_{nn}}{3} x_i\right|_S \tag{2.68}$$

where

$$\dot{E}_{ij} = \dot{E}'_{ij} + \frac{\dot{E}_{nn}}{3}\delta_{ij}. \tag{2.69}$$

Microscopic strain rate field can be separated as v_i, then one gets

$$\dot{\epsilon}_{ij} = \dot{\epsilon}_{ij}^s + \dot{\epsilon}_{ij}^v \tag{2.70}$$

Equation 2.67 gives

$$\dot{\epsilon}^s_{ij} = \dot{E}'_{ij} \tag{2.71}$$

that satisfies incompressibility due to the nature of deviatory.

By symmetry, v^v_i should consist of radial component only. Therefore, incompressibility is written as follows

$$\dot{\epsilon}^v_{nn} = \frac{\mathrm{d}v^v_r}{\mathrm{d}r} + \frac{2v^v_r}{r} = 0 \tag{2.72}$$

Above equation results

$$v^v_r = Cr^{-2} \tag{2.73}$$

where C is a constant. Applying the boundary condition Equation 2.68

$$v^v_r|_{r=b} = Cb^{-2} = \frac{\dot{E}_{nn}}{3}b \quad \Rightarrow \quad C = \frac{\dot{E}_{nn}}{3}b^3 \tag{2.74}$$

The velocity field corresponding to pure dilatation is

$$v^v_r = \frac{\dot{E}_{nn}}{3}\frac{b^3}{r^2}, \quad v^v_\theta = v^v_\phi = 0. \tag{2.75}$$

$\dot{\epsilon}^v_{ij}$ in spherical coordinates are

$$\dot{\epsilon}^v_{rr} = \frac{\partial v^v_r}{\partial r} = -\frac{2}{3}\left(\frac{b}{r}\right)^3 \dot{E}_{nn} \tag{2.76}$$

$$\dot{\epsilon}^v_{\theta\theta} = \frac{1}{r}\left(\frac{\partial v^v_\phi}{\partial \phi} + v^v_r\right) = \frac{1}{3}\left(\frac{b}{r}\right)^3 \dot{E}_{nn} \tag{2.77}$$

$$\dot{\epsilon}^v_{\phi\phi} = \frac{1}{r\sin(\phi)}\left(\frac{\partial v^v_\theta}{\partial \theta} + v^v_r \sin(\phi) + v^v_\phi \cos(\phi)\right) = \frac{1}{3}\left(\frac{b}{r}\right)^3 \dot{E}_{nn} \tag{2.78}$$

$$\dot{\epsilon}^v_{r\theta} = \dot{\epsilon}^v_{r\phi} = \dot{\epsilon}^v_{\theta\phi} = 0 \tag{2.79}$$

Notice that incompressibility is satisfied.

$\dot{\epsilon}_{ij}$ can be written using the new variable h_{ij}

$$\dot{\epsilon}_{ij} = \dot{E}'_{ij} + \frac{\dot{E}_{nn}}{3} h_{ij} \tag{2.80}$$

In spherical coordinates:

$$h_{rr} = -2\left(\frac{b}{r}\right)^3 \tag{2.81}$$

$$h_{\phi\phi} = h_{\theta\theta} = \left(\frac{b}{r}\right)^3 \tag{2.82}$$

$$h_{ij} = 0 \quad \text{when} \quad i \neq j. \tag{2.83}$$

In cartesian coordinates:

$$h_{ij} = \left(\delta_{ij} - \frac{3x_i x_j}{r^2}\right)\left(\frac{b}{r}\right)^3 = \left(\delta_{ij} - 3n_i n_j\right)\left(\frac{b}{r}\right)^3 \tag{2.84}$$

where

$$r^2 = x_1^2 + x_2^2 + x_3^2 \tag{2.85}$$

$$n_i = \frac{x_i}{r} \tag{2.86}$$

n_i are the cartesian components of the normal to a sphere of radius r. An approximate $\dot{\epsilon}_{ij}$ field is constructed and now using the Equations 2.48 and 2.58 macroscopic stress Σ_{ij} can be written as a function of $\dot{E}_{ij}$.

$$\Sigma_{ij} = \frac{1}{V}\int_V \sigma'_{kl} \frac{\partial \dot{\epsilon}_{kl}}{\partial \dot{E}_{ij}}\, dV \tag{2.87}$$

Equation 2.80 can be rewritten as follows

$$\dot{\epsilon}_{kl} = \dot{E}_{kl} + \frac{\dot{E}_{nn}}{3}\left(h_{kl} - \delta_{kl}\right) \tag{2.88}$$

so,

$$\frac{\partial \dot{\epsilon}_{kl}}{\partial \dot{E}_{ij}} = \delta_{ki}\delta_{lj} + \frac{\delta_{ij}}{3}(h_{kl} - \delta_{kl}) \tag{2.89}$$

Using the fact that $\sigma'_{kl}\delta_{kl} = \sigma'_{kk} = 0$, Equation 2.87 becomes

$$\Sigma_{ij} = \frac{1}{V}\int_V \left(\sigma'_{ij} + \frac{\delta_{ij}\sigma'_{kl}h_{kl}}{3}\right) dV = \Sigma'_{ij} + \frac{\Sigma_{kk}}{3}\delta_{ij} \tag{2.90}$$

Matching coefficients of δ_{ij} gives

$$\begin{aligned} \Sigma'_{ij} &= \frac{1}{V}\int_V \sigma'_{ij}\, dV &(2.91) \\ \Sigma_{kk} &= \frac{1}{V}\int_V \sigma'_{kl}h_{kl}\, dV &(2.92) \end{aligned}$$

Using $\sigma'_{kk} = 0$ again and Equations 2.81-2.83, it can be written

$$\begin{aligned} \Sigma_{kk} &= \frac{1}{V}\int_V \left(\sigma'_{rr} - \frac{\sigma'_{\theta\theta} + \sigma'_{\phi\phi}}{2}\right) h_{rr}\, dV \\ &= \frac{1}{V}\int_V \left(\frac{3\sigma'_{rr}}{2} - \frac{\sigma'_{rr} + \sigma'_{\theta\theta} + \sigma'_{\phi\phi}}{2}\right) h_{rr}\, dV \\ &= \frac{1}{V}\int_V \frac{3\sigma'_{rr}}{2} h_{rr}\, dV &(2.93) \end{aligned}$$

Macroscopic stresses in terms of σ_Y and $\dot{\epsilon}_{ij}$ can be obtained using Prandtl-Reuss stress strain relation, Equation 2.2.

$$\begin{aligned} \Sigma'_{ij} &= \frac{1}{V}\int_V \sqrt{\frac{2}{3}} \frac{\sigma_Y \dot{\epsilon}_{ij}}{\sqrt{\dot{\epsilon}_{kl}\dot{\epsilon}_{kl}}}\, dV &(2.94) \\ \Sigma_{kk} &= \frac{1}{V}\int_V \sqrt{\frac{3}{2}} \frac{\sigma_Y \dot{\epsilon}_{rr} h_{rr}}{\sqrt{\dot{\epsilon}_{kl}\dot{\epsilon}_{kl}}}\, dV &(2.95) \end{aligned}$$

The integrands must first be expressed in terms of $\dot{E}_{ij}$. Using the fact that $\dot{E}'_{nn} = 0$

and Equations 2.80-2.83 yield

$$\begin{aligned}
\dot{\epsilon}_{ij}\dot{\epsilon}_{ij} &= \dot{E}'_{ij}\dot{E}'_{ij} + \frac{2}{3}\dot{E}_{nn}\dot{E}'_{ij}h_{ij} + \frac{1}{9}\dot{E}^2_{nn}h_{ij}h_{ij} \\
&= \dot{E}'_{ij}\dot{E}'_{ij} + \frac{2}{3}\dot{E}_{nn}h_{rr}\left(\frac{3\dot{E}'_{rr}}{2} - \frac{1}{2}(\dot{E}'_{rr} + \dot{E}'_{\theta\theta} + \dot{E}'_{\phi\phi})\right) + \frac{2}{3}\dot{E}^2_{nn}\left(\frac{b}{r}\right)^6 \\
&= \dot{E}'_{ij}\dot{E}'_{ij} - 2\dot{E}_{nn}\dot{E}'_{rr}\left(\frac{b}{r}\right)^3 + \frac{2}{3}\dot{E}^2_{nn}\left(\frac{b}{r}\right)^6 \qquad (2.96)
\end{aligned}$$

The following changes of variable will be useful for tracking the Equations 2.94 and 2.95. New variables are

$$D = \frac{\dot{E}_{nn}}{3\sqrt{\frac{2}{3}\dot{E}'_{kl}\dot{E}'_{kl}}} \qquad (2.97)$$

$$t_{ij} = \frac{\dot{E}'_{ij}}{\sqrt{\frac{2}{3}\dot{E}'_{kl}\dot{E}'_{kl}}} \qquad (2.98)$$

$$\mu = \frac{\dot{E}'_{rr}}{\sqrt{\frac{2}{3}\dot{E}'_{kl}\dot{E}'_{kl}}} \qquad (2.99)$$

$$\lambda = \left(\frac{r}{b}\right)^3 \qquad (2.100)$$

$$Q = 1 - 4D\mu\lambda^{-1} + 4D^2\lambda^{-2} \qquad (2.101)$$

The volume integral over the sphere is treated in the following manner.

$$\frac{1}{V}\int_V dV = \frac{1}{\frac{4}{3}\pi b^3}\int_\Omega\int_a^b r^2 dr d\Omega = \frac{1}{4\pi}\int_\Omega\int_f^1 d\lambda d\Omega \qquad (2.102)$$

where

$$\int_\Omega d\Omega = \int_0^{2\pi}\int_0^\pi \sin(\phi)d\phi d\theta \qquad (2.103)$$

$$f = \frac{a^3}{b^3} \qquad \text{(void volume fraction for a spherical void)} \qquad (2.104)$$

Using the Equations 2.80, 2.84 and 2.96-2.102, macroscopic stresses Equations 2.94 and 2.95 become

$$\begin{aligned}\Sigma'_{ij} &= \frac{\sigma_Y}{6\pi}\int_\Omega\int_f^1 \frac{1}{\sqrt{Q}}[t_{ij}+(\delta_{ij}-3n_in_j)D\lambda^{-1}]\;d\lambda d\Omega && (2.105)\\ \Sigma_{kk} &= \frac{\sigma_Y}{2\pi}\int_\Omega\int_f^1 \frac{1}{\sqrt{Q}}(2D\lambda^{-1}-\mu)\lambda^{-1}\;d\lambda d\Omega && (2.106)\end{aligned}$$

Above equations show that macroscopic stresses depend only the ratios of the $\dot{E}_{ij}$, and not on their magnitudes. Integration of Equations 2.105 and 2.106 with respect to λ yield

$$\begin{aligned}\Sigma'_{ij} &= -\frac{\sigma_Y}{6\pi}\int_\Omega\left[t_{ij}H(\lambda,\mu)+D\;G(\lambda,\mu)(\delta_{ij}-3n_in_j+2\mu t_{ij})\right]\Bigg|_{\lambda=1}^{\lambda=f} d\Omega && (2.107)\\ \Sigma_{kk} &= \frac{\sigma_Y}{2\pi}\int_\Omega\left[\frac{D}{|D|}F(\lambda,\mu)+\mu\;G(\lambda,\mu)\right]\Bigg|_{\lambda=1}^{\lambda=f} d\Omega && (2.108)\end{aligned}$$

where

$$\begin{aligned}F(\lambda,\mu) &= \ln\left(\sqrt{Q}+2|D|\lambda^{-1}-\frac{D}{|D|}\mu\right) && (2.109)\\ G(\lambda,\mu) &= \ln(\sqrt{Q}\lambda+\lambda-2D\mu) && (2.110)\\ H(\lambda,\mu) &= \sqrt{Q}\lambda && (2.111)\end{aligned}$$

Next step is to obtain an approximate analytical solution to Equations 2.107 and 2.108. Taylor expansion of the functions F, G and H in μ around $\mu = 0$ is used for approximate solution. The expansions are of the form

$$F(\lambda,\mu)\Big|_{\lambda=1}^{\lambda=f} = F^{(0)}+\mu F^{(1)}+\frac{1}{2}\mu^2F^{(2)}+\ldots \qquad (2.112)$$

where

$$F^{(n)} = \left(\frac{\partial^n F(\lambda,\mu)}{\partial\mu^n}\right)_{\mu=0}\Bigg|_{\lambda=1}^{\lambda=f} \qquad (2.113)$$

The approximate stress integrals where F, G and H are expanded to second order in μ

become

$$\begin{aligned}
\Sigma'_{ij} &\approx -\frac{\sigma_Y}{6\pi}\int_\Omega \left[t_{ij}\left(H^{(0)}+\mu H^{(1)}+\frac{1}{2}\mu^2 H^{(2)}\right)+2Dt_{ij}\left(\mu G^{(0)}+\mu^2 G^{(1)}\right)\right. \\
&\quad \left. +(\delta_{ij}-3n_in_j)\left(G^{(0)}+\mu G^{(1)}+\frac{1}{2}\mu^2 G^{(2)}\right)\right] d\Omega \qquad (2.114) \\
\Sigma_{kk} &\approx \frac{\sigma_Y}{2\pi}\int_\Omega \left[\frac{D}{|D|}\left(F^{(0)}+\mu F^{(1)}+\frac{1}{2}\mu^2 F^{(2)}\right)+\left(\mu G^{(0)}+\mu^2 G^{(1)}\right)\right] d\Omega \qquad (2.115)
\end{aligned}$$

Using the Equations B.4-B.6 derived in Appendix B and dropping the smaller terms, one gets

$$\begin{aligned}
T'_{ij} &= \frac{\Sigma'_{ij}}{\sigma_Y} = -t_{ij}\left(\frac{2}{3}H^{(0)}+\frac{1}{15}H^{(2)}+\frac{4}{15}DG^{(1)}\right) \qquad (2.116) \\
T_{kk} &= \frac{\Sigma_{kk}}{\sigma_Y} = \frac{D}{|D|}\left(2F^{(0)}+\frac{1}{5}F^{(2)}\right)+\frac{2}{5}G^{(1)} \qquad (2.117)
\end{aligned}$$

Again dropping the smaller terms, macroscopic equivalent tensile stress can be calculated as shown below

$$\begin{aligned}
T_{eqv}^2 = \frac{3}{2}T'_{ij}T'_{ij} &\approx \frac{3}{2}t_{ij}t_{ij}\left(\frac{4}{9}(H^{(0)})^2+\frac{4}{45}H^{(0)}H^{(2)}\right) \\
&\approx (H^{(0)})^2+\frac{1}{5}H^{(0)}H^{(2)} \qquad (2.118)
\end{aligned}$$

$$\begin{aligned}
T_{eqv} &\approx \left((H^{(0)})^2+\frac{1}{5}H^{(0)}H^{(2)}\right)^{1/2} \\
&\approx |H^{(0)}|\left(1+\frac{1}{5}H^{(0)}H^{(2)}\right)^{1/2} \\
&\approx |H^{(0)}|+\frac{1}{10}H^{(2)}\,\mathrm{sgn}(H^{(0)}) \qquad (2.119)
\end{aligned}$$

Following statements can be obtained from Equations 2.109-2.111 and using Equation 2.113.

$$
\begin{aligned}
F^{(0)} &= \ln\left(\frac{\sqrt{f^2+4D^2}+2|D|}{f(\sqrt{1+4D^2}+2|D|)}\right) && (2.120)\\
F^{(2)} &= -\left(\frac{1}{1+4D^2\lambda^{-2}}+\frac{4D^2\lambda^{-2}}{(1+4D^2\lambda^{-2})^{3/2}(\sqrt{1+4D^2\lambda^{-2}}+2|D|\lambda^{-1})}\right)\Bigg|_{\lambda=1}^{\lambda=f} && (2.121)\\
G^{(1)} &= -\frac{2D\lambda^{-1}}{\sqrt{1+4D^2\lambda^{-2}}}\Bigg|_{\lambda=1}^{\lambda=f} && (2.122)\\
H^{(0)} &= \sqrt{f^2+4D^2}-\sqrt{1+4D^2} && (2.123)\\
H^{(2)} &= -\frac{4D^2\lambda^{-1}}{(1+4D^2\lambda^{-2})^{3/2}} && (2.124)
\end{aligned}
$$

For $D > 0$, these give

$$
\begin{aligned}
\frac{T_{kk}}{2} &\approx \ln\left(\frac{\sqrt{f^2+4D^2}+2|D|}{f(\sqrt{1+4D^2}+2|D|)}\right)-\frac{D(2+4D^2\lambda^{-2})}{5\lambda(1+4D^2\lambda^{-2})^{3/2}}\Bigg|_{\lambda=1}^{\lambda=f} && (2.125)\\
T_{eqv} &\approx \sqrt{1+4D^2}-\sqrt{f^2+4D^2}+\frac{2D^2}{5\lambda(1+4D^2\lambda^{-2})^{3/2}}\Bigg|_{\lambda=1}^{\lambda=f} && (2.126)
\end{aligned}
$$

the last terms in the above equations are of second order terms. They can be dropped for a fairly good first order result since they are small with respect to the first order terms. This results

$$
\Phi_{spherical} = \frac{\Sigma_{eqv}^2}{\sigma_Y^2}+2f\cosh\left(-\frac{3}{2}\frac{\Sigma_h}{\sigma_Y}\right)-1-f^2=0 \qquad (2.127)
$$

that is the first order yield function for a spherical void configuration where f is void volume fraction, σ_Y is tensile flow stress in matrix material,

$$
\begin{aligned}
\Sigma_{eqv} &= T_{eqv}\sigma_Y=\left(\frac{3}{2}\Sigma'_{ij}\Sigma'_{ij}\right)^{1/2}, && (2.128a)\\
\Sigma_h &= -\frac{\Sigma_{kk}}{3}=-\frac{\Sigma_{11}+\Sigma_{22}+\Sigma_{33}}{3}, && (2.128b)\\
\Sigma'_{ij} &= \Sigma_{ij}-\delta_{ij}\frac{\Sigma_{kk}}{3}. && (2.128c)
\end{aligned}
$$

Σ_{eqv}, Σ_h, Σ'_{ij} are macroscopic equivalent von Mises, hydrostatic and deviatoric stresses.

2.3. Modifications to Gurson Yield Function for Spherical Void

Gurson yield function for a spherical void Equation 2.127 was modified introducing new coefficients namely yield function coefficients q_is (i=1,2,3) by Tvergaard [26, 27] as shown in below equation, since in its original form the complete loss of material stress carrying capacity was not predicted at a realistic value of void volume fraction.

$$\Phi_{modified\,1} = \frac{\Sigma_{eqv}^2}{\sigma_Y^2} + 2q_1 f \cosh\left(- q_2 \frac{3}{2}\frac{\Sigma_h}{\sigma_Y}\right) - 1 - q_3 f^2 = 0 \qquad (2.129)$$

In this case stress carrying capacity vanishes (Σ_{eqv}=0, Σ_h=0), when void volume fraction f equals to $\frac{q_1 + \sqrt{q_1^2 - q_3}}{q_3}$. Tvergaard [26, 27] showed that agreement in numerical studies is improved considerably for q_1=1.5, q_2=1 and $q_3 = q_1^2$.

The yield function Equation 2.129 was subsequently remodified by Tvergaard and Needleman [28] as follows:

$$\Phi_{modified\,2} = \frac{\Sigma_{eqv}^2}{\sigma_Y^2} + 2q_1 f^* \cosh\left(- q_2 \frac{3}{2}\frac{\Sigma_h}{\sigma_Y}\right) - 1 - q_3 f^{*\,2} = 0 \qquad (2.130)$$

where f^* represents the modified damage parameter which accounts for acceleration of loss of stress carrying capacity due to void coalescence. f^* is defined in terms of void volume fraction f by

$$f^*(f) = \begin{cases} f & \text{if } f \leq f_c, \\ f_c + \dfrac{f_U - f_c}{f_F - f_c}(f - f_c) & \text{if } f_c < f \leq f_F, \end{cases} \qquad (2.131)$$

where $f_U = \frac{q_1 + \sqrt{q_1^2 - q_3}}{q_3}$ is the ultimate value of void volume fraction at which the stress carrying capacity vanishes (Σ_{eqv}=0, Σ_h=0), f_c is the critical void volume fraction at which an accelerated void growth starts (it is also called initiation of void coalescence), and f_F is the failure void volume fraction.

The evolution of void volume fraction during an increment of deformation was expressed both in terms of growth of existing voids, and nucleation of new voids by Tvergaard and Needleman [28] as follows:

$$\dot{f} = (\dot{f})_{growth} + (\dot{f})_{nucleation} \tag{2.132}$$

where superimposed " ˙ " implies time derivative. Growth and nucleation parts were described by

$$\begin{aligned} (\dot{f})_{growth} &= (1-f)\,\dot{\epsilon}^P_{kk} && (2.133) \\ (\dot{f})_{nucleation} &= A\,\dot{\epsilon}^P_{eqv} + B_1\,\dot{\sigma}_{eqv} + B_2\,\dot{\sigma}_{kk}/3 && (2.134) \end{aligned}$$

where $\dot{\epsilon}^P_{kk}$, $\dot{\sigma}_{kk}$ are the trace of plastic strain rate and the trace of stress rate, respectively, and $\dot{\epsilon}^P_{eqv}$, $\dot{\sigma}_{eqv}$ are the equivalent plastic strain rate and equivalent stress rate, respectively. The growth term in Equation 2.133 enforces incompressibility of the matrix material. Void nucleation occurs due to interfacial separation of inclusions, and these inclusions could be secondary phase particles that are added intentionally to improve specific properties of the material or impurities which do not serve improvement in material properties [33]. Nucleation of voids have strain and stress controlled parts that are denoted by coefficients A, B_1 and B_2. A is suggested that nucleation follows a normal distribution by Chu and Needleman [40] as follows:

$$A = \frac{f_n}{s_n\sqrt{2\pi}} \exp\left[-\frac{1}{2}\left(\frac{\epsilon^P_{eqv} - \epsilon_n}{s_n}\right)^2\right] \tag{2.135}$$

where s_n is the standard deviation and ϵ_n is the mean of the distribution, f_n is the void volume fraction of the void nucleating particles. B_1 and B_2 are also suggested that nucleation follows a normal distribution by Chu and Needleman [40] as follows:

$$B_1 = B_2 = \frac{f_n}{s_n\sigma_0\sqrt{2\pi}} \exp\left[-\frac{1}{2}\left(\frac{\sigma_{eqv} + \sigma_{kk}/3 - \sigma_n}{s_n\sigma_0}\right)^2\right] \tag{2.136}$$

where s_n is the standard deviation and σ_n is the mean of the distribution, f_n is the void volume fraction of the void nucleating particles, and σ_0 is the initial tensile flow stress of the matrix material.

2.4. Gurson Yield Function for FGMs

In this section, an attempt on obtaining a yield function in closed form analytically similar to the one proposed by Gurson [24, 25] for a cylindrical void is presented where the medium is non-homogeneous and shear modulus G varies radially. The velocity and resulting strain rate fields are again separated into three parts as was done in section 2.1:

(i) Plane strain,
(ii) Uniform axial deformation,
(iii) General dilatation.

Velocity, strain rate fields for each part are derived separately in the following sections for radially varying G.

2.4.1. Plane Strain

The plane strain problem with no volumetric change is solved assuming an angular dependence for stresses and velocities same as in Equations 2.5a - 2.5e given in section 2.1.1. Equilibrium equations along r and θ axes, and incompressibility relation which are given in section 2.1.1, in Equations 2.6 and 2.7 are also same in the following derivations, but two constitutive relations are:

$$\bar{\sigma}_{\theta\theta} - \bar{\sigma}_{rr} = 2G\left(\frac{2\bar{v}_\theta + \bar{v}_r}{r} - \frac{\mathrm{d}\bar{v}_r}{\mathrm{d}r}\right), \tag{2.137a}$$

$$\bar{\sigma}_{r\theta} = G\left(\frac{\mathrm{d}\bar{v}_\theta}{\mathrm{d}r} - \frac{2\bar{v}_r + \bar{v}_\theta}{r}\right) \tag{2.137b}$$

are different than Equations 2.8a and 2.8b where G is shear modulus and it is assumed to be of the $G_0 r^n$ form. Equilibrium equations namely Equations 2.6 are rewritten substituting constitutive relations, Equations 2.137a and 2.137b, and using incompressibility relation, Equation 2.7. After these substitutions, the following ordinary differential equation in terms of $\bar{v}_r$ is obtained.

$$r^4\frac{\mathrm{d}^4\bar{v}_r}{\mathrm{d}r^4}+2(n+3)r^3\frac{\mathrm{d}^3\bar{v}_r}{\mathrm{d}r^3}+(n^2+6n-3)r^2\frac{\mathrm{d}^2\bar{v}_r}{\mathrm{d}r^2}+(n^2-8n-9)r\frac{\mathrm{d}\bar{v}_r}{\mathrm{d}r}+(3n^2+9)\bar{v}_r=0 \quad (2.138)$$

The general solution for Equation 2.138 is

$$\begin{aligned}\bar{v}_r \;=\;& D_1 r^{\left(\frac{-n+\sqrt{n^2+20+4\sqrt{16-3n^2}}}{2}\right)}+D_2 r^{\left(\frac{-n+\sqrt{n^2+20-4\sqrt{16-3n^2}}}{2}\right)}\\ &+D_3 r^{\left(\frac{-n-\sqrt{n^2+20-4\sqrt{16-3n^2}}}{2}\right)}+D_4 r^{\left(\frac{-n-\sqrt{n^2+20+4\sqrt{16-3n^2}}}{2}\right)} \qquad (2.139)\end{aligned}$$

where D_i are constants. $\bar{v}_\theta$ is obtained substituting Equation 2.139 into incompressibility relation, Equation 2.7.

$$\begin{aligned}\bar{v}_\theta \;=\;& -\frac{1}{2}D_1\left(1+\frac{-n+\sqrt{n^2+20+4\sqrt{16-3n^2}}}{2}\right)r^{\left(\frac{-n+\sqrt{n^2+20+4\sqrt{16-3n^2}}}{2}\right)}\\ &-\frac{1}{2}D_2\left(1+\frac{-n+\sqrt{n^2+20-4\sqrt{16-3n^2}}}{2}\right)r^{\left(\frac{-n+\sqrt{n^2+20-4\sqrt{16-3n^2}}}{2}\right)}\\ &-\frac{1}{2}D_3\left(1+\frac{-n-\sqrt{n^2+20-4\sqrt{16-3n^2}}}{2}\right)r^{\left(\frac{-n-\sqrt{n^2+20-4\sqrt{16-3n^2}}}{2}\right)}\\ &-\frac{1}{2}D_4\left(1+\frac{-n-\sqrt{n^2+20+4\sqrt{16-3n^2}}}{2}\right)r^{\left(\frac{-n-\sqrt{n^2+20+4\sqrt{16-3n^2}}}{2}\right)} \qquad (2.140)\end{aligned}$$

Combining the equations above with assumed velocities in Equations 2.5d and 2.5e, approximate velocities v_r and v_θ under plane stress conditions are obtained.

$$\begin{aligned}v_r \;=\;& \Bigg[D_1 r^{\left(\frac{-n+\sqrt{n^2+20+4\sqrt{16-3n^2}}}{2}\right)}+D_2 r^{\left(\frac{-n+\sqrt{n^2+20-4\sqrt{16-3n^2}}}{2}\right)}\\ &+D_3 r^{\left(\frac{-n-\sqrt{n^2+20-4\sqrt{16-3n^2}}}{2}\right)}+D_4 r^{\left(\frac{-n-\sqrt{n^2+20+4\sqrt{16-3n^2}}}{2}\right)}\Bigg]\cos(2\theta), \qquad (2.141a)\end{aligned}$$

$$\begin{aligned} v_\theta \;=\; -\frac{1}{2}\Bigg[& D_1\left(1+\frac{-n+\sqrt{n^2+20+4\sqrt{16-3n^2}}}{2}\right)r^{\left(\frac{-n+\sqrt{n^2+20+4\sqrt{16-3n^2}}}{2}\right)} \\ & +D_2\left(1+\frac{-n+\sqrt{n^2+20-4\sqrt{16-3n^2}}}{2}\right)r^{\left(\frac{-n+\sqrt{n^2+20-4\sqrt{16-3n^2}}}{2}\right)} \\ & +D_3\left(1+\frac{-n-\sqrt{n^2+20-4\sqrt{16-3n^2}}}{2}\right)r^{\left(\frac{-n-\sqrt{n^2+20-4\sqrt{16-3n^2}}}{2}\right)} \\ & +D_4\left(1+\frac{-n-\sqrt{n^2+20+4\sqrt{16-3n^2}}}{2}\right)r^{\left(\frac{-n-\sqrt{n^2+20+4\sqrt{16-3n^2}}}{2}\right)}\Bigg]\sin(2\theta). \end{aligned} \tag{2.141b}$$

The differences between the velocity field obtained for non-homogeneous medium with a radially varying shear modulus here in Equations 2.141a-2.141b and the one obtained for homogeneous medium in Equations 2.12a-2.12b in section 2.1.1, are the exponents and coefficients of rs that includes n which is varying exponent of shear modulus. When n is taken to be zero in Equations 2.141a-2.141b that introduces homogeneity, the velocity field derived here yields the one obtained in section 2.1.1.

2.4.2. Uniform Axial Deformation

The macroscopic strain rate field, $\dot{E}_{ij}$ which is the volumetric average of microscopic strain rate field is defined same as to the one that is done in section 2.1.2 and given in Equation 2.14. The same assumptions are accepted as stated in section 2.1.2. They are repeated here to be able to provide continuity. Microscopic and macroscopic strain rates along the axial direction are equal for uniform axial deformation. Shearing rates along axial direction is related to the macroscopic strain rates $\dot{E}_{13}$ and $\dot{E}_{23}$. A rotation of the $r-\theta$ plane around the axial direction, z, that results in $\dot{E}_{13}$=0 can be determined. This is considered to simplify equations without loosing generality. New polar angle γ is measured from the new 2^* axis. The assumed velocity field for this new coordinate system here is same as Equations 2.15a-2.15c given in section 2.1.2. Equilibrium equation along axial direction, two strain rate-velocity relations are also same as Equations 2.16 and 2.18 given in section 2.1.2, but two constitutive relations:

$$\sigma_{rz} = 2G\dot{\epsilon}_{rz}, \quad \sigma_{\gamma z} = 2G\dot{\epsilon}_{\gamma z}, \tag{2.142}$$

are different than Equation 2.17, where G is shear modulus and it is assumed to be of the $G_0 r^n$ form.

When combined with Equations 2.15a-2.15c and 2.18, Equation 2.142 becomes

$$\sigma_{rz} = G\,\cos(\gamma)\left(\bar{v}_r + \frac{\mathrm{d}\bar{v}_z}{\mathrm{d}r}\right) \tag{2.143a}$$

$$\sigma_{\gamma z} = -G\,\sin(\gamma)\left(\bar{v}_r + \frac{\bar{v}_z}{r}\right) \tag{2.143b}$$

Using above equations, $G = G_0 r^n$, and the fact that σ_{zz} is not function of z, equilibrium equation along axial direction, Equation 2.16 becomes

$$r^2\frac{\mathrm{d}^2\bar{v}_z}{\mathrm{d}r^2} + r(n+1)\frac{\mathrm{d}\bar{v}_z}{\mathrm{d}r} - \bar{v}_z + f(r) + r^2\frac{\mathrm{d}\bar{v}_r}{\mathrm{d}r} + rn\bar{v}_r - f(r) = 0 \tag{2.144}$$

$f(r)$ is an arbitrary function of r. $\bar{v}_r$ and $\bar{v}_z$ are independent quantities, therefore they go to zero separately. Then, the general solution which yields zero $\dot{\epsilon}_{rr}$, $\dot{\epsilon}_{\gamma\gamma}$ and $\dot{\epsilon}_{r\gamma}$ (this is required to satisfy the boundary conditions) for Equation 2.144 is

$$\bar{v}_r = constant \equiv V^*_{32} \tag{2.145a}$$

$$\bar{v}_z = D_5 r^{\frac{-n+\sqrt{n^2+4}}{2}} + D_6 r^{\frac{-n-\sqrt{n^2+4}}{2}} - V^*_{32} r \tag{2.145b}$$

where D_5, D_6 are constants and V^*_{32} is the shearing velocity per unit axial length.

Combining Equations 2.15 and 2.145, velocity field due to uniform axial deformation is given

$$v_r = V^*_{32}\, z\, \cos(\gamma), \tag{2.146a}$$

$$v_\gamma = -V_{32}^* \, z \, \sin(\gamma), \tag{2.146b}$$

$$v_z = (D_5 r^{\frac{-n+\sqrt{n^2+4}}{2}} + D_6 r^{\frac{-n-\sqrt{n^2+4}}{2}} - V_{32}^* r) \, \cos(\gamma). \tag{2.146c}$$

The difference between the velocity field obtained here and the one obtained in section 2.1.2 is at axial velocity, v_z. Exponents of r in v_z for non-homogeneous medium includes n, and one more extra term that is $V_{32}^* r$ is included. When n is taken to be zero, both velocity fields obtained here and in section 2.1.2 are equal.

2.4.3. General Dilatation

Same procedure in section 2.1.3 is followed while obtaining velocity field considering general dilatation. No angular dependence and uniform axial deformation is considered. Strain rate field is same as given in Equation 2.25 in section 2.1.3. Equation 2.25 results the same incompressibility relation as it is given in Equation 2.26. The general solution for $\dot{\epsilon}_{kk} = 0$, is same both for homogeneous and non-homogeneous mediums, and it is

$$v_r^D = D_7 r^{-1} - \frac{r}{2} \dot{E}_{33}, \tag{2.147a}$$

$$v_\theta^D = 0, \tag{2.147b}$$

$$v_z^D = \dot{E}_{33} z. \tag{2.147c}$$

where D_7 is constant. This is because no constitutive equation is used while obtaining velocity field considering general dilatation.

2.4.4. General Velocity and Strain Rate Fields

One gets the general form of the velocity and strain rate fields superposing derived velocity and strain rate fields from separated parts that are *i*) plane strain, *ii*) uniform axial deformation and *iii*) general dilatation. Velocity field is

$$\begin{aligned} v_r &= (D_1 r^M + D_2 r^N + D_3 r^{-N} + D_4 r^{-M})\, r^{-\frac{n}{2}} \cos(2\theta) \\ &\quad + D_7 r^{-1} - \frac{r}{2}\dot{E}_{33} + V_{32}^*\, z\, \cos(\gamma), \end{aligned} \tag{2.148a}$$

$$\begin{aligned} v_\theta &= -\frac{1}{2}\Bigg[D_1\bigg(1-\frac{n}{2}+M\bigg)r^M + D_2\bigg(1-\frac{n}{2}+N\bigg)r^N + D_3\bigg(1-\frac{n}{2}-N\bigg)r^{-N} \\ &\quad + D_4\bigg(1-\frac{n}{2}-M\bigg)r^{-M}\Bigg]\, r^{-\frac{n}{2}} \sin(2\theta) - V_{32}^*\, z\, \sin(\gamma), \end{aligned} \tag{2.148b}$$

$$v_z = (D_5 r^{\frac{-n+\sqrt{n^2+4}}{2}} + D_6 r^{\frac{-n-\sqrt{n^2+4}}{2}} - V_{32}^* r)\, \cos(\gamma) + \dot{E}_{33} z. \tag{2.148c}$$

where $M = \dfrac{\sqrt{n^2+20+4\sqrt{16-3n^2}}}{2}$, and $N = \dfrac{\sqrt{n^2+20-4\sqrt{16-3n^2}}}{2}$.

Strain rate field is

$$\begin{aligned} \dot{\epsilon}_{rr} &= \frac{\partial v_r}{\partial r} \\ &= \Bigg[D_1\bigg(-\frac{n}{2}+M\bigg)r^{M-1} + D_2\bigg(-\frac{n}{2}+N\bigg)r^{N-1} + D_3\bigg(-\frac{n}{2}-N\bigg)r^{-N-1} \\ &\quad + D_4\bigg(-\frac{n}{2}-M\bigg)r^{-M-1}\Bigg]\, r^{-\frac{n}{2}} \cos(2\theta) - D_7 r^{-2} - \frac{\dot{E}_{33}}{2}, \end{aligned} \tag{2.149a}$$

$$\begin{aligned} \dot{\epsilon}_{\theta\theta} &= \frac{1}{r}\frac{\partial v_\theta}{\partial \theta} + \frac{v_r}{r} \\ &= \Bigg[D_1\bigg(\frac{n}{2}-M\bigg)r^{M-1} + D_2\bigg(\frac{n}{2}-N\bigg)r^{N-1} + D_3\bigg(\frac{n}{2}+N\bigg)r^{-N-1} \\ &\quad + D_4\bigg(\frac{n}{2}+M\bigg)r^{-M-1}\Bigg]\, r^{-\frac{n}{2}} \cos(2\theta) + D_7 r^{-2} - \frac{\dot{E}_{33}}{2}, \end{aligned} \tag{2.149b}$$

$$\dot{\epsilon}_{zz} = \frac{\partial v_z}{\partial z} = \dot{E}_{33}, \tag{2.149c}$$

$$\begin{aligned}
\dot{\epsilon}_{r\theta} &= \frac{1}{2}\left(\frac{1}{r}\frac{\partial v_r}{\partial \theta} + \frac{\partial v_\theta}{\partial r} - \frac{v_\theta}{r}\right) \\
&= \Bigg[D_1\left(-\frac{3}{4} - \left(\frac{-n+2M}{4}\right)^2\right)r^{M-1} + D_2\left(-\frac{3}{4} - \left(\frac{-n+2N}{4}\right)^2\right)r^{N-1} \\
&\quad + D_3\left(-\frac{3}{4} - \left(\frac{-n-2N}{4}\right)^2\right)r^{-N-1} + D_4\left(-\frac{3}{4} - \left(\frac{-n-2M}{4}\right)^2\right)r^{-M-1}\Bigg] \\
&\quad r^{-\frac{n}{2}}\sin(2\theta), \qquad (2.149\text{d})
\end{aligned}$$

$$\begin{aligned}
\dot{\epsilon}_{rz} &= \frac{1}{2}\left(\frac{\partial v_z}{\partial r} + \frac{\partial v_r}{\partial z}\right) \\
&= \frac{1}{2}\Bigg[D_5\left(\frac{-n+\sqrt{n^2+4}}{2}\right)r^{\frac{-n+\sqrt{n^2+4}}{2}-1} \\
&\quad + D_6\left(\frac{-n-\sqrt{n^2+4}}{2}\right)r^{\frac{-n-\sqrt{n^2+4}}{2}-1}\Bigg]\cos(\gamma), \qquad (2.149\text{e})
\end{aligned}$$

$$\begin{aligned}
\dot{\epsilon}_{\theta z} &= \frac{1}{2}\left(\frac{\partial v_\theta}{\partial z} + \frac{1}{r}\frac{\partial v_z}{\partial \theta}\right) \\
&= -\frac{1}{2}\left[D_5 r^{\frac{-n+\sqrt{n^2+4}}{2}-1} + D_6 r^{\frac{-n-\sqrt{n^2+4}}{2}-1}\right]\sin(\gamma). \qquad (2.149\text{f})
\end{aligned}$$

Velocity and strain rate fields that are obtained from general dilatation part are same both for homogeneous material and FGM where shear modulus is $G_0 r^n$. Differences between homogeneous material and FGM in terms of these fields obtained here are the exponents of r as can be seen when the Equations 2.29, 2.148, and Equations 2.30, 2.149 are compared.

When these velocity and strain rate fields are compared to the ones obtained for homogeneous materials.

Boundary conditions on the outer surface for velocities v_i in terms of macroscopic strain rates must be obtained in order to determine the constants D_1 through D_7 in Equations 2.148-2.149. In general, boundary conditions are

$$v_i\big|_s = \dot{E}_{ik} x_k\big|_s. \qquad (2.150)$$

Therefore,

$$v_r\Big|_s = \dot{E}_{rr} b + \dot{E}_{rz} z, \tag{2.151a}$$

$$v_\theta\Big|_s = \dot{E}_{\theta r} b + \dot{E}_{\theta z} z, \tag{2.151b}$$

$$v_z\Big|_s = \dot{E}_{zr} b + \dot{E}_{zz} z. \tag{2.151c}$$

Before obtaining boundary conditions, a transformation is required between cartesian and polar coordinate systems. The transformation is not ordinary since θ is measured from the (2) axis instead of the (1) axis (See Figure 2.2).

Transformation matrix for the coordinate systems in Figure 2.2 is

$$\boldsymbol{T} = \begin{bmatrix} \cos(\frac{\pi}{2}+\theta) & \cos(\theta) \\ \cos(\pi+\theta) & \cos(\frac{\pi}{2}+\theta) \end{bmatrix} = \begin{bmatrix} -\sin(\theta) & \cos(\theta) \\ -\cos(\theta) & -\sin(\theta) \end{bmatrix} \tag{2.152}$$

Transformations for a 1^{st}-order tensor, $\boldsymbol{v}$ which is velocity and for a 2^{nd}-order tensor, $\dot{\boldsymbol{E}}$ which is macroscopic strain rate are given as follows

$$\boldsymbol{v}_{polar} = \boldsymbol{T}\boldsymbol{v}_{cart.} \tag{2.153}$$

$$\dot{\boldsymbol{E}}_{polar} = \boldsymbol{T}\dot{\boldsymbol{E}}_{cart.}\boldsymbol{T}^T \tag{2.154}$$

Using the above transformations, one gets

$$v_r = -v_1 \sin(\theta) + v_2 \cos(\theta), \tag{2.155a}$$

$$v_\theta = -v_1 \cos(\theta) - v_2 \sin(\theta), \tag{2.155b}$$

$$\dot{E}_{rr} = \dot{E}_{11} \sin^2(\theta) + \dot{E}_{22} \cos^2(\theta) - 2\dot{E}_{12} \sin(\theta)\cos(\theta), \tag{2.156a}$$

$$\dot{E}_{\theta\theta} = \dot{E}_{11} \cos^2(\theta) + \dot{E}_{22} \sin^2(\theta) + 2\dot{E}_{12} \sin(\theta)\cos(\theta), \tag{2.156b}$$

$$\dot{E}_{r\theta} = (\dot{E}_{11} - \dot{E}_{22}) \sin(\theta)\cos(\theta) + \dot{E}_{12}(\sin^2(\theta) - \cos^2(\theta)). \tag{2.156c}$$

Similarly, $\dot{E}_{rz}$ and $\dot{E}_{\theta z}$ are obtained using an alike transformation matrix $\boldsymbol{T}$.

$$\begin{aligned}
\dot{E}_{rz} &= -V_{31}^{*}\sin(\gamma) + V_{32}^{*}\cos(\gamma) && \text{(2.157a)}\\
\dot{E}_{\theta z} &= -V_{31}^{*}\cos(\gamma) - V_{32}^{*}\sin(\gamma) && \text{(2.157b)}\\
\dot{E}_{zz} &= \dot{E}_{33} && \text{(2.157c)}
\end{aligned}$$

The axial strain rates are obtained considering uniform axial deformation in the section 2.4.2 and these derivations are handled in a different coordinate system denoted by * where $\dot{E}_{13}$=0. Therefore $\dot{E}_{rz}$ and $\dot{E}_{\theta z}$ are expressed in terms of shearing velocities per unit axial length V_{31}^{*} and V_{32}^{*}.

Substituting Equations 2.156-2.157 into Equations 2.151a-2.151c and taking into account that $\dot{E}_{12}$ and V_{31}^{*} (remember that $\dot{E}_{13}$=0 in * superscripted coordinate system) are 0, boundary conditions are given

$$\begin{aligned}
v_r\Big|_{r=b} &= \frac{1}{2}(\dot{E}_{22} - \dot{E}_{11})b\cos(2\theta) + \frac{1}{2}(\dot{E}_{22} + \dot{E}_{11})b + V_{32}^{*}z\cos(\gamma), && \text{(2.158a)}\\
v_\theta\Big|_{r=b} &= -\frac{1}{2}(\dot{E}_{22} - \dot{E}_{11})b\sin(2\theta) - V_{32}^{*}z\sin(\gamma), && \text{(2.158b)}\\
v_z\Big|_{r=b} &= V_{23}^{*}b\cos(\gamma) + \dot{E}_{33}z && \text{(2.158c)}
\end{aligned}$$

where V_{23}^{*} is a shear velocity parallel to the (3) axis and it is similar to V_{32}^{*}. Another boundary condition is zero shear strain rate on the void surface.

$$\begin{aligned}
\dot{\epsilon}_{r\theta}|_{r=a} &= 0 && \text{(2.159a)}\\
\dot{\epsilon}_{rz}|_{r=a} &= 0 && \text{(2.159b)}
\end{aligned}$$

General velocity field Equations 2.148 and velocity boundary condition Equations 2.158 give

$$\begin{aligned} D_1 b^M + D_2 b^N + D_3 b^{-N} + D_4 b^{-M} &= \frac{1}{2}(\dot{E}_{22} - \dot{E}_{11}) b^{\frac{n+2}{2}}, \quad (2.160a) \\ D_1\left(1 - \frac{n}{2} + M\right) b^M + D_2\left(1 - \frac{n}{2} + N\right) b^N & \\ + D_3\left(1 - \frac{n}{2} - N\right) b^{-N} + D_4\left(1 - \frac{n}{2} - M\right) b^{-M} &= (\dot{E}_{22} - \dot{E}_{11}) b^{\frac{n+2}{2}}, \quad (2.160b) \\ D_7 b^{-1} - \frac{1}{2}\dot{E}_{33} b &= \frac{1}{2}(\dot{E}_{11} + \dot{E}_{22}) b, \quad (2.160c) \\ D_5 b^{\frac{-n+\sqrt{n^2+4}}{2}} + D_6 b^{\frac{-n-\sqrt{n^2+4}}{2}} &= (V^*_{23} + V^*_{32}) b. \quad (2.160d) \end{aligned}$$

It is obtained that

$$D_7 = \frac{1}{2}(\dot{E}_{11} + \dot{E}_{22} + \dot{E}_{33}) b^2 \qquad (2.161)$$

from Equation 2.160c. Using shear rate boundary conditions Equations 2.159a and 2.159b, $\dot{\epsilon}_{r\theta}$ and $\dot{\epsilon}_{rz}$ in Equations 2.149d-2.149e give

$$\begin{aligned} D_1\left(-\frac{3}{4} - \left(\frac{-n+2M}{4}\right)^2\right) a^M + D_2\left(-\frac{3}{4} - \left(\frac{-n+2N}{4}\right)^2\right) a^N & \\ + D_3\left(-\frac{3}{4} - \left(\frac{-n-2N}{4}\right)^2\right) a^{-N} + D_4\left(-\frac{3}{4} - \left(\frac{-n-2M}{4}\right)^2\right) a^{-M} &= 0, \\ & \qquad (2.162a) \\ D_5\left(\frac{-n+\sqrt{n^2+4}}{2}\right) a^{\frac{-n+\sqrt{n^2+4}}{2}-1} + D_6\left(\frac{-n-\sqrt{n^2+4}}{2}\right) a^{\frac{-n-\sqrt{n^2+4}}{2}-1} &= 0. \\ & \qquad (2.162b) \end{aligned}$$

D_5 and D_6 are uniquely determined from Equations 2.160d and 2.162b.

$$\begin{aligned} D_5 &= \frac{2a^{-\frac{\sqrt{n^2+4}}{2}} b^{\frac{n+2}{2}} (V^*_{23} + V^*_{32})}{2\left(\frac{b}{a}\right)^{\frac{\sqrt{n^2+4}}{2}} + \left(\frac{a}{b}\right)^{\frac{\sqrt{n^2+4}}{2}} (n^2 + 2 - n\sqrt{n^2+4})} \qquad (2.163) \\ D_6 &= \frac{2a^{\frac{\sqrt{n^2+4}}{2}} b^{\frac{n+2}{2}} (V^*_{23} + V^*_{32})}{2\left(\frac{a}{b}\right)^{\frac{\sqrt{n^2+4}}{2}} + \left(\frac{b}{a}\right)^{\frac{\sqrt{n^2+4}}{2}} (n^2 + 2 + n\sqrt{n^2+4})} \qquad (2.164) \end{aligned}$$

Notice that there are four unknowns, D_1 through D_4 and three Equations 2.160a, 2.160b and 2.162a left. Therefore the system is indeterminate. The minimization of dissipation energy $\dot{W}$ must be considered as well.

$$\dot{W} = \frac{1}{V}\int_V \sigma'_{ij}\dot{\epsilon}_{ij}\, dV = \frac{1}{V}\int_V \sqrt{\frac{2}{3}}\sigma_Y \sqrt{\dot{\epsilon}_{ij}\dot{\epsilon}_{ij}}\, dV. \tag{2.165}$$

If four constants, D_1 through D_4 are solved using Equations 2.160a, 2.160b and 2.162a, minimizing Equation 2.165; a yield function can be obtained with a specifically varying shear modulus where $G = G_0 r^n$. This could not be achieved. Therefore, computational implementation of Gurson - Tvergaard - Needleman model is preferred which would allow the application to a more general FGM.

3. COMPUTATIONAL IMPLEMENTATION OF GURSON - TVERGAARD - NEEDLEMAN MODEL

Gurson - Tvergaard - Needleman (GTN) model is implemented using finite elements for simulation of failure. Some of commercial finite element packages have built-in module for GTN model, and one of these softwares is Abaqus. Abaqus is used in following studies for this purpose. First, required GTN model parameters for simulations are introduced in section 3.1. Failure of a three point bending steel specimen problem that is investigated by Narasimhan *et al.* [33] is revisited for verification of the built-in GTN model module in Abaqus. After verification of the results, GTN model parameter effects on stress-strain response of a uniaxially loaded specimen and mesh sensitivity of the GTN model are investigated in sections 3.3 and 3.4.

3.1. Required Parameters for GTN Model

The name for the built-in module in Abaqus for GTN model is “porous metal plasticity”. Material parameters that are required while using GTN model in Abaqus are listed below, and effects of these parameters on failure are discussed. In Abaqus, one can use 3-D solid, 2-D plane strain and 2-D axisymmetric elements for modeling using GTN model. 2-D plane stress elements are not available for GTN model in Abaqus.

- Elastic properties: Young’s modulus and Poisson’s ratio are inputs.
- Plastic properties: Plastic behavior of the material is identified by tabulating data of yield stress versus plastic strain.
- Density (Explicit): Mass density is required for the explicit solver.
- Yield function coefficients: These coefficients, q_1, q_2 and q_3 characterize the yield function given in Equation 2.129. For typical metals, the ranges of these coefficients are q_1= 1.0 to 1.5, q_2= 1.0, and q_3= = 1.0 to 2.25. The original Gurson yield function given in Equation 2.127 is obtained with q_1= q_2= q_3= 1.0.
- Relative density: The initial relative density of the matrix material, r_0, is defined

as the ratio of the volume of solid material to the total volume of the material where is r_0 equal to 1-f_0 (f_0 is the initial void volume fraction). If there is no void initially, then $r_0 = 1$.

- Critical and failure void volume fractioons (Explicit): GTN model in Abaqus / Explicit allows for progressive failure of elements. In that case, the yield condition is expressed as given in Equation 2.130 where f^* introduces accelerated loss of stress carrying capacity accompanied with void coalescence. f^* is defined in terms of the void volume fraction in Equation 2.131 where f_c is the critical value of void volume fraction. After that value of void volume fraction, f^* increases more rapidly. f_F is the value of void volume fraction at which there is a complete loss of stress carrying capacity in the material. This accelerated void increasing model is only available for the explicit solver. f_c and f_F are user-specified parameters.
- Void nucleation parameters: A plastic strain controlled void nucleation law is assumed as given in Equation 2.134 where A is a function of equivalent plastic strain and $B_1 = B_2 = 0$. The function A is chosen as in Equation 2.135 as suggested by Chu and Needleman [40] so that void nucleation follows a normal distribution about a mean nucleation strain ϵ_n with a standard deviation s_n. f_n denotes the volume fraction of void nucleating particles. The values f_n, s_n and ϵ_n are user-defined parameters.

To summarize GTN model parameters are tabulated in Table 3.1.

3.2. Failure of A Three Point Bending Steel Specimen

Failure of a three point bending steel specimen is studied by Narasimhan *et al.* [33] using two and three dimensional finite element models. Gurson - Tvergaard - Needleman (GTN) failure criterion is used to simulate a continuum elastic-plastic model that accounts for void nucleation and growth to introduce damage accumulation. The problem studied by Narasimhan *et al.* is revisited for the verification of the finite element model to be used. In Section 3.2.1, details of the problem geometry and FE model are represented. A good agreement is observed between the results of the present model and Narasimhan *et al.*'s work in Abaqus is achieved in Section 3.2.2. In Section

Table 3.1. GTN model parameters required by Abaqus

Elastic properties	Elastic modulus	E
	Poisson's ratio	ν
Plastic properties	Yield stress	σ_Y
	Plastic strain	ϵ^P
Density †		ρ
Yield function coefficients		q_1, q_2, q_3
Void volume fraction parameters	Initial relative density (r_0)	1-f_0
	Critical void volume fraction ‡	f_c
	Failure void volume fraction ‡	f_F
Void nucleation parameters	Mean nucleation strain	ϵ_n
	Standard deviation	s_n
	Volume fraction of void nucleating particles	f_n

† Required only for Abaqus/Explicit.

‡ Available only for Abaqus/Explicit.

3.4, mesh refinement is applied and mesh size dependency is observed on failure.

3.2.1. Geometry of the Problem and FE Model

Specimen geometry and in-plane mesh are shown in Figure 3.1 (a-b) respectively. Due to symmetry, quarter and half of the specimen are simulated with symmetry boundary conditions for 3-D and 2-D models, respectively. 3-D model consists of 6 layers in thickness direction. Each layer consists of 320 elements. The layer interfaces are located at $x_3/h = 0$, 0.113, 0.226, 0.339, 0.415 and 0.5 where $x_3/h = 0.5$ indicates the free surface of the specimen. A detailed in-plane mesh near the notch tip is shown in Figure 3.1 (c). The initial notch diameter b_0 is chosen as $h/50$, that is 0.2 mm.

Uniaxial tension response of the material is characterized by a piece-wise power hardening law of the form:

$$\frac{\varepsilon_m}{\varepsilon_0} = \begin{cases} \sigma_Y/\sigma_0 & \sigma_Y \leq \sigma_0 \\ (\sigma_Y/\sigma_0)^{1/n} & \sigma_m > \sigma_0 \end{cases} \tag{3.1}$$

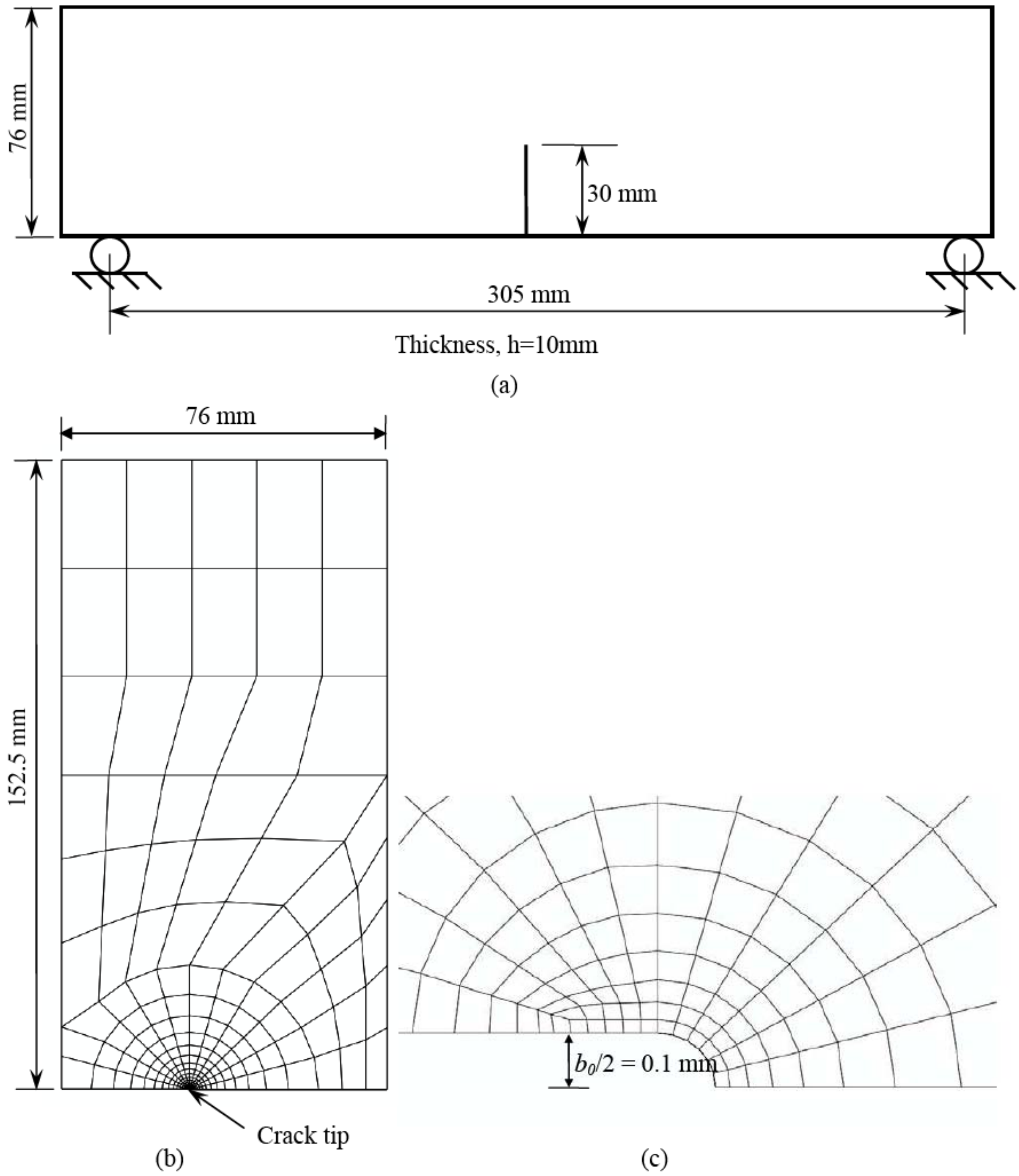

Figure 3.1. (a) Test specimen geometry. (b) In-plane mesh used in finite element analysis. (c) Details of in-plane mesh near notch tip [33]

where hardening exponent $n = 1/22$ and initial yield stress $\sigma_0 = 1030$ MPa. Young's modulus, Poisson's ratio and density of the material are not given in the paper. The type of the steel is AISI 4340. In literature, it is indicated that Young's modulus is between 190 and 210 GPa, Poisson's ratio is between 0.27 and 0.3, and density is between 7700 and 8030 kg/m^3 for AISI 4340 steel. 200 GPa, 0.3, and 7860 kg/m^3 are chosen as Young's modulus, Poisson's ratio, and density, respectively.

The governing equilibrium equations are derived from small-strain approach and stress computations are performed using an explicit algorithm in Abaqus similar to the Narasimhan *et al.*'s study. The matrix yield strength σ_Y and void volume fraction f are held constant after f is reached a value of 0.95 f_F by Narasimhan *et al.* because of numerical difficulties, but Abaqus can overcome with this numerical difficulty. Therefore f reaches f_F at the current study.

3.2.2. Results

Present studies and Narasimhan *et al.*'s results are plotted for 2-D and 3-D simulations in the following sections for comparison.

3.2.2.1. Plane Strain Simulation.

The contours of macroscopic equivalent stress Σ_{eqv} around the notch tip are shown in Figures 3.2 and 3.3 for plane strain. Stress contours are plotted in Figures 3.2 and 3.3 are after incipient material failure, and after the failure of three elements ahead of the notch tip, respectively. From Figures 3.2 and 3.3, it can be noted that the shape of the contours are in good agreement except for their magnitudes. The difference between the values is due to difference between the failure algorithm used by Narasimhan *et al.* and by Abaqus (present study). Narasimhan *et al.* hold yield strength σ_Y and void volume fraction f constant after f reaches $0.95 f_F$ to overcome numerical difficulties when equivalent stress approaches 0. Therefore, lowest value of Σ_{eqv} in Narasimhan's results is not 0 and highest value of Σ_{eqv} is lower than obtained the one in current study.

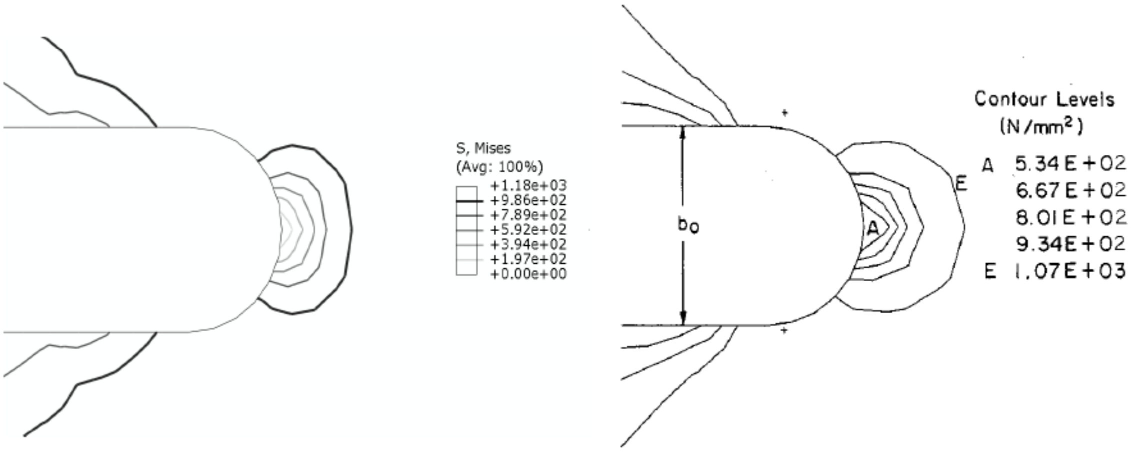

(a) (b)

Figure 3.2. Contours of macroscopic equivalent stress Σ_{eqv} for plane strain after failure of first element for (a) current results, (b) Narasimhan *et al.*'s [33] results

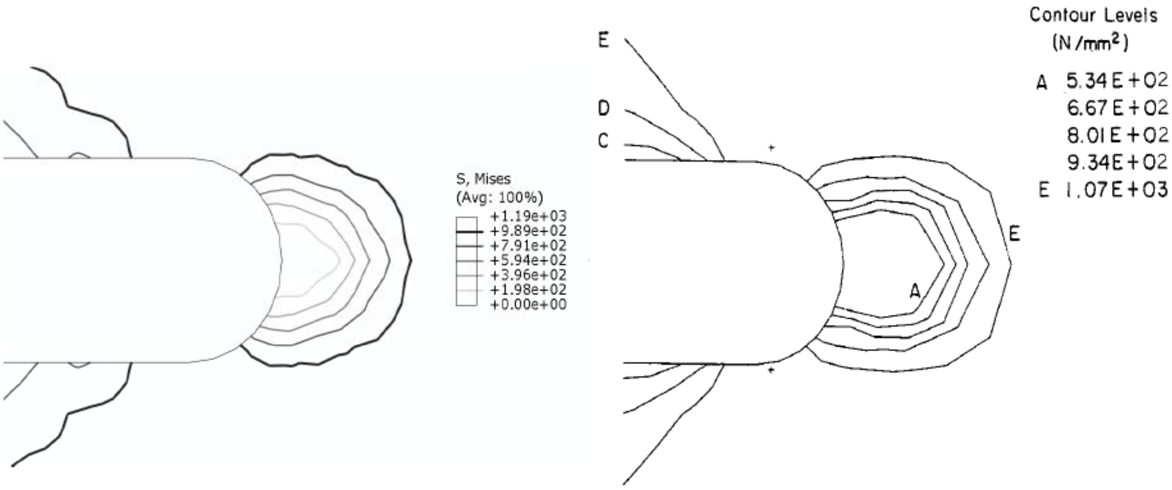

(a) (b)

Figure 3.3. Contours of macroscopic equivalent stress Σ_{eqv} for plane strain after failure of three elements for (a) current results, (b) Narasimhan *et al.*'s [33] results

The contours of void volume fraction around the notch tip are presented in Figures 3.4 and 3.5. Void volume fractions in Figures 3.4 (a) and (b) are calculated following failure of the first element. Figures 3.5 (a) and (b) are after the failure of three elements ahead of the notch tip.

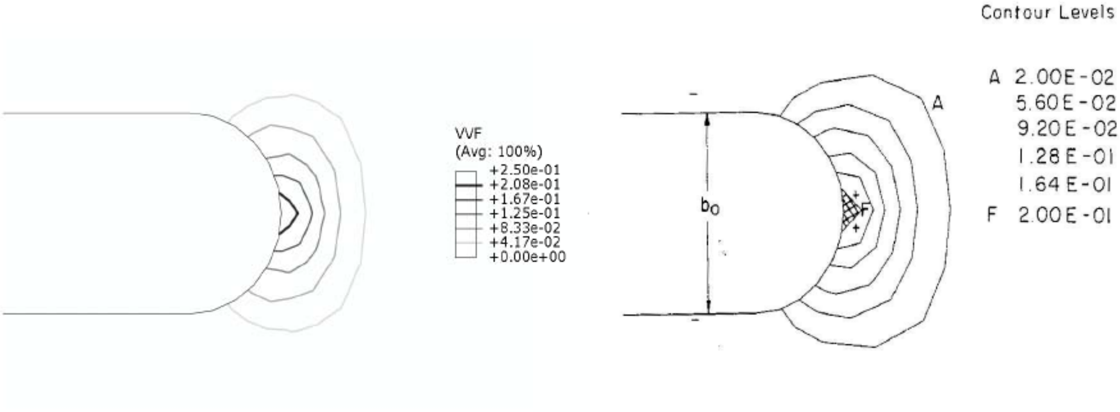

(a) (b)

Figure 3.4. Contours of void volume fraction f for plane strain after failure of first element for (a) current results, b) Narasimhan *et al.*'s [33] results

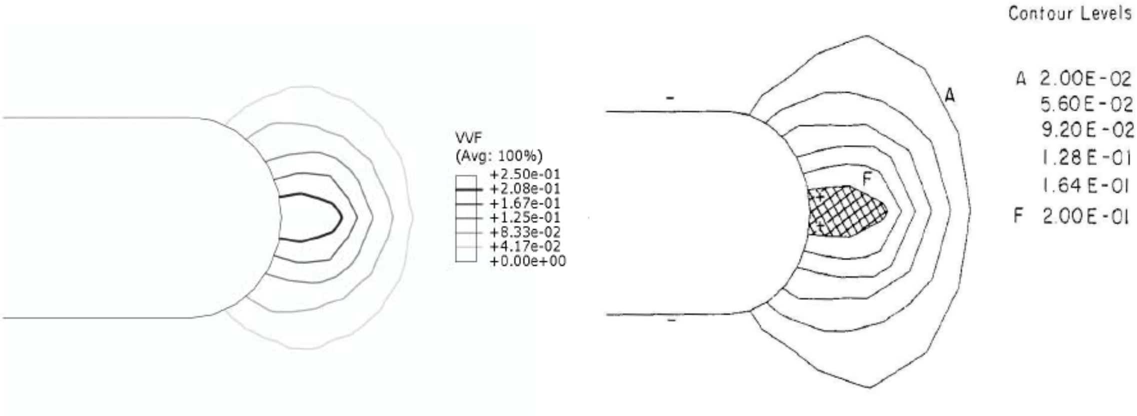

(a) (b)

Figure 3.5. Contours of void volume fraction f for plane strain after failure of three elements for (a) current results, (b) Narasimhan *et al.*'s [33] results

In Figures 3.4 and 3.5, shapes of contours are similar, but the values of void volume fraction differ as was the case for contours of equivalent stress. Note that void volume fraction calculated using Abaqus reaches the chosen value of 0.25 for f_F at failure, but this is not the case for the ones obtained by Narasimhan *et al.*.

3.2.2.2. Three Dimensional Simulation. In Figures 3.6-3.8, contours of equivalent stress near the notch tip are plotted in different planes through the thickness where $x_3/h = 0.057$, 0.282, and 0.485, respectively. It must be recalled that free surface of the specimen is located at $x_3/h = 0.5$.

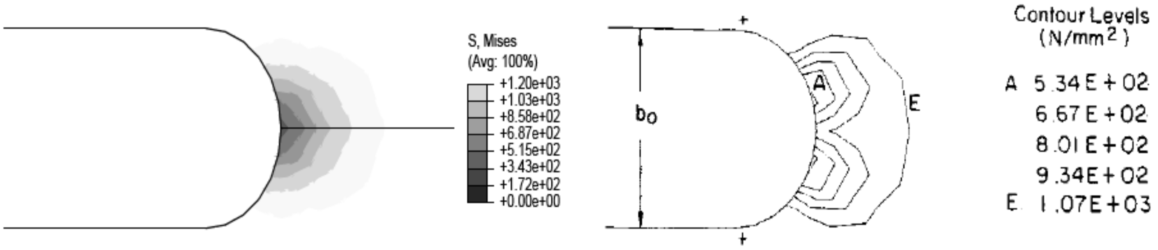

(a) (b)

Figure 3.6. Contours of equivalent stress at $x_3/h = 0.057$ (near center-plane) for (a) current results, (b) Narasimhan *et al.*'s [33] results

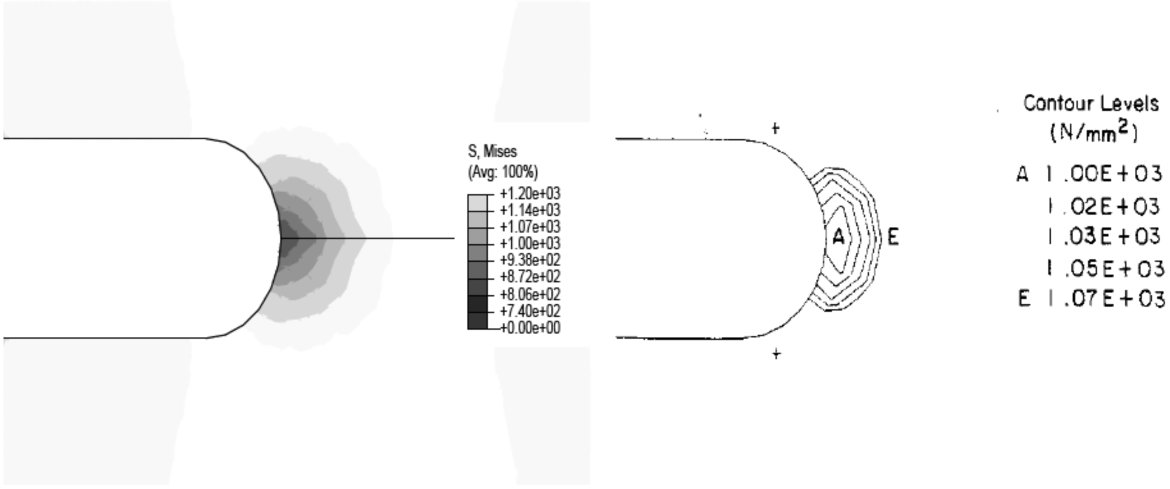

(a) (b)

Figure 3.7. Contours of equivalent stress at $x_3/h = 0.282$ for (a) current results, (b) Narasimhan *et al.*'s [33] results

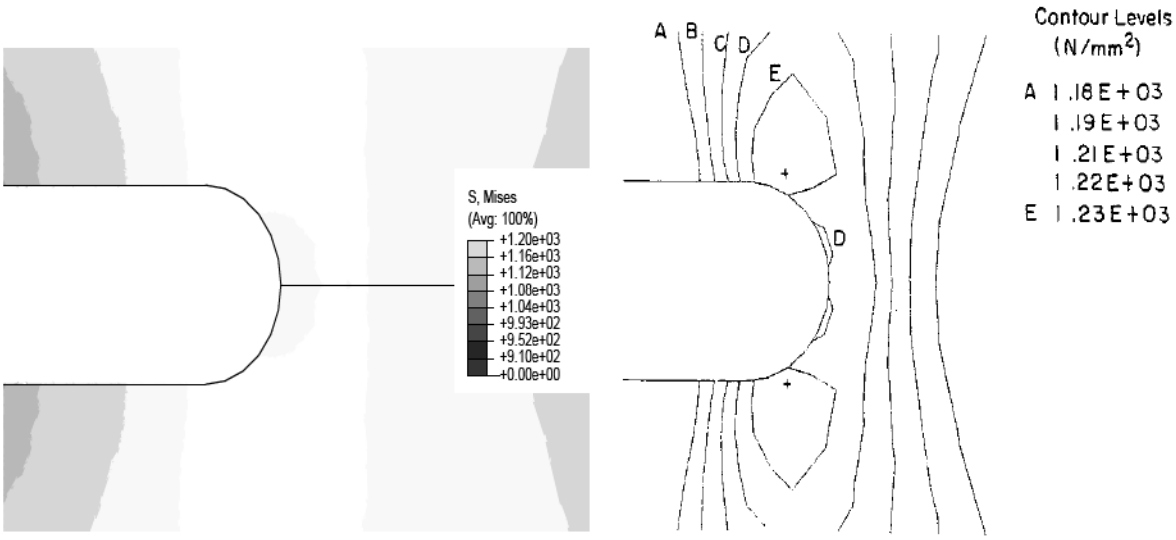

(a) (b)

Figure 3.8. Contours of equivalent stress at $x_3/h = 0.485$ (near free surface) for (a) current results, (b) Narasimhan *et al.*'s [33] results

In Figures 3.9-3.11, contours of void fraction near the notch tip are displayed in different planes through the thickness where x_3/h = 0.057, 0.282, and 0.485, respectively.

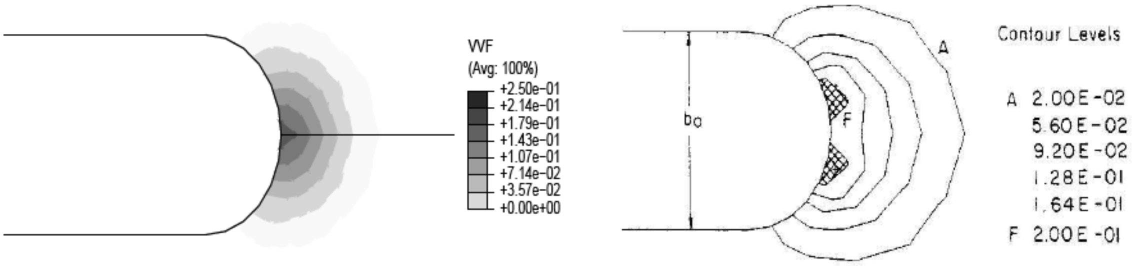

(a) (b)

Figure 3.9. Contours of void volume fraction at $x_3/h = 0.057$ (near center-plane) for (a) current results, (b) Narasimhan *et al.*'s [33] results

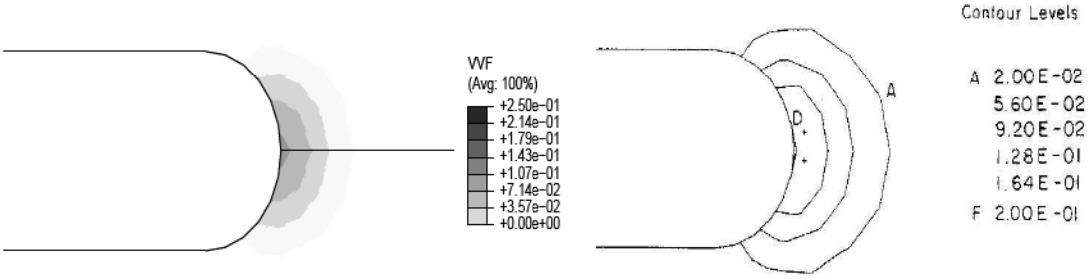

(a) (b)

Figure 3.10. Contours of void volume fraction at $x_3/h = 0.282$ for (a) current results, (b) Narasimhan *et al.*'s [33] results

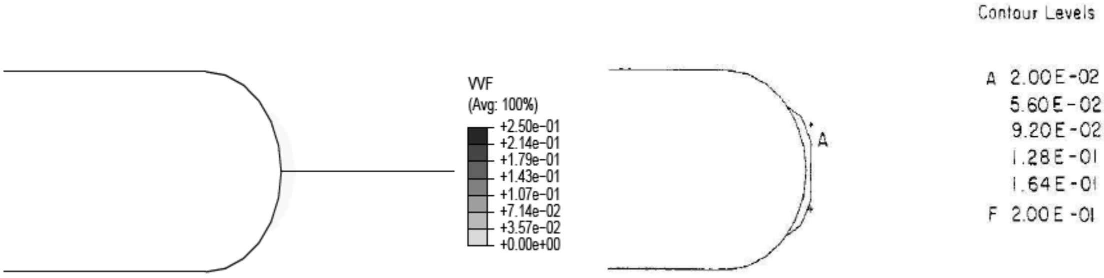

(a) (b)

Figure 3.11. Contours of void volume fraction at $x_3/h = 0.485$ (near free surface) for (a) current results, (b) Narasimhan *et al.*'s [33] results

In the present study, the element that is to fail first is located at the tip of the notch for both 2-D and 3-D simulations as can be seen in Figures 3.4(a) and 3.9(a). However, Narasimhan *et al.*'s results in Figure 3.9(b) show that in 3-D simulation the element adjacent to the symmetry-plane of the specimen exhibits first failure. This indicates an inadmissible bifurcating crack. Otherwise, the magnitudes of void volume fraction show a similar decreasing behavior from center-plane to free surface along thickness direction in both cases. This behavior is an indication of tunneling effect.

3.2.2.3. Variations in Thickness and Radial Directions. Figure 3.12 illustrates the variation of void volume fraction through the thickness of the specimen (x_3/h). Each of the curves corresponds to different radial distances (r/b_0) ahead of the notch tip. Note that center-plane is located at $x_3/h = 0$, and free surface is located at $x_3/h = 0.5$. Higher values of void volume fraction differ, however variation patterns are similar. The difference is due to the difference of first elements that fail and failure algorithms used. Damage accumulation vanishes at $r/b_0 = 1.3$ in both cases.

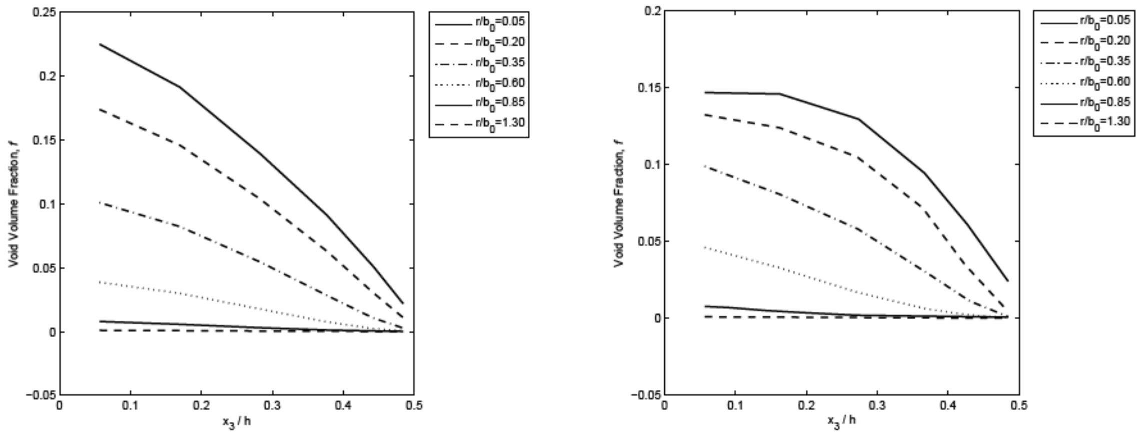

(a) (b)

Figure 3.12. Variation of void volume fraction through the thickness for (a) current results, (b) Narasimhan *et al.*'s [33] results

In Figures 3.13 and 3.14, normalized hydrostatic and normalized opening stresses (normalization is done using σ_0= 1030 MPa) are plotted versus normalized radial distance (r/b_0) ahead of the tip of notch. Results of 3-D simulations corresponding to three different planes are near the center plane, quarter plane and free surface.

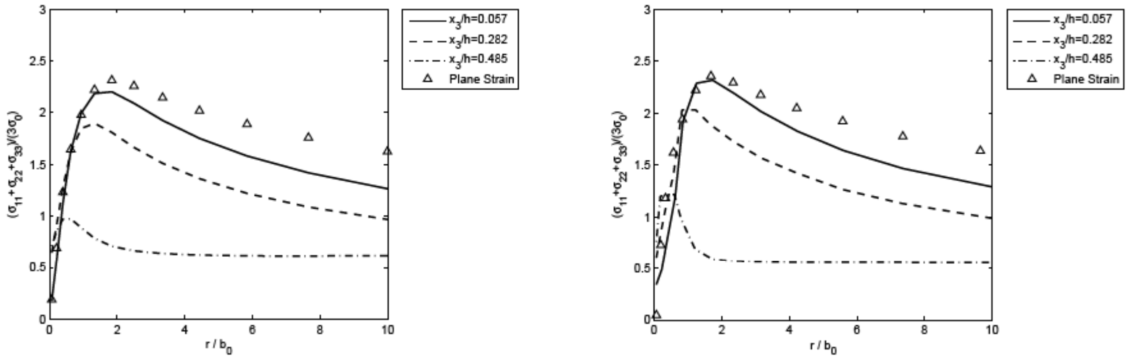

(a) (b)

Figure 3.13. Radial variation of normalized hydrostatic stress for (a) current results, (b) Narasimhan *et al.*'s [33] results

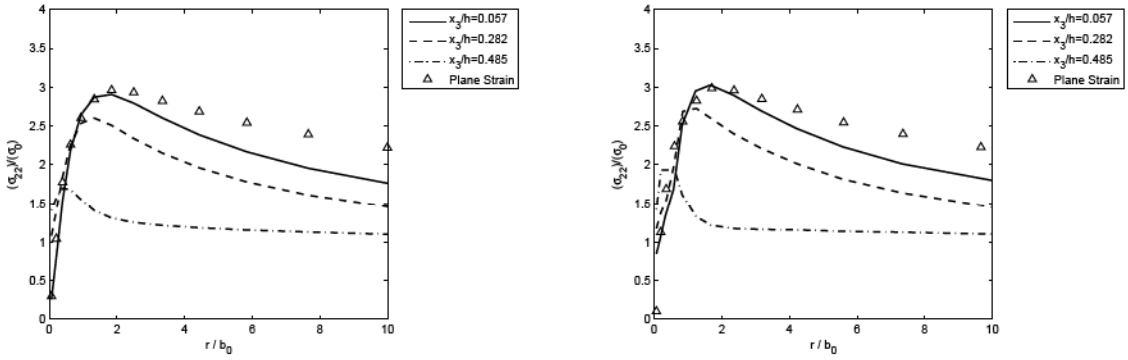

(a) (b)

Figure 3.14. Radial variation of normalized opening stress for (a) current results, (b) Narasimhan *et al.*'s [33] results

Highest hydrostatic and opening stresses are near the center-plane, and a close comparison between 3-D center and plane strain results should be noted in both current results and Narasimhan *et al.*'s results in Figures 3.13 and 3.14. It can be concluded that when Narasimhan *et al.*'s work [33] is remodeled using finite elements and built-in Gurson - Tvergaard - Needleman model, reasonable results within an acceptable agreement are obtained.

3.3. A Parametric Study on GTN Model Parameters

The effects of yield function coefficient, q_1 and void nucleation parameters, ϵ_n, s_n, f_n on nominal stress - strain response of a circumferentially waisted round tensile bar specimen are investigated, in this section. The geometry of the problem is shown in Figure 3.15. The specimen geometry is the one that is examined experimentally by Paulino *et al.* [41] to determine the stress - strain response of pure titanium.

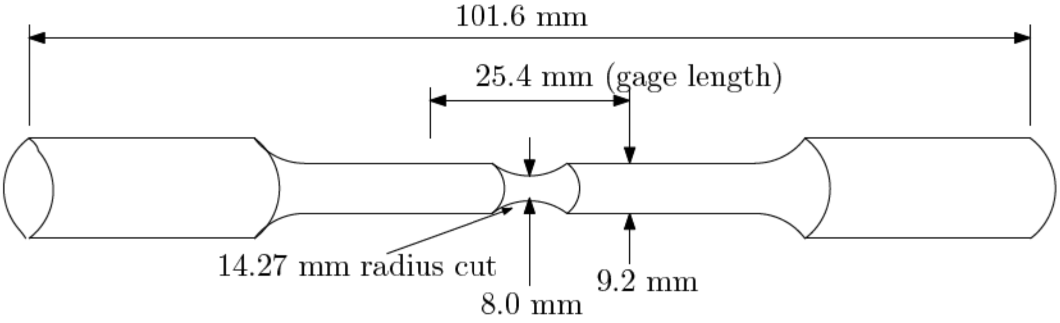

Figure 3.15. Circumferentially waisted round tensile bar specimen geometry

Gage length section of the specimen is discretized using 2-D axisymmetric finite elements. Displacement controlled loading and boundary conditions are applied for the analyses as illustrated in Figure 3.16 (a) and corresponding finite element mesh is shown in Figure 3.16 (b). 1280 linear quadrilateral elements of type CAX4R are used in FE mesh. In these simulations, Abaqus/Standard solver and power hardening plasticity are used. Young's modulus E is 107 GPa, Poisson's ratio is 0.34, initial yield stress σ_0 is 450 MPa, and power hardening exponent n is 1/10.

In the parametric studies, following original values are taken $q_1 = 1.5$, $q_2 = 1$, $q_3 = q_1^2 = 2.25$, $\epsilon_n = 0.3$, $s_n = 0.1$, and $f_n = 0.04$ which are generally used for a steel. Values of q_1, ϵ_n, s_n, and f_n are varied within -6 % and 6 % of their original values. Failure stain and maximum stress values are tabulated for different q_1, ϵ_n, s_n, and f_n values in Tables 3.2-3.5. Stress versus strain for different q_1, ϵ_n, s_n, and f_n values are plotted in Figures 3.17 - 3.20 (a). A in Equation 2.135 is also plotted in Figures 3.17 - 3.20 (b) to figure out the behavior of $\dot{f}_{nucleation}$ for different values of q_1, ϵ_n, s_n, and f_n. Note that in Figure 3.17 (b), there is only one curve because A is not a function of q_1, and ϵ_n, s_n, and f_n are all constant for varying q_1. In these figures, increasing directions of the changing parameter values are denoted with an arrow.

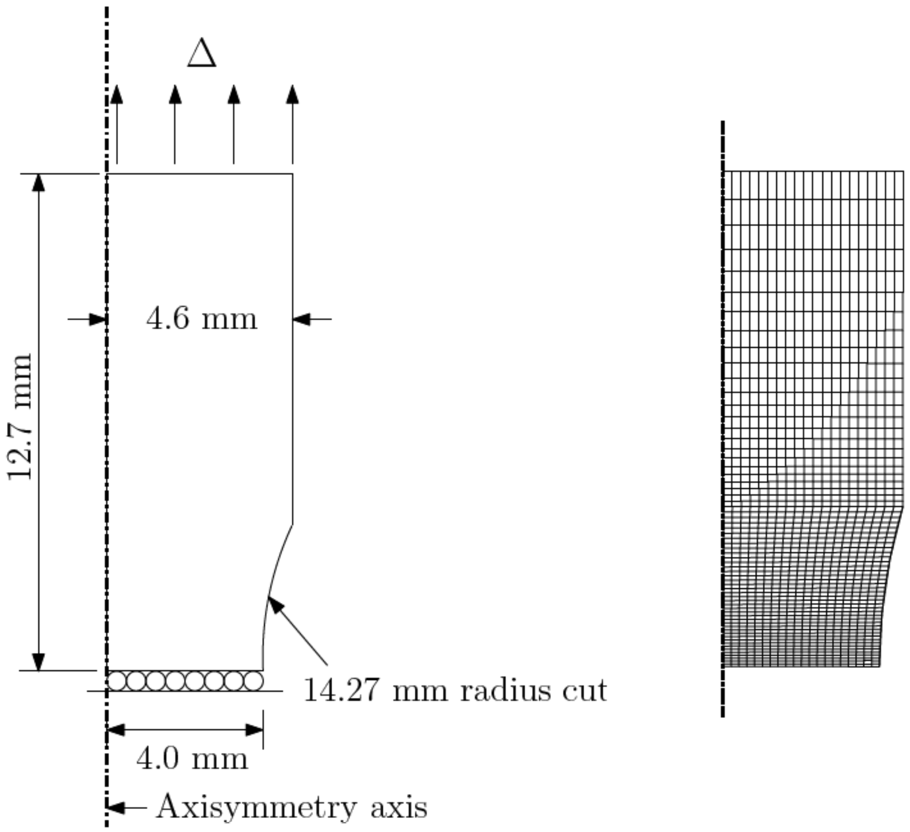

(a) (b)

Figure 3.16. Tensile bar specimen's (a) gage length section used for finite element model, (b) finite element mesh for parametric study

The failure strain of the material decreases as seen in Figure 3.17 (a) when the value of q_1 increases. The failure void volume fraction is equal to $1/q_1$ when $q_3 = q_1^2$. The void volume fraction at failure is inversely proportional to the value of q_1. Therefore, stress carrying capacity decreases earlier with the increasing q_1. In the case of void nucleation parameters, a similar trend of q_1 is observed for volume fraction of void nucleating particles f_n. When volume fraction of void nucleating particles increases failure strain of the material decreases as shown in Figure 3.20 (a). This is reasonable when increasing value of void nucleation coefficient A in Equation 2.135 with increasing value of f_n is considered. Nucleation of new voids occurs faster for higher values of f_n. An opposite behavior is observed for mean nucleation strain ϵ_n and standard deviation s_n. When ϵ_n and s_n increase, failure strain also increases. This

Table 3.2. Failure strain and maximum stress values for different values of q_1

q_1	% q_1 change	ϵ_{fail}	% ϵ_{fail} change	σ_{max}	% σ_{max} change
1.41	-6 %	0.47861	18.24 %	757.92	1.42 %
1.44	-4 %	0.45240	11.76 %	753.99	0.90 %
1.47	-2 %	0.42772	5.66 %	750.49	0.43 %
1.5	0 %	0.40479	0 %	747.30	0 %
1.53	2 %	0.38106	-5.86 %	744.38	-0.39 %
1.56	4 %	0.35914	-11.28 %	741.82	-0.73 %
1.59	6 %	0.34099	-15.76 %	739.43	-1.05 %

Table 3.3. Failure strain and maximum stress values for different values of ϵ_n

ϵ_n	% ϵ_n change	ϵ_{fail}	% ϵ_{fail} change	σ_{max}	% σ_{max} change
0.282	-6 %	0.39990	-1.21 %	745.25	-0.27 %
0.288	-4 %	0.40111	-0.91 %	745.89	-0.19 %
0.294	-2 %	0.40285	-0.48 %	750.49	-0.10 %
0.3	0 %	0.40479	0 %	747.30	0 %
0.306	2 %	0.40600	0.30 %	748.00	0.09 %
0.312	4 %	0.40750	0.67 %	748.70	0.19 %
0.318	6 %	0.40937	1.13 %	749.40	0.28 %

increase is not very significant for s_n as shown in Figure 3.19 (a). The maximum value of void nucleation coefficient A is higher for smaller values of s_n. Therefore, nucleation of new voids occurs faster for smaller values of s_n. Increase in the value of ϵ_n yields a retarded nucleation of voids and failure strain increases with increasing ϵ_n. These parametric studies show that the most sensitive parameter is q_1 and least sensitive parameter is s_n.

Table 3.4. Failure strain and maximum stress values for different values of s_n

s_n	% s_n change	ϵ_{fail}	% ϵ_{fail} change	σ_{max}	% σ_{max} change
0.094	-6 %	0.40500	0.05 %	747.27	-0.004 %
0.096	-4 %	0.40488	0.02 %	747.28	-0.003 %
0.098	-2 %	0.40485	0.01 %	747.29	-0.001 %
0.1	0 %	0.40479	0 %	747.30	0 %
0.102	2 %	0.40448	-0.08 %	747.31	0.001 %
0.104	4 %	0.40417	-0.15 %	747.32	0.003 %
0.106	6 %	0.40416	-0.16 %	747.36	0.008 %

Table 3.5. Failure strain and maximum stress values for different values of f_n

f_n	% f_n change	ϵ_{fail}	% ϵ_{fail} change	σ_{max}	% σ_{max} change
0.0376	-6 %	0.42278	4.44 %	752.22	0.66 %
0.0384	-4 %	0.41615	2.81 %	750.51	0.43 %
0.0392	-2 %	0.41050	1.41 %	748.91	0.22 %
0.04	0 %	0.40479	0 %	747.30	0 %
0.0408	2 %	0.39883	-1.47 %	745.71	-0.21 %
0.0416	4 %	0.39241	-3.06 %	744.21	-0.41 %
0.0424	6 %	0.38689	-4.42 %	742.70	-0.62 %

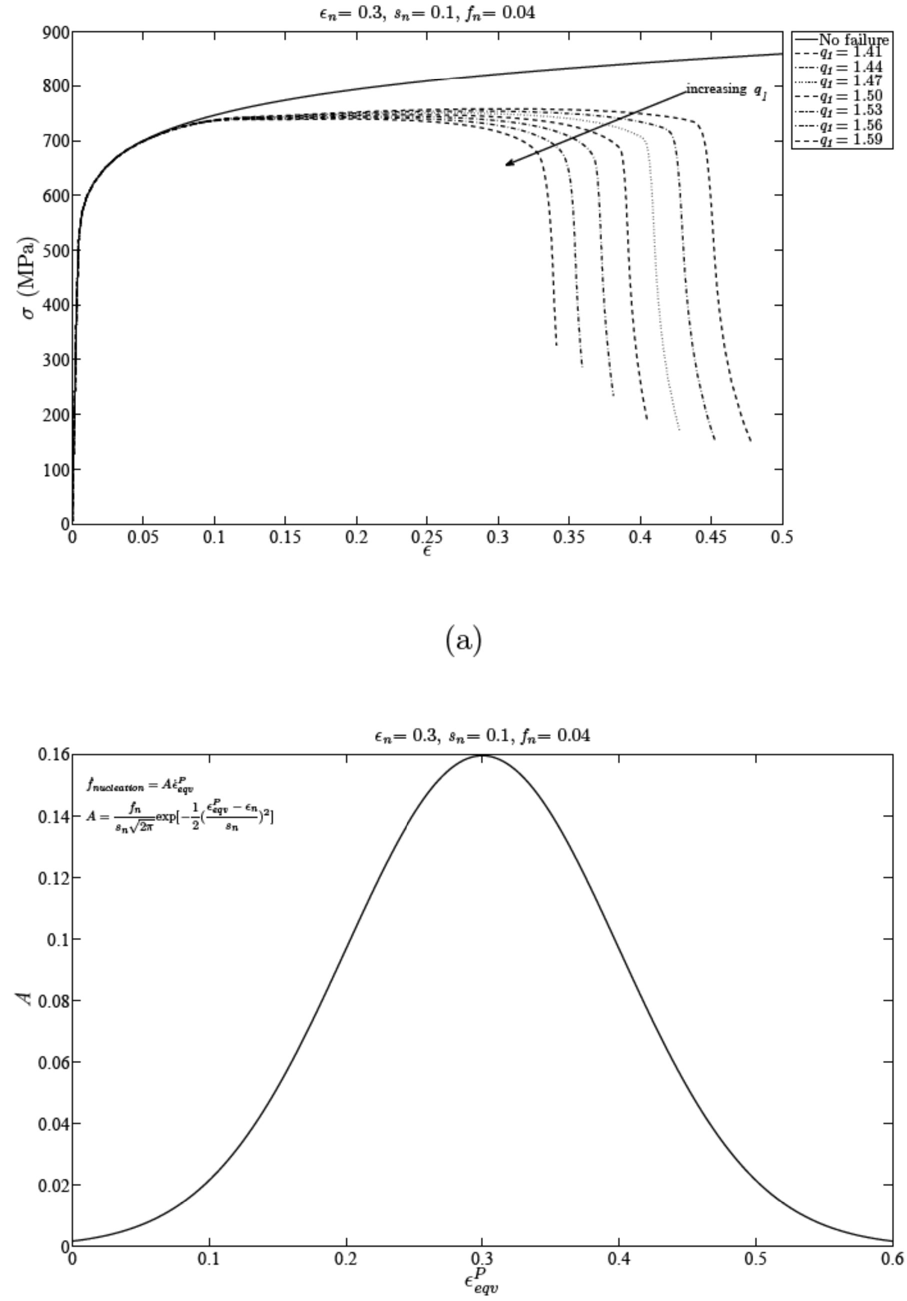

(a)

(b)

Figure 3.17. (a) Stress vs strain, and (b) variation of A w.r.t. ϵ^P_{eqv} for varying q_1

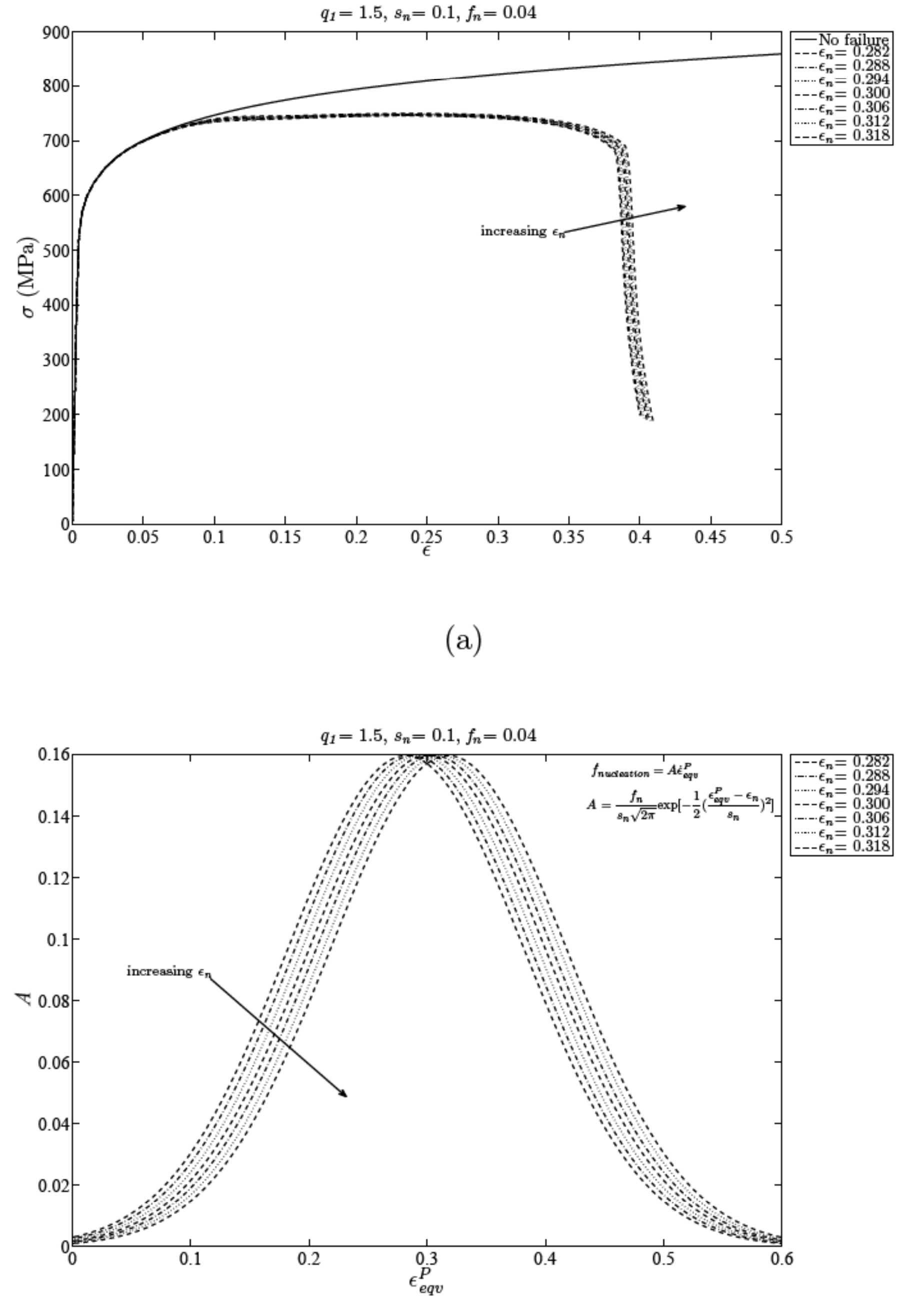

(a)

(b)

Figure 3.18. (a) Stress vs strain, and (b) variation of A w.r.t. ϵ^P_{eqv} for varying ϵ_n

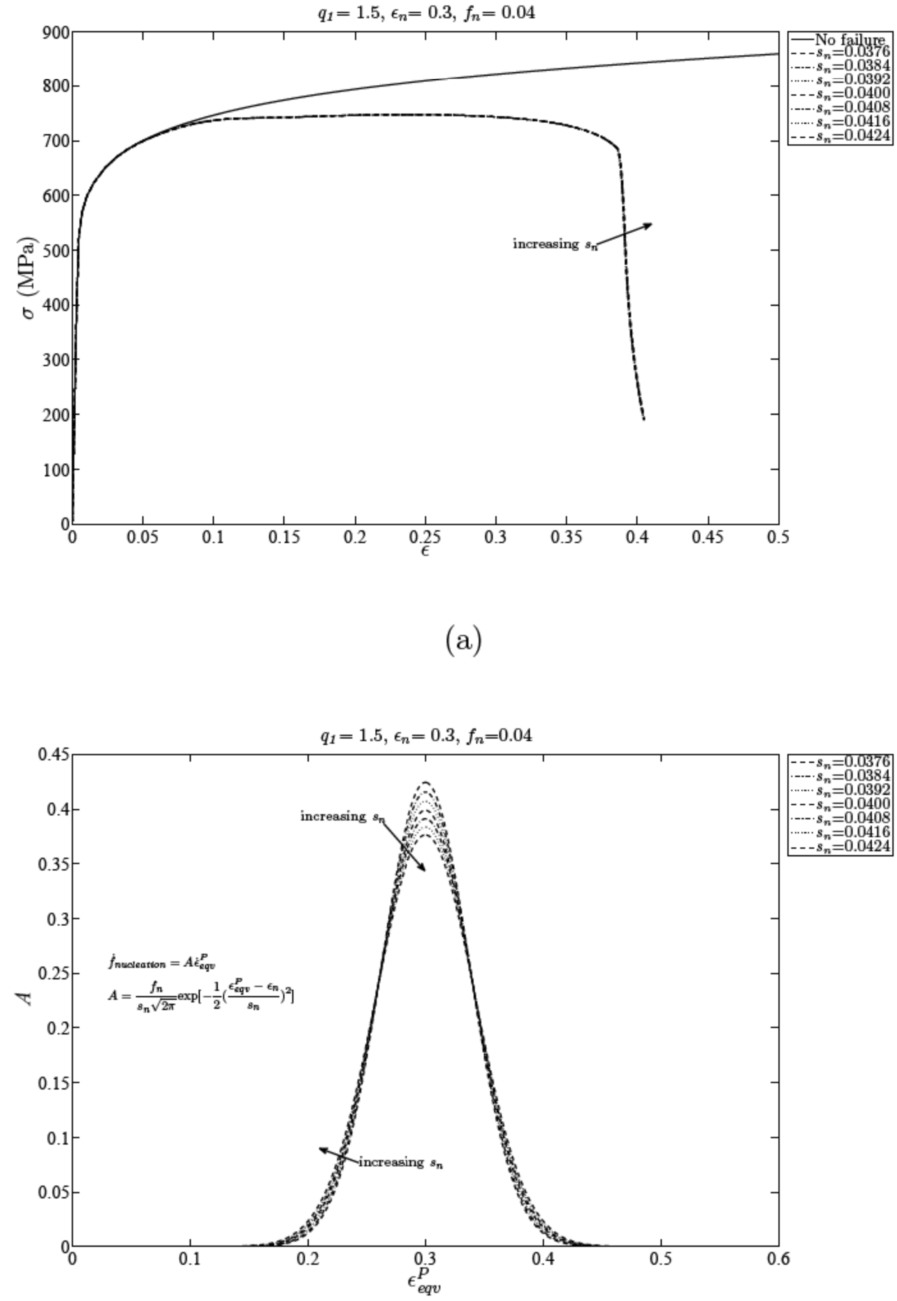

(a)

(b)

Figure 3.19. (a) Stress vs strain, and (b) variation of A w.r.t. ϵ^P_{eqv} for varying s_n

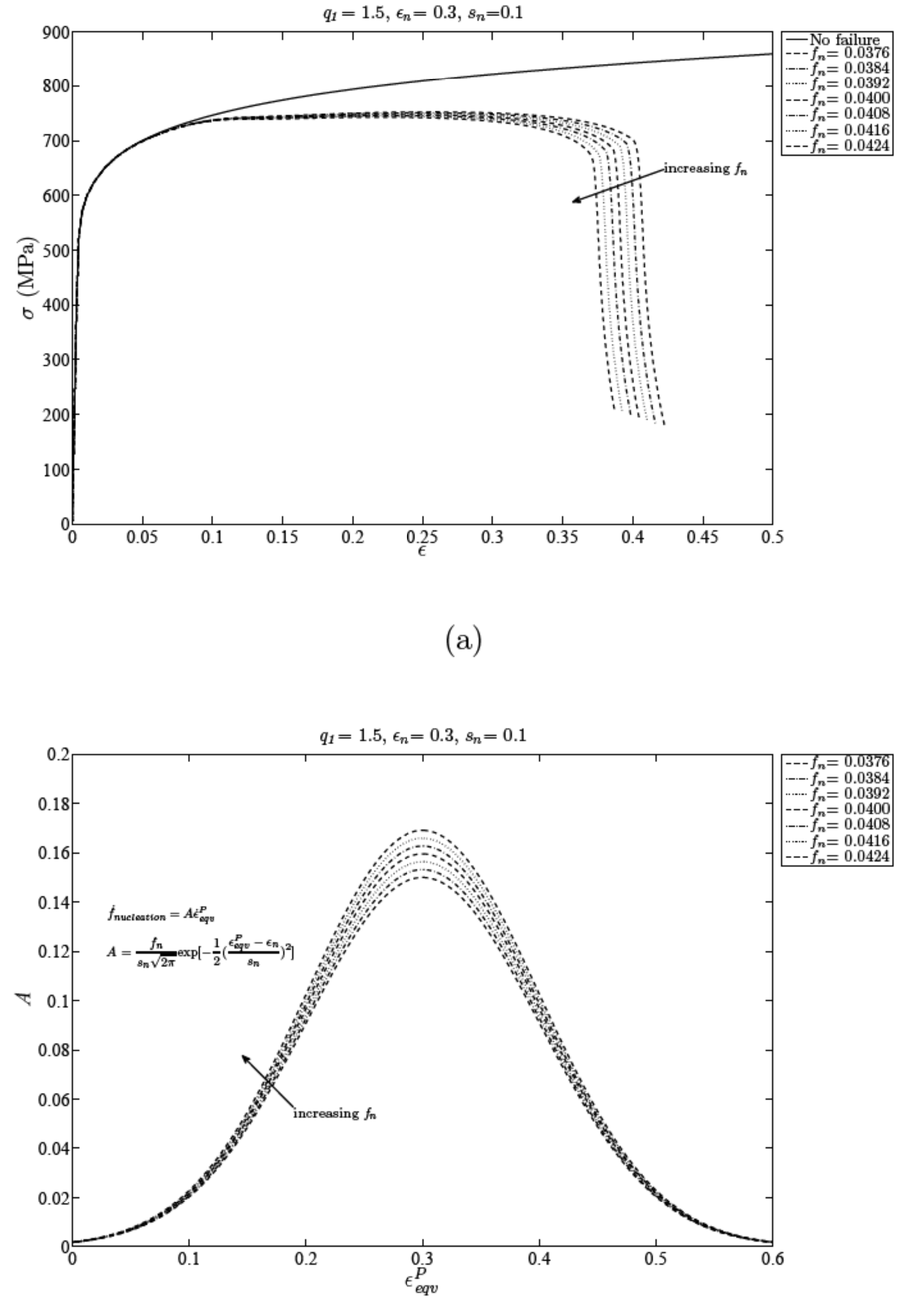

(a)

(b)

Figure 3.20. (a) Stress vs strain, and (b) variation of A w.r.t. ϵ^P_{eqv} for varying f_n

3.4. Dependence on Mesh Size

Contour plots for void volume fraction are drawn for three different 2D mesh configurations in Figure 3.21. 320, 1280 and 5120 elements are used for these different configurations, and minimum element dimensions for the meshes with 320, 1280 and 5120 elements are $25 \times 26\ \mu\mathrm{m}^2$, $12.5 \times 13\ \mu\mathrm{m}^2$ and $6.25 \times 6.5\ \mu\mathrm{m}^2$, respectively. The one with 320 elements which exhibits an expected crack growth direction is the mesh configuration used by Narasimhan *et al.* [33]. This is the case for the one with 1280 elements, but not for the one with 5120 elements. In the case with 5120 elements, model predicts a bifurcating crack. One of the common problems encountered while implementing continuum damage mechanics (CDM) models such as Gurson - Tvergaard - Needleman model to finite element simulations is mesh size dependence due to softening and strain localization. In the case of cracked structures (or structures in that a crack has been initiated), refining the mesh leads to continuously decreasing fracture energies, and misprediction of failure direction due to strain localization. The different techniques to overcome the problem of mesh dependency attempted in literature can be classified as follows [42].

(i) Placing of a limit on the size of the FEs using a concept of characteristic volume associated with defect statistics (i.e., use the mesh sizes which are of the order of mean distance between relevant inclusions in the material). This is the method used in simulations involving local damage models where the restriction on the use of mesh size near the crack tip is equivalent to indirect introduction of length scale in the constitutive equation [34, 35].
(ii) Introduction of higher-order strain gradients in the material constitutive equation or the yield function [43].
(iii) Use of a nonlocal definition of material damage parameter while preserving a local definition for strain [44].

The mesh sensitivity of ductile damage algorithms can be reduced by applying averaging techniques as mentioned in second and third items above. In such approaches an additional material parameter is introduced in the form of a characteristic length $2L$.

Physically this internal length scale of the material may be interpreted as the size of a process zone or as a function of the distance between individual voids or the distance between dimples in the fracture surfaces, but is not fully understood at present [45].

The GTN model to only a single row of elements where failure is expected that is a common technique sometimes called the “computational cells” method as proposed by Xia and Shih [34, 35]. In this dissertation, mesh size is considered as a material parameter and “computational cells” method is used.

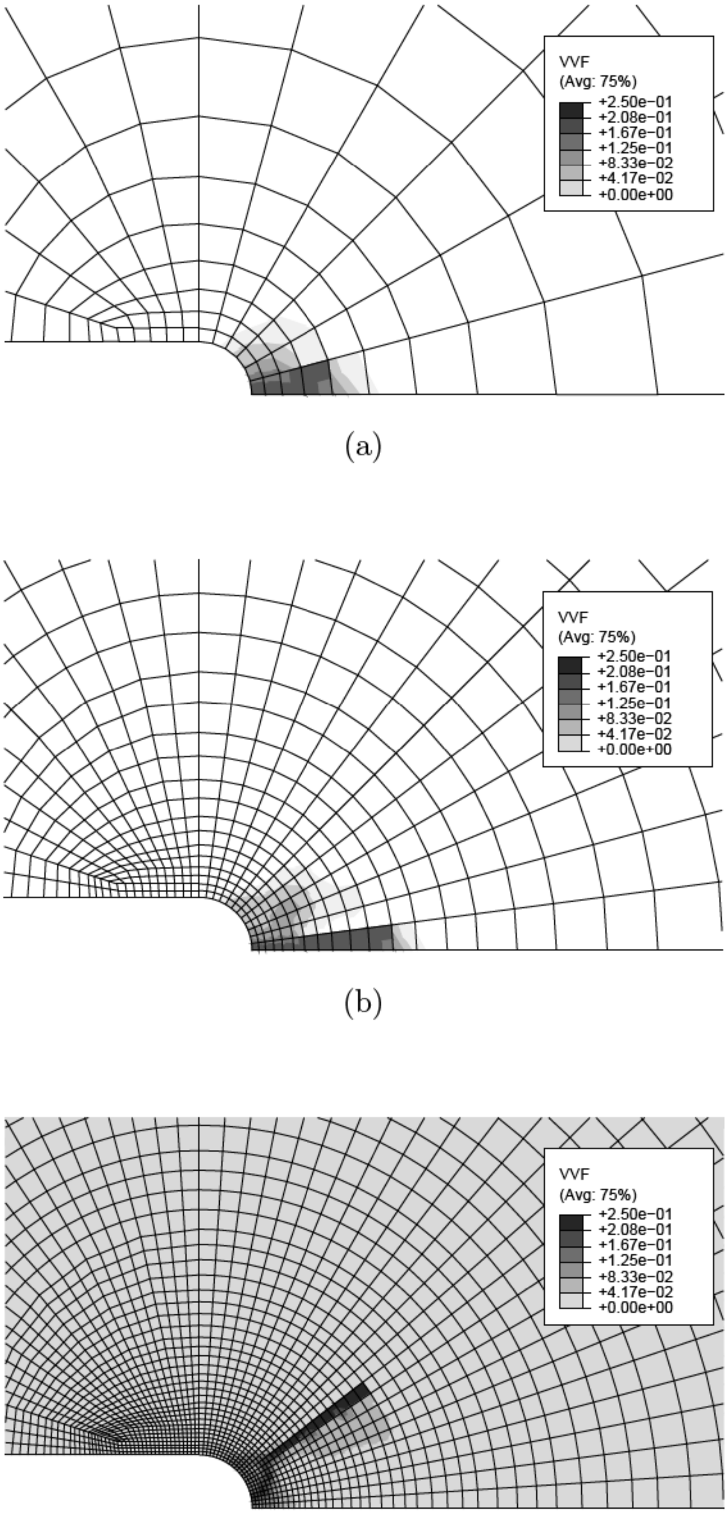

(a)

(b)

(c)

Figure 3.21. Contour plots of void volume fraction for different mesh sizes; (a) 320 elements, (b) 1280 elements, and (c) 5120 elements

4. FAILURE ANALYSIS OF FGM SPECIMENS USING GURSON - TVERGAARD - NEEDLEMAN MODEL

In this chapter two example problems taken from literature are studied. One of them is on failure of a pure titanium (Ti) and a titanium monoboride / titanium (TiB / Ti) functionally graded material (FGM) single edge notched bending specimen studied by Paulino *et al.* [41] and Jin *et al.* [17, 18], respectively. The other example problem is on failure of homogeneously and gradually ultraviolet irradiated polyethylene carbon monoxide co-polymer (a polymer based laboratory scale FGM) uniaxial and single edge notched tension specimen studied by Abanto-Beuno [23], Abanto-Bueno and Lambros [47] and Kandula *et al.* [22].

GTN model is applied to these two problems to study failure. First homogeneous material's GTN model parameters are determined; then, failure of FGM specimens is simulated using finite elements with GTN model.

4.1. Failure of Pure Ti and TiB / Ti FGM Specimens

Paulino *et al.* [41] used tensile test results to determine plasticity data for pure titanium (Ti), and conducted crack growth experiments using single edge notched bending specimens to determine crack initiation conditions; load versus load line displacement and load versus crack mouth opening displacement (CMOD).

For the present work, GTN model parameters are predicted using tensile test data given by Paulino *et al.* [41] and crack initiation of single edge notched bending specimen is simulated using finite elements.

Crack growth in ceramic / metal functionally graded material (FGM) namely titanium monoboride / titanium (TiB / Ti) FGM is investigated by Jin *et al.* considering elastic behavior [17], and considering elasto-plastic behavior [18]. Plasticity is required while using GTN model in finite element analyses. A volume fraction based, elastic-plastic model (extension of the original Tamura-Tomota-Ozawa model [48]) that is explained in section 4.1.2.1 describes the elastic-plastic response of the bulk material. Jin *et al.* use cohesive zone model and a computational scheme to analyze crack growth in a single edge notched bending specimen made of a TiB / Ti FGM and to obtain crack initiation condition; load versus crack mouth opening displacement (CMOD) numerically. In section 4.1.2.2, failure of the same specimen is studied using GTN model and it's application is discussed.

4.1.1. Failure of Pure Ti Specimens

Failure of pure Ti uniaxial tension specimen is simulated using GTN model, and corresponding GTN model parameter are determined using experimental data given by Paulino *et al.* [41]. Load versus crack mouth opening displacement (CMOD) and load versus load line displacement of single edge notched bending specimen are calculated using GTN model parameters that are obtained from uniaxial tension specimen. The results are compared with the experimental data given by Paulino *et al.* [41].

4.1.1.1. Failure of Pure Ti Uniaxial Tension Specimen. GTN model parameters are obtained from uniaxial tensile specimen for which the geometry is given in Figure 3.15, and the model in Figure 3.16. Abaqus / Standard is used for FE analyses. Material properties for pure Ti are: $E = 107$ GPa, $\nu = 0.34$ and initial yield stress $\sigma_0 = 450$ MPa. Power hardening is assumed as follows:

$$\frac{\epsilon}{\epsilon_0} = \left(\frac{\sigma}{\sigma_0}\right)^{1/n} ; \qquad \sigma \geq \sigma_0 \tag{4.1}$$

where n is the hardening exponent. Failure parameters are predicted in a way that results in an acceptable fit to experimental stress - strain response by trial and error using different power hardening exponents that are 1/10, 1/11 and 1/12. A reasonable agreement with experimental data is achieved when $q_1 = 2.5$, $q_2 = 1$, $q_3 = q_1^2 = 6.25$, $s_n = 0.1$ and $f_n = 0.04$ are used. ϵ_n is 0.2 when power hardening exponent is 1/10, it is 0.23 when power hardening exponent is 1/11 and finally ϵ_n is 0.25 when power hardening exponent is 1/12. Resulting stress - strain plots are given with experimental ones in Figure 4.1. The curve with $1/n = 10$ looks like the best fit to experimental results. Therefore, material and failure properties are used for $1/n = 10$ fit that yields $E = 107$ GPa, $\nu = 0.34$, $\sigma_0 = 450$ MPa, $q_1 = 2.5$, $q_2 = 1$, $q_3 = q_1^2 = 6.25$, $\epsilon_n = 0.2$, $s_n = 0.1$ and $f_n = 0.04$.

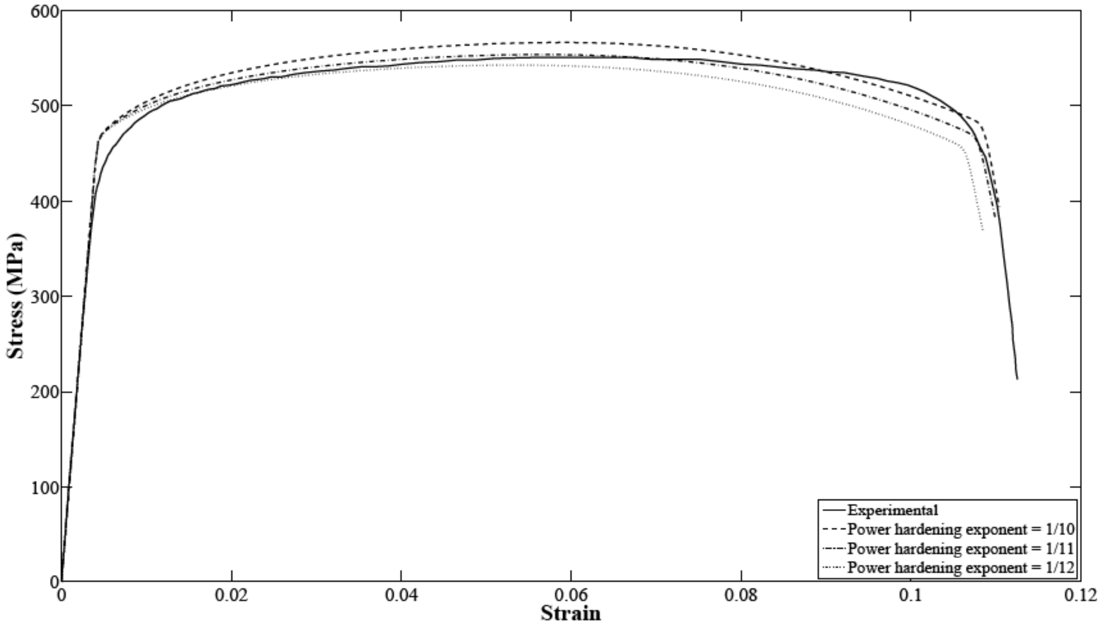

Figure 4.1. Experimental [41] and GTN model stress - strain responses of pure Ti uniaxial tension specimen

4.1.1.2. Failure of Pure Ti Single Edge Notched Bending Specimen. Figure 4.2 shows the geometry of single edge notched bending (SENB) specimen modeled in this section. A quarter of entire pure Ti SENB specimen is discretized using 7 different 3-D mesh configurations for which the properties and results are tabulated in Table 4.1. Meshes for Model #1, #3, #5 and #7 are shown in Figures 4.3 (a-d), respectively. The difference between these models is the mesh size ahead of the crack-tip. Mesh refinement is conducted in length - width plane, there is no refinement along the thickness. The most refined model is Model #7.

Load vs CMOD and load vs load line displacement are plotted in Figures 4.4 and 4.5, respectively. In these plots, squares represent experimental data given by Paulino *et al.* [41], solid line and dashed line with circles are results of Model #3 and #7, respectively. A good agreement between results of experimental load vs CMOD, and load vs load line displacement and the results of Model #3 is obtained. Note that, GTN model results are calculated using Abaqus / Standard solver, and progressive failure cannot be simulated using Abaqus / Standard. Therefore, the present results are obtained up to failure of the first element near the crack-tip. Experimentally calculated failure load is 11.5 kN, and numerically predicted failure load from Model #3 is 12.3 kN. Mesh sensitivity that is discussed in section 3.4, is observed in results. Failure load and maximum load line displacement decreases when the element size near the crack-tip decreases.

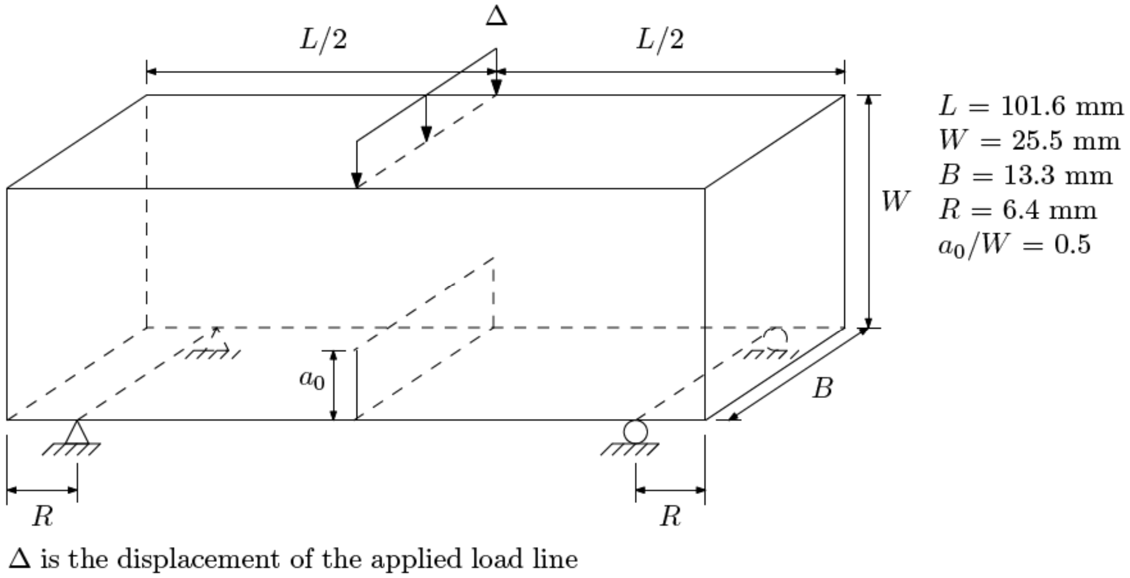

Figure 4.2. Pure Ti SENB specimen dimensions for three-point bend testing (Note that the figure is not scaled)

4.1.2. Failure of TiB / Ti FGM Specimen

In the following subsections, an elastic-plastic model to be used for FGMs proposed by Jin *et al.* [18] is discussed in detail. Then, the model's numerical implementation in Abaqus is explained. The results of the GTN model for TiB / Ti FGM single edge notched bending specimen are compared to cohesive zone model results obtained by Jin *et al.* [18].

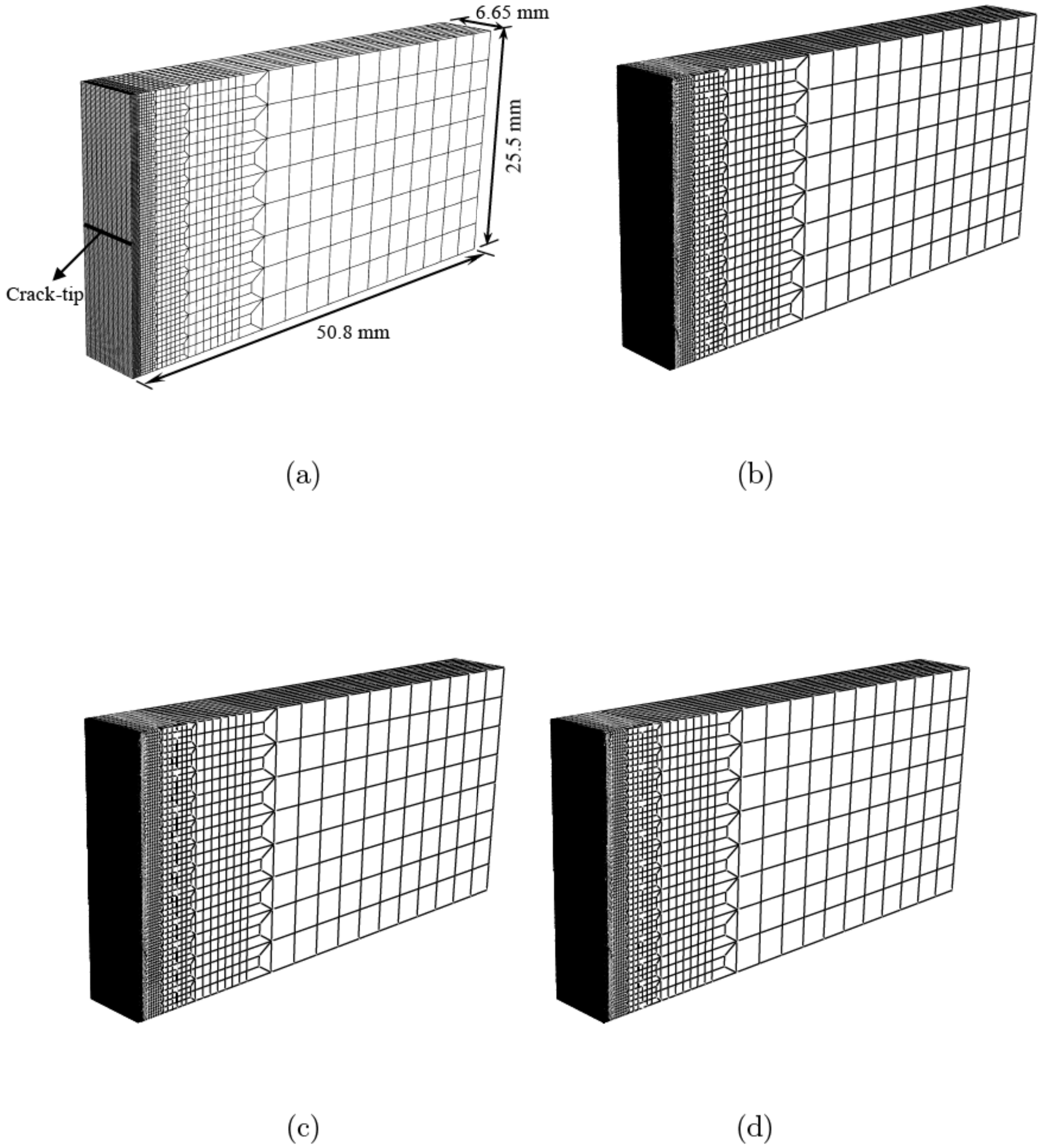

Figure 4.3. Pure Ti SENB specimen finite element meshes used for (a) Model #1, (b) Model #3, (c) Model #5 and (d) Model #7

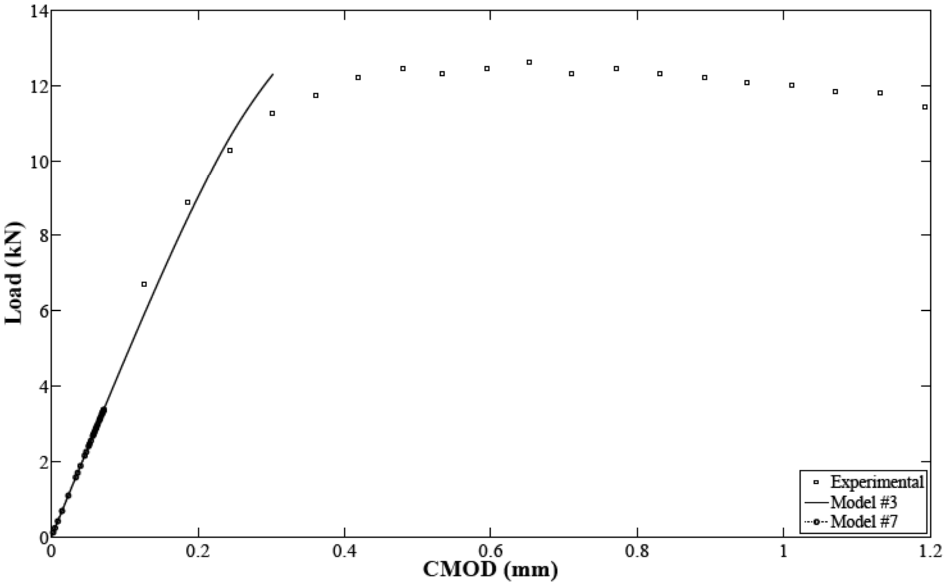

Figure 4.4. Experimental [41] and GTN model load versus crack mouth opening displacement results for pure Ti SENB specimen.

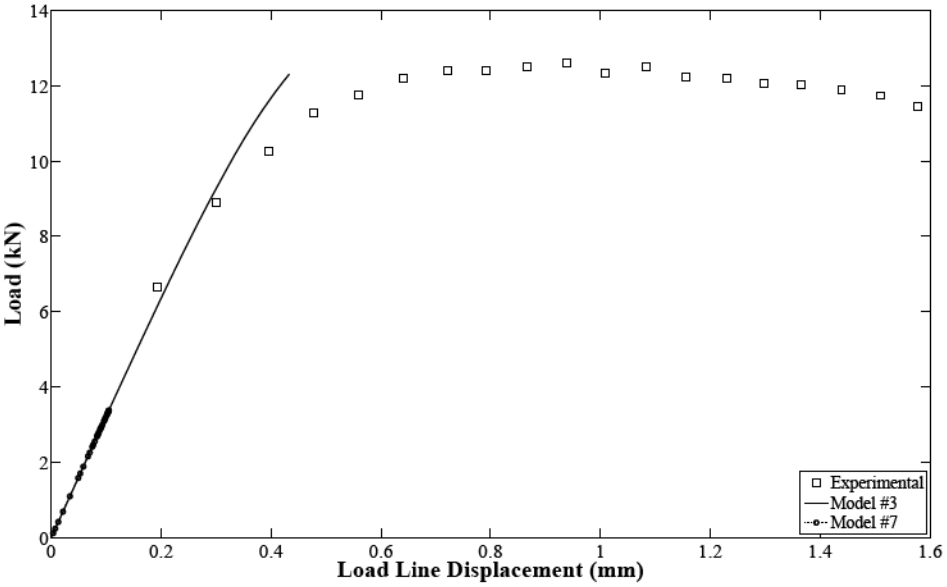

Figure 4.5. Experimental [41] and GTN model load versus load line displacement results for pure Ti SENB specimen

Table 4.1. FE model properties and results for pure Ti SENB specimen

FE Model #	Number of Elements	Size of Min. Element (mm)	Max. Load Line Displacement (mm)	Initial Failure Load (kN)
1	24722	0.1328 × 0.1328 × 0.665	0.960	16.3
2	40082	0.0664 × 0.0664 × 0.665	0.637	14.9
3	70802	0.0332 × 0.0340 × 0.665	0.437	12.3
4	86240	0.0166 × 0.0166 × 0.665	0.310	9.4
5	114480	0.0083 × 0.0083 × 0.665	0.218	6.8
6	119680	0.00415 × 0.00415 × 0.665	0.150	4.8
7	124880	0.002075 × 0.002075 × 0.665	0.106	3.4

4.1.2.1. Elastic-Plastic Model for FGMs. One of the issues in modeling of FGMs is to decide how to implement plasticity required for GTN model. Jin *et al.* [18] proposed a volume fraction based, elastic-plastic model for FGMs which is an extended form of the original Tamura - Tomota - Ozawa model obtained by Tamura *et al.* [48]. This model without the failure is implemented to Abaqus, and the results of FE and the theory are compared. Plastic part of the new proposed model is not linear. The set of parametric equations to determine the stress - strain curve for the FGM are as follows:

$$\frac{\epsilon}{\epsilon_{0_{FGM}}} = \frac{V_{cer}E_{FGM}}{q+E_{cer}}\frac{\sigma_{met}}{\sigma_{0_{FGM}}} + \frac{(q+V_{met}E_{cer})E_{FGM}}{(q+E_{cer})E_{met}}\frac{\sigma_{0_{met}}}{\sigma_{0_{FGM}}}\left(\frac{\sigma_{met}}{\sigma_{0_{met}}}\right)^{1/n_{met}}, \quad (4.2)$$

$$\frac{\sigma}{\sigma_{0_{FGM}}} = \frac{V_{met}q+E_{cer}}{q+E_{cer}}\frac{\sigma_{met}}{\sigma_{0_{FGM}}} + \frac{V_{cer}qE_{cer}}{(q+E_{cer})E_{met}}\frac{\sigma_{0_{met}}}{\sigma_{0_{FGM}}}\left(\frac{\sigma_{met}}{\sigma_{0_{met}}}\right)^{1/n_{met}} \quad (4.3)$$

where V_{met}, V_{cer}, E_{met} and E_{cer} are volume fraction and Young's moduli of metal and ceramic constituent phases, respectively. $\epsilon_{0_{FGM}} = \sigma_{0_{FGM}} \;/\; E_{FGM}$ where

$$E_{FGM} = \left(V_{met}E_{met}\frac{q+E_{cer}}{q+E_{met}} + V_{cer}E_{cer}\right)\bigg/\left(V_{met}\frac{q+E_{cer}}{q+E_{met}} + V_{cer}\right), \quad (4.4)$$

and

$$\sigma_{0_{FGM}} = \sigma_{0_{met}}\left(V_{met} + \frac{(q+E_{met})E_{cer}}{(q+E_{cer})E_{met}}V_{cer}\right). \quad (4.5)$$

$\sigma_{0_{met}}$, $\epsilon_{0_{met}}$ denote the initial yield stress and strain of the metal, respectively. q is the ratio of stress to strain transfer which is formulated as $q = \dfrac{\sigma_{cer} - \sigma_{met}}{|\epsilon_{cer} - \epsilon_{met}|}$. n_{met} is the hardening exponent of the metal. Poisson's ratio is calculated using rule of mixtures $\nu = V_{met}\, \nu_{met} + V_{cer}\, \nu_{cer}$.

Material properties of ingredients of TiB / Ti FGM are tabulated in Table 4.2. Using them, stress - strain curves using the extended TTO model (Equations 4.2 - 4.3) for different volume fractions of Ti are plotted in Figure 4.6 where $q = 4.5$ GPa.

Table 4.2. Material properties of pure TiB and Ti [18]

Material Name	Young's Modulus (GPa)	Poisson's Ratio	Initial Yield Stress (MPa)	Hardening Exponent
TiB	375	0.14	N/A	N/A
Ti	107	0.34	450	1/10

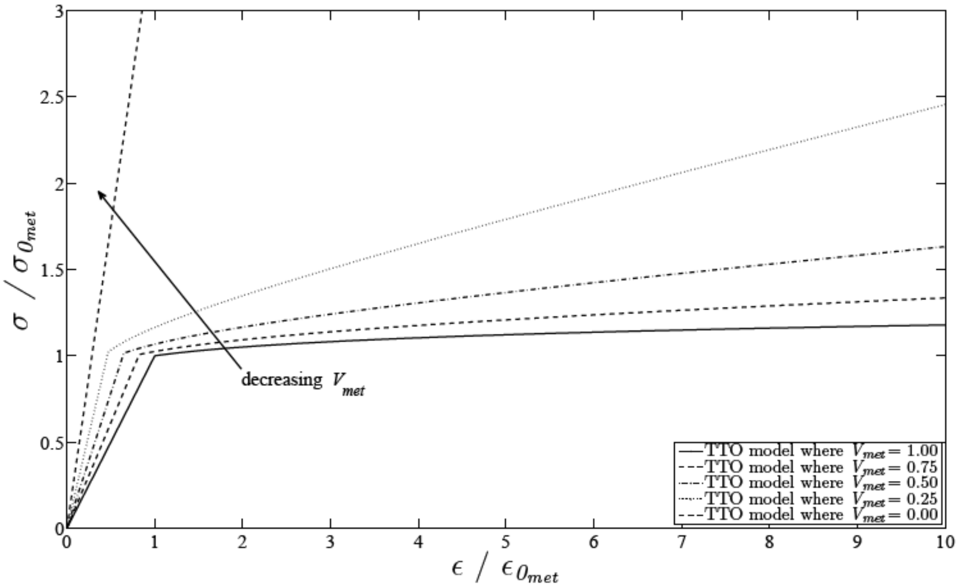

Figure 4.6. Normalized stress - strain curves for different volume fractions of constituent phases, extended TTO model is used

A TiB / Ti FGM plate that is shown in Figure 4.7 is studied using Abaqus to examine whether stress - strain responses calculated by extended TTO model and obtained numerically from Abaqus agree or not. Material variation along x direction is considered. Uniform displacement is applied where Δ_{max} is 60 mm.

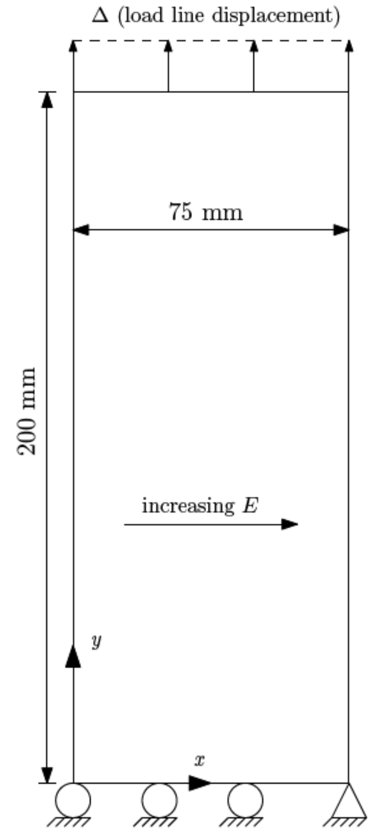

Figure 4.7. Geometry and boundary conditions of the TiB / Ti FGM plate

Volume fraction variation of Ti is $V_{met}(x) = 1$ - 0.01 x, and corresponding Young's modulus E variation calculated from Equation 4.4 is plotted in Figure 4.8. At the left edge where $x = 0$ mm, material is pure Ti. On the other hand, at the right edge where $x = 75$ mm, volume fraction of the metal is 0.25 which means that right edge is not pure TiB. Stress - strain curves obtained from Abaqus for different V_{met} are plotted in Figure 4.9 with results calculated from extended TTO model and a good agreement is achieved between them.

4.1.2.2. Failure of TiB / Ti FGM Single Edge Notched Bending Specimen. Elastic - plastic model introduced in section 4.1.2.1 is used to define the plastic responses of different volume fraction mixtures of TiB and Ti because they are not available experimentally. The geometry of single edge notched bending (SENB) specimen tested by Jin *et al.* [17, 18] is shown in Figure 4.10. Volume fraction variation of TiB and Ti

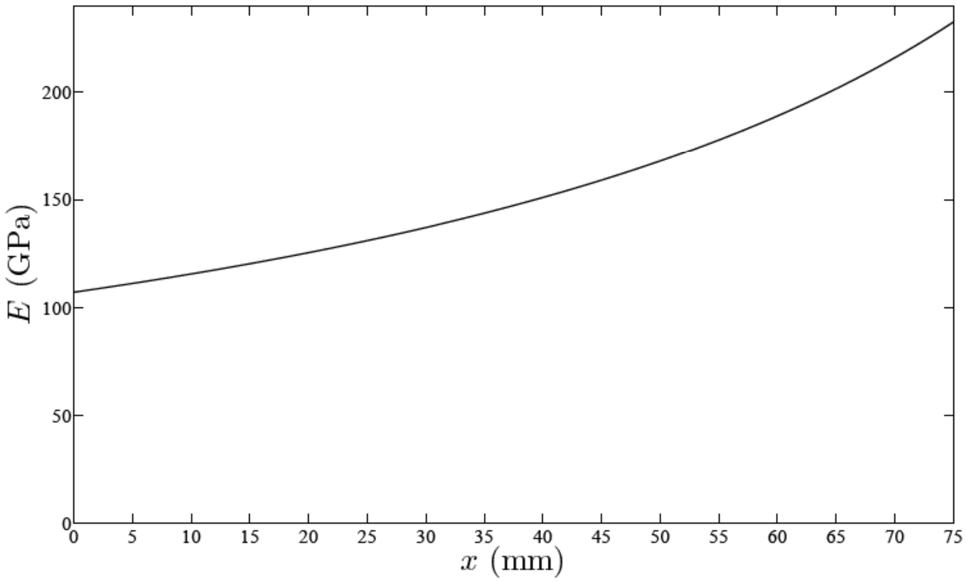

Figure 4.8. Young's modulus variation along width of the TiB / Ti FGM plate

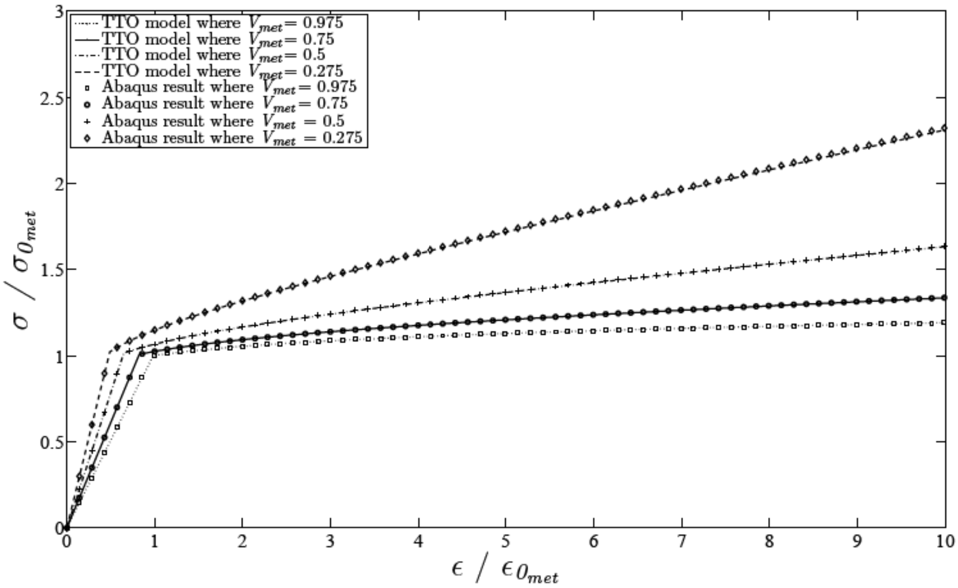

Figure 4.9. Stress - strain responses of the TiB / Ti FGM plate's sections which possess different volume fractions of Ti

along the width of the specimen is tabulated in Table 4.3 and is plotted in Figure 4.11. A third order polynomial is fitted to the volume fraction variation of Ti as it varies between % 15 and % 100 from bottom to top edge. Crack grows from more brittle region to more ductile region.

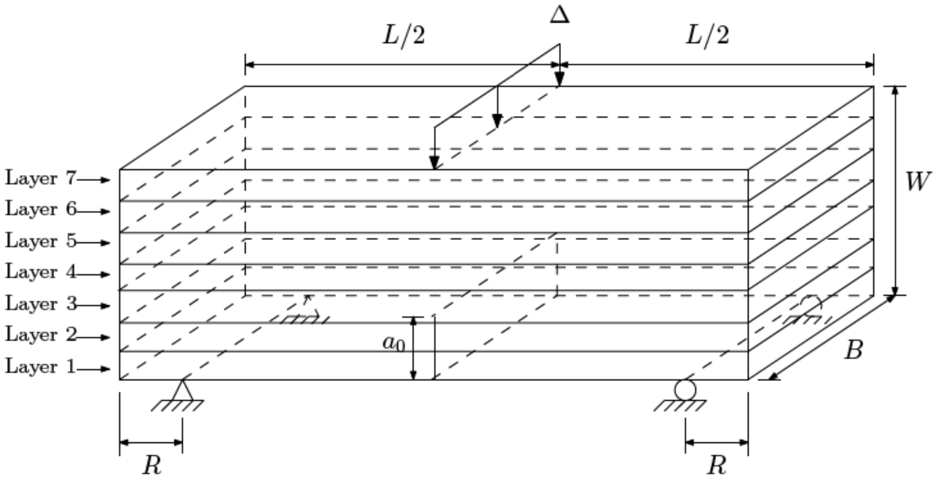

$L = 79.4$ mm
$W = 14.7$ mm
$B = 7.4$ mm
$R = 10.2$ mm
$a_0/W = 0.3$

Δ is the displacement of the applied load line

Figure 4.10. TiB / Ti FGM single edge-notched bending specimen dimensions for three-point bend testing (Note that the figure is not scaled)

Table 4.3. Volume fraction and thickness distribution in the layered TiB / Ti FGM SENB specimen [18]

Layer #	Thickness (mm)	TiB vol. fraction	Ti vol. fraction
1	2.515	0.85	0.15
2	1.676	0.79	0.21
3	1.778	0.62	0.38
4	1.448	0.47	0.53
5	1.753	0.32	0.68
6	2.134	0.15	0.85
7	3.429	0.00	1.00

Plastic part is defined by using the extended TTO model using material properties given in Table 4.2. A reasonable failure strain variation is obtained by varying q_1 values

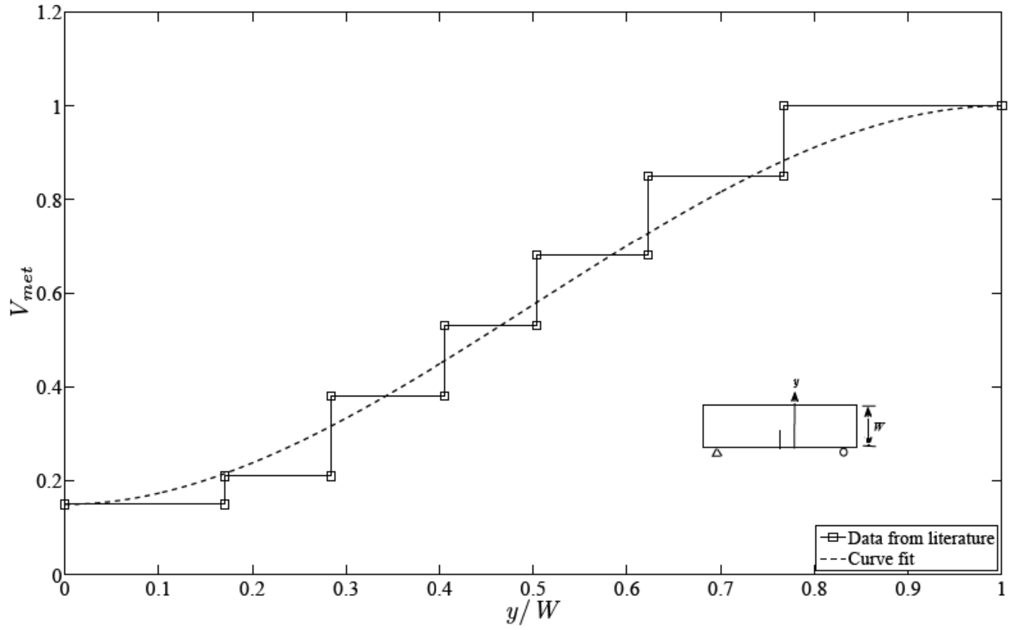

Figure 4.11. Volume fractions of Ti in the TiB / Ti SENB specimen [49] (Fitted curve is a third order polynomial)

(with $q_2 = 1$, $q_3 = q_1^2$) for different volume fractions of Ti as shown in Figure 4.12. When the volume fraction of Ti decreases, an increase in the value of q_1 which would yield a lesser failure strain is proposed. This behavior is suitable for a more brittle material. Void nucleation parameters, ϵ_n, s_n, f_n are kept constant at values 0.2, 0.1, 0.04, respectively. These set of parameters yield an assumed reasonable stress - strain responses that is plotted in Figure 4.13. They are obtained from homogeneous tensile specimens finite element analyses for different volume fractions of Ti.

A quarter of entire TiB / Ti FGM SENB specimen is discretized using 7 different 3-D mesh configurations and model properties are tabulated in Table 4.4 which is also done for pure Ti SENB specimen's finite element modeling. Meshes for Model #1, #2, #4 and #7 are plotted in Figures 4.14 (a-d), respectively. Reduction in failure load is observed with a refinement in mesh. Failure initiation load for Model # 4 in this study is 0.994 kN that approximately matches 0.925 kN measured experimentally by Carpenter *et al.* [49]. Load versus crack mouth opening displacement (CMOD) response of this specimen is obtained using cohesive zone model by Jin *et al.* [18]. Load versus CMOD plots obtained using GTN model are given together with cohesive zone model results

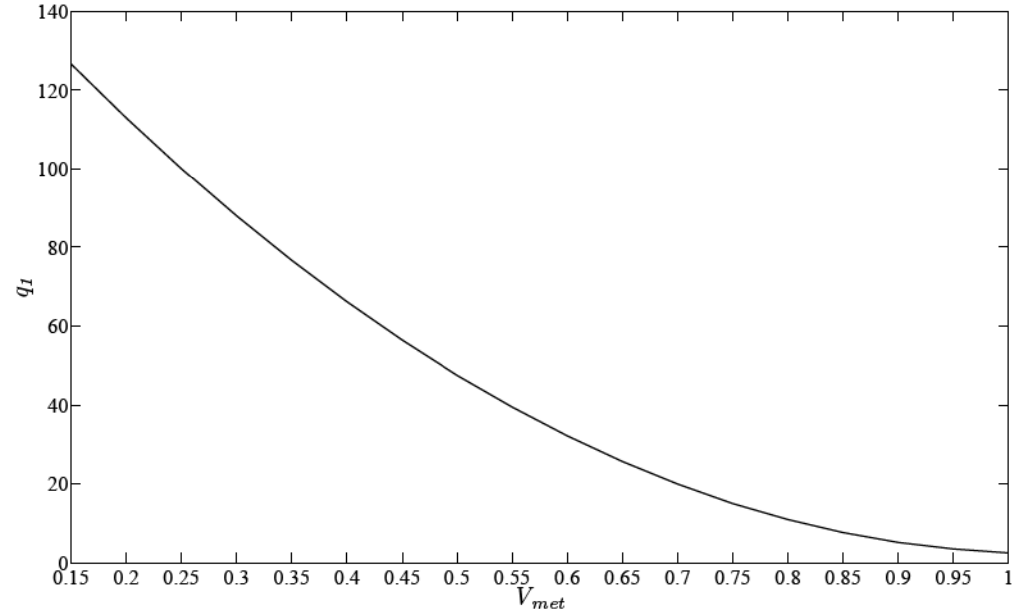

Figure 4.12. q_1 variation with respect to Ti volume fraction, TiB / Ti SENB specimen

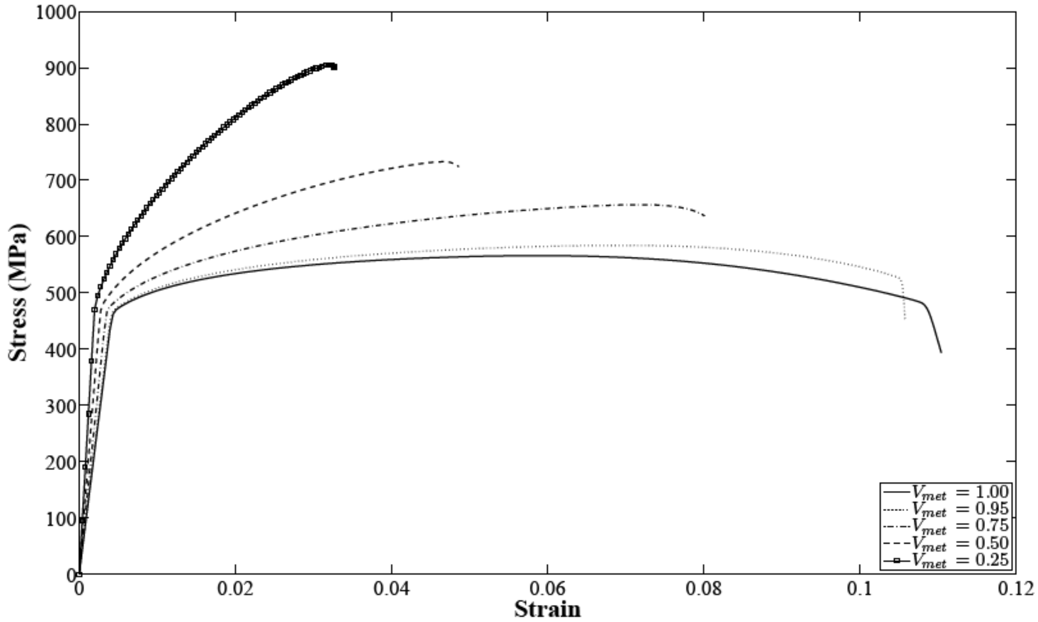

Figure 4.13. Stress - strain responses of homogeneous tensile specimens for different volume fractions of Ti

[18] in Figure 4.15. Failure loads match, but corresponding CMODs are quite different. This result can be improved by changing the used failure parameters, but it is hard to predict the parameters without tensile stress-strain response of the regions where volume fraction of Ti is less than 100%. Unfortunately, these results are not published in literature, therefore further study of Ti-TiB FGMs is omitted.

Table 4.4. FE model properties and results for TiB / Ti FGM SENB specimen

FE Model #	Number of Elements	Size of Min. Element (mm)	Initial Failure Load (kN)
1	26402	$0.1019 \times 0.1021 \times 0.37$	2.976
2	37922	$0.0510 \times 0.0510 \times 0.37$	2.062
3	60960	$0.0255 \times 0.0255 \times 0.37$	1.468
4	65520	$0.01276 \times 0.01276 \times 0.37$	0.994
5	73280	$0.00638 \times 0.00638 \times 0.37$	0.714
6	77840	$0.00319 \times 0.00319 \times 0.37$	0.502
7	80480	$0.00159 \times 0.00159 \times 0.37$	0.361

4.2. Failure of Homogeneously and Gradually Ultraviolet Irradiated Polyethylene Carbon Monoxide Co-polymer Specimens

In this section, the Gurson - Tvergaard - Needleman (GTN) model that is commonly used for metallic materials is applied to the failure of a polymeric material specifically a polyethylene carbon monoxide (ECO) co-polymer which is an enhanced photodegradable material. A novel technique is developed for the fabrication of laboratory scaled functionally graded materials (FGMs) by Lambros *et al.* [46]. Abanto-Beuno [23] and Abanto-Bueno and Lambros [47] produced laboratory scaled ECO FGM single edge notched tension (SENT) specimens. First, GTN model parameters for homogeneously ultraviolet irradiated ECO are determined. Then, load and crack extension versus load line displacement behaviors of FGM specimens are calculated using GTN model. In the following finite element analyses, to simulate progressive failure of multiple elements, Abaqus/Explicit is used.

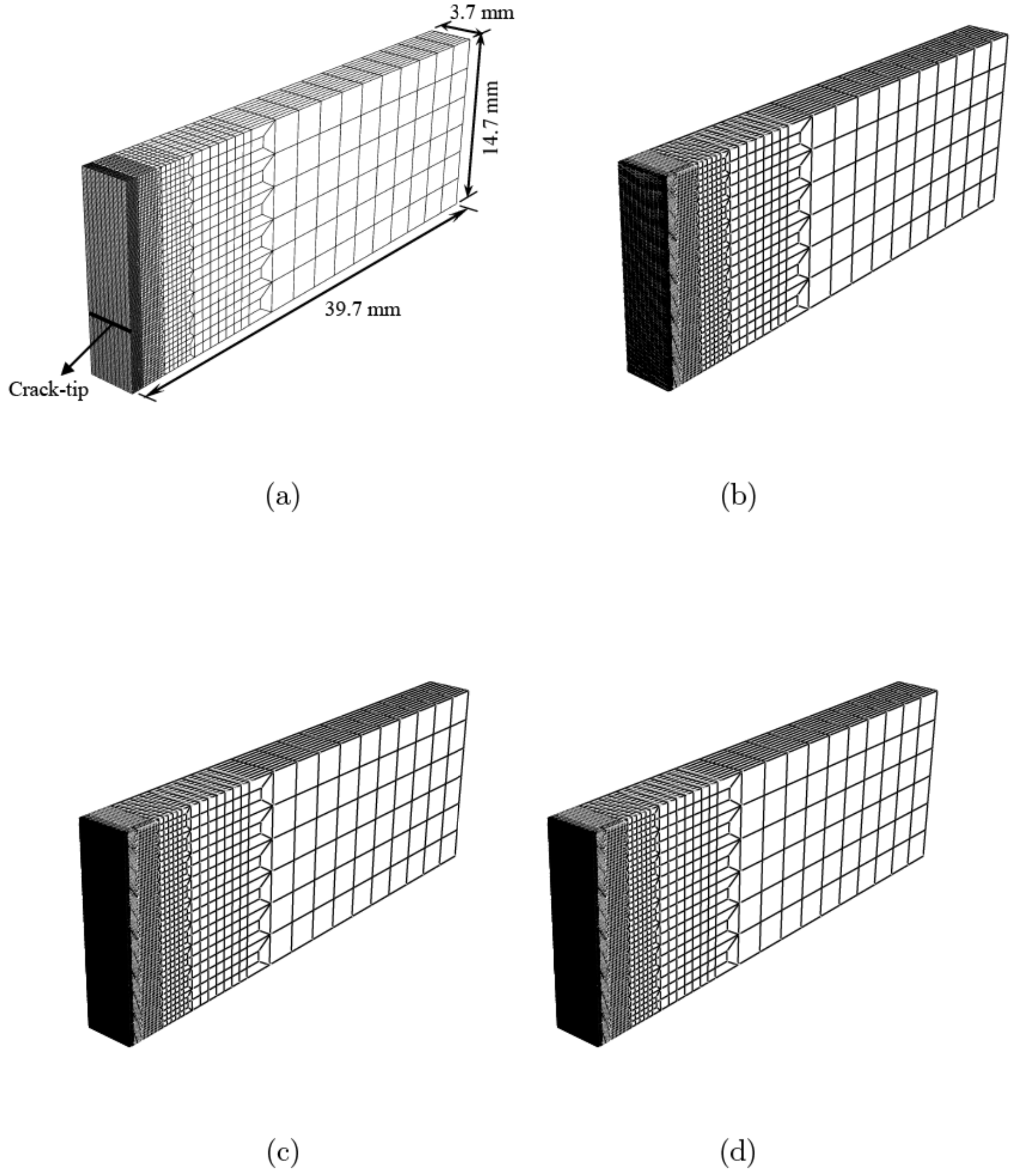

Figure 4.14. TiB / Ti FGM SENB specimen finite element meshes used for (a) Model #1, (b) Model #2, (c) Model #4 and (d) Model #7

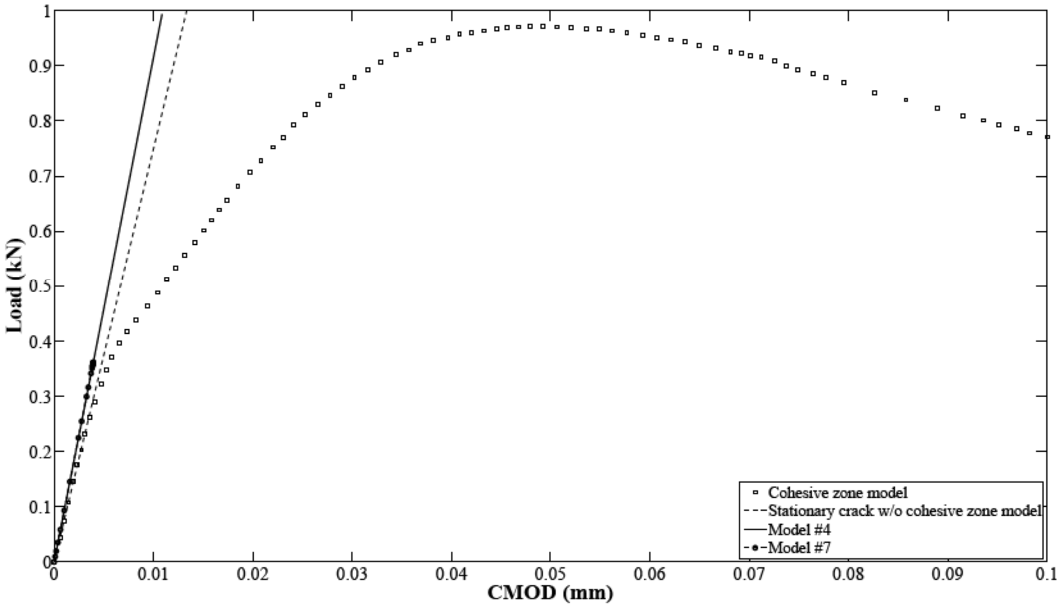

Figure 4.15. Cohesive zone model [41] , stationary crack w/o cohesive zone model [41] and GTN model load versus crack mouth opening displacement results for TiB / Ti FGM SENB specimen

4.2.1. Failure of Homogeneously Ultraviolet Irradiated Polyethylene Carbon Monoxide Co-polymer Specimens

Numerical implementation of the GTN model to polymers is limited compared to that for metals primarily because the void nucleation growth and coalescence process is not present in most polymers in the same way it is in metals. However, the GTN model is a continuum softening and failure model, so appropriate selection of parameters could make the model applicable to other situations that may not involve at the microscale void growth mechanisms similar to those exhibited in metals. For example, Jeong [50] modified the Gurson yield function by combining it with Coulomb's yield function, and calculated cavitation and plastic zone sizes for a rubber-modified epoxy specimen under symmetric double-edge double-notched four-point bending. Fracture toughness of steel compact tension (CT) specimens bonded with rubber-modified epoxy and bulk rubber-modified epoxy single edge notched bending (SENB) specimens were investigated numerically using GTN model by Imanaka *et al.* [51]. Numerical and experimental relations between J-integral values and crack extension were compared there for both the CT and SENB specimens. Using the GTN model for damage accumulation, Zaïri *et al.* [52, 53] studied both experimentally and numerically the uniaxial tensile and volumetric strain response of a rubber toughened polymethylmethacrylate and high impact polystyrene for different strain rates at room temperature. Zaïri *et al.* [54] also studied equal channel angular extrusion and uniaxial tensile tests for polypropylene specimens, again using GTN model. In Challier *et al.* [55] and Laiarinandrasana *et al.* [56], the effects of strain rate and temperature on mechanical properties (elastic, plastic, viscous and GTN model parameters) were investigated for polyvinylidene fluoride (PVDF) by comparing experimental and numerical stress-strain responses for smooth, circumferentially notched round specimens and load-crack opening displacement responses for single edge notched bending (SENB) specimens. The mechanical behavior of porous polymers with different volume fraction of voids under different macroscopic stress triaxiality was investigated numerically by Riku *et al.* [57] using a unit cell computation, and theoretical results based on a modified Gurson model. Their results showed little dependence on the arrangement of voids.

Although generally a good agreement has been obtained between numerical and experimental results in the above-mentioned studies of polymers, there is no specific framework on how GTN model parameters can be consistently determined from experiments on polymeric materials, or how a link between uniaxial and fracture response can be made. Typically either tensile or fracture response was investigated independently, and no attempts have been made to connect the two in a common minimization framework. Making such a connection in the context of a robust optimization framework is one of the goals of this effort.

Several studies in the past have used optimization methods for determination of GTN model parameters from experiments, either tensile or fracture, but this has been done exclusively for metals. The studies discussed above for polymers either do not involve any experiments or do not provide details of the determination process of GTN model parameters. Aoki *et al.* [58] used Kalman filtering to obtain two nucleation parameters from two numerical tensile test experiments with a centered circular hole and side semi-circular notches for an elastic-plastic material. Kalman filtering was also used by Corigliano *et al.* [59] to obtain the GTN yield function coefficients from three point bending experiments of steel single edge notched specimens. Mahnken [60] used a Newton-like algorithm given by Bertsekas combined with the Broyden-Fletcher-Goldfarb-Shanno (BFGS) method to obtain GTN parameters for an axisymmetric tensile test specimen made of steel. A gradient based method using a Levenberg-Marquardt algorithm (LMA) was employed to obtain initial, coalescence and failure void volume fractions, nucleation parameters, power hardening coefficient and initial yield values for a structural steel by Springmann and Kuna [61, 62]. Broggiato *et al.* [63] used the Nelder-Mead simplex method to obtain initial, coalescence and failure void volume fractions, nucleation parameters using multi-section optical data acquired from round-notched steel tensile specimens.

The goal of the present work is to explore the applicability of the GTN model to a photodegradable polyethylene carbon monoxide (ECO) co-polymer and to obtain corresponding parameters for the GTN model through a robust optimization process that will couple experimental results from *two* different configurations: uniaxial tension and edge notched fracture.

4.2.1.1. Problem Geometry and FE Model. In the finite element analyses, q_3 is taken to be equal to q_1^2 (which results in $f_U = \dfrac{1}{q_1}$). The initial value of void volume fraction f_0 is 0 because cavities do not preexist in glassy polymers unlike in metals as discussed by Schirrer [64]. A is taken to be constant to decrease the number of parameters to be optimized. Finally the yield function and the evolution of void volume fraction can be written in the following form:

$$\begin{aligned} \phi &= \left(\frac{\sigma_{eqv}}{\sigma_Y}\right)^2 + 2\, f^*\, q_1\, \cosh\left(-\, q_2\, \frac{3\sigma_h}{2\sigma_Y}\right) - (1 + (q_1\, f^*)^2) = 0, && (4.6)\\ \dot{f} &= (1-f)\, \dot{\epsilon}^P_{kk} + A\, \dot{\epsilon}^P_{eqv}, && (4.7) \end{aligned}$$

Failure occurs when f reaches f_F ($f^* = f_U$).

The experimental results used in this part are taken from the work done by Abanto-Beuno [23] and Abanto-Bueno and Lambros [47]. In the interest of brevity only a summary of the experimental details is not given here. The reader is referred to the above references for more details. Polyethylene carbon monoxide (ECO) becomes stiffer and more brittle when exposed to ultraviolet (UV) irradiation. Thin sheets of ECO (thickness 0.406 mm) 170 mm × 150 mm were artificially UV irradiated for different periods of time: 0.25, 0.5, 1, 1.5, 2, 3, 5, 42, 100, and 130 hour(s), and are cut into the tensile and fracture specimen geometries shown on the right in Figure 4.16. In this work only the 5, 42 and 130 hours UV irradiated ECO specimens, labeled ECO 5, ECO 42 and ECO 130, respectively, are studied. The bulk material properties used for ECO in this work are tabulated in Table 4.5. Note that Poisson's ratio and density don't exhibit a significant change with UV radiation. The specimen dimensions used in the experiments, which are the ones modeled here, are shown in Figure 4.16. The crosshead speed used in the experiments was 0.5 mm/min (approximately 0.01 mm/s).

Table 4.5. Calculated and measured mechanical properties of ECO

Material property	virgin ECO	ECO 5	ECO 42	ECO 130
Elastic modulus, E (MPa) †	178	223	277	332
Poisson's ratio, ν ‡	0.45	0.45	0.45	0.45
Initial yield stress, σ_0 (MPa) †	1.18	1.28	1.37	1.45
Density, ρ (kg/m^3) §	960	960	960	960

† Calculated using experimental tension test results given by [23].

‡ Measured by [65].

§ Measured by [23].

The GTN model is implemented using finite elements (Abaqus/Explicit) and an inverse procedure to determine model parameters is used. The in-plane mesh used to model the uniaxial tension specimen is shown in Figure 4.17. The mesh has 1625 linear hexahedral elements of type C3D8R with 3528 nodes. Using symmetry, 1/8th of the entire specimen is modeled. The element size is $0.385 \times 0.4 \times 0.203$ mm^3 and a uniform mesh is used. To simulate progressive failure of multiple elements, Abaqus/Explicit is used. A displacement loading rate of 0.1 mm/s, as used in the experiments, would produce simulations of excessively long duration. The GTN model rate sensitivity is studied numerically, and rate-dependency is not observed in numerical simulations of up to a loading of 10 mm/s. Therefore, to reduce computational time a 10 mm/s rate is used as the applied displacement rate at location $y = 50$ mm - the top of the

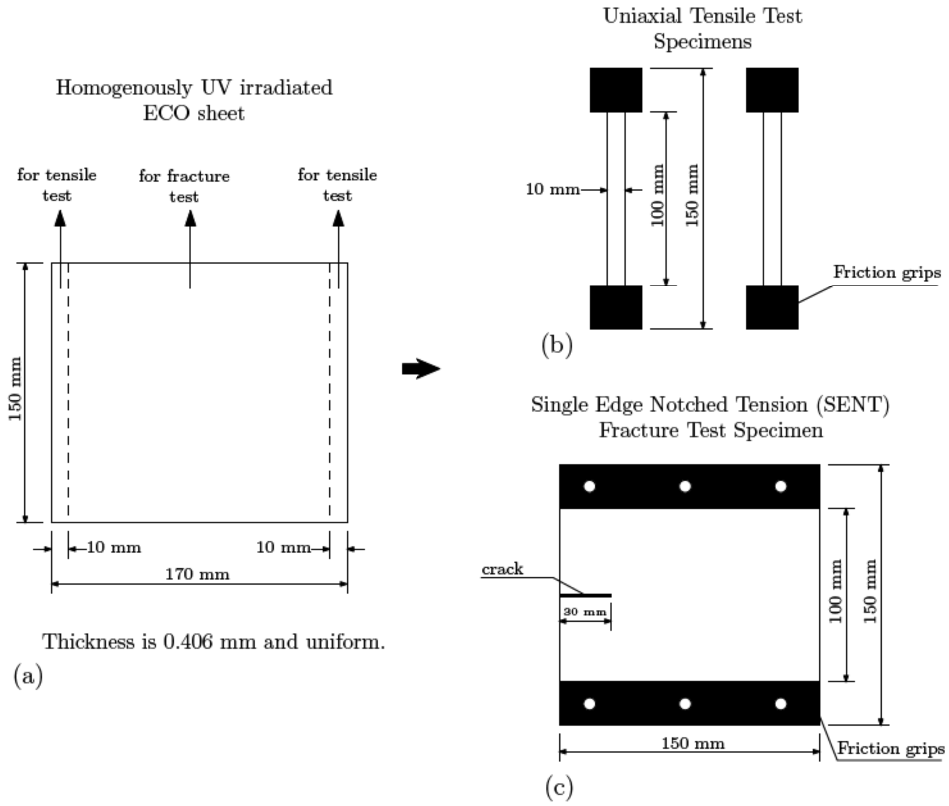

Figure 4.16. Geometry of (a) UV irradiated ECO sheet; (b) tensile and (c) fracture specimens obtained from this sheet [23, 47]

tension specimen. Note that this parametric rate sensitivity study only investigates rate dependence in the GTN model and is independent from material rate sensitivity. Since no rate sensitivity is seen in the GTN model, material rate sensitivity could be studied by extracting properties from different rate experiments, although in this study only one set of experiments at a single loading rate is used. Bulk elastic and plastic material properties are taken from experimental results up to ultimate tensile strength, σ_{UTS}, where necking initiates. After σ_{UTS}, the bulk behavior stress value is kept constant at the ultimate value, as observed in the experiments until failure. Isotropic hardening is assumed for the bulk plastic flow.

Softening behavior is introduced numerically by applying the GTN model, but only to the bottom row elements in the mesh of Figure 4.17, thus forcing failure to occur at the line of symmetry of the sample. Thus, only the bottom row of elements is capable of softening in this configuration. This introduces a softening length scale in the problem (the height of the elements). It is known that such a length scale dependence is present in the GTN model, and one question that arises is how to specify this length scale. As discussed in more detail later, in the present work selection of this length scale is made from the experimentally observed failure region which is around 300-400 microns in half-height [66]. Note that applying the GTN model to only a single row of elements where failure is expected, as is done here, is a common technique sometimes called the "computational cells" method as proposed by Xia and Shih [34, 35], and used and discussed in [36, 67–72].

Figure 4.17. Finite element mesh for homogeneous ECO uniaxial tensile test specimen

For the single edge notched Tensile (SENT) fracture specimen, $1/4^{\text{th}}$ of the entire specimen is discretized, the dimensions of the model being 150 × 50 × 0.203 mm^3. The GTN model parameters will depend on mesh size, as stated above. Although the tensile testing experiments described above may not provide an inherent length scale for failure, in the fracture experiments failure is produced by a single craze originating from the crack-tip [23]. Thus, unlike the case of ductile metals where the failure region size may not be known, here the craze has been experimentally measured to be around 300-400 microns in half-height, although this would depend to some extent on the level of irradiation. Therefore in these simulations softening GTN elements are again placed only directly ahead of the crack-tip and given a height of 400 microns (which is also kept the same for the tensile experiments described above). Thus, by combining both the fracture and tensile loading experiments in this work it is able to specify the length scale over which softening will occur. Consequently the graded in-plane mesh shown in Figure 4.18 is used to model the fracture experiments with the smallest element size chosen to be 0.4 × 0.4 × 0.203 mm^3 which is close to the half size of a craze. The mesh has 2909 linear hexahedral elements of type C3D8R with 6288 nodes. The crack surface (0 mm $< x <$ 30 mm & $y = 0$ mm) is kept traction free, and as before a 10 mm/s displacement rate is applied at $y = 50$ mm. Material properties are the same as the tensile test's specimen. Note that in this particular case in order to check the validity of results, a simulation in which the GTN model is applied to all elements of the mesh is also conducted.

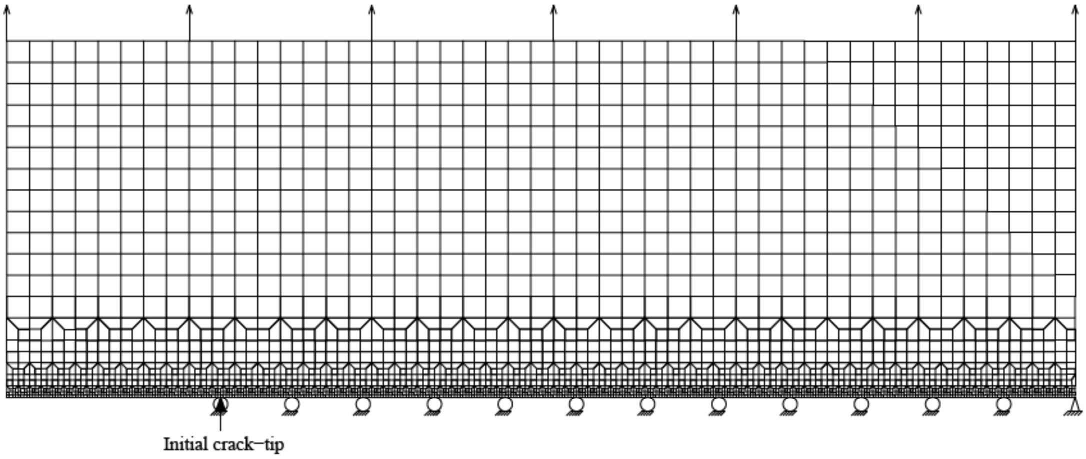

Figure 4.18. Finite element mesh for homogeneous ECO SENT fracture test specimen

The bulk elastic-plastic properties of the surrounding elements are taken directly from experiments as entire stress-strain curves which are tabulated for the purposes of the numerical simulations. As mentioned above, the only modifications made to the experimental stress - strain curves is that, if needed in the simulations, they would not soften but rather would remain at a maximum value of σ_{UTS} if the strain evolved beyond that measured experimentally. Therefore only the GTN parameters of the single row of "cells" are unknown and need to be determined by minimizing a particular objective function (see below). Minimization is done using the Nelder - Mead simplex method which is a direct search method that does not use numerical or analytic gradients, and can overcome discontinuities near the optimal solution. In the case studied here, discontinuities may arise as a result of failure of the specimen. To obtain optimum GTN model parameters numerical results are correlated with experimental nominal stress–strain values (tension specimen) or load–displacement values (fracture specimen). Three different optimization calculations are performed as shown below for; *i*) the tensile specimen, *ii*) the fracture specimen, and *iii*) the tensile and fracture specimens together, for each different UV irradiation time, corresponding to varying amounts of ductility. Two different types of objective functions are used that are sum of difference between squares of experimental and numerical results indicated with Φ_i, and the other one is in least squares sense indicated with ϕ_i and are given as follows:

$$\Phi_1(p) = \sum_{n=0}^{N} |\,\bar{\sigma}_n^2 - \sigma_n(p)^2| \quad \text{for the tensile test,} \tag{4.8a}$$

$$\Phi_2(p) = \sum_{m=0}^{M} |\,\bar{L}_m^2 - L_m(p)^2| \quad \text{for the fracture test,} \tag{4.8b}$$

$$\Phi_3(p) = w_\Phi \sum_{n=0}^{N} |\,\bar{\sigma}_n^2 - \sigma_n(p)^2| + \sum_{m=0}^{M} |\,\bar{L}_m^2 - L_m(p)^2| \quad \text{for the tensile and fracture tests together,} \tag{4.8c}$$

$$\phi_1(p) = \sum_{n=0}^{N} [\,\bar{\sigma}_n - \sigma_n(p)\,]^2 \quad \text{for the tensile test,} \tag{4.9a}$$

$$\phi_2(p) = \sum_{m=0}^{M} [\,\bar{L}_m - L_m(p)\,]^2 \quad \text{for the fracture test,} \tag{4.9b}$$

$$\phi_3(p) = w_\phi \sum_{n=0}^{N} [\,\bar{\sigma}_n - \sigma_n(p)\,]^2 + \sum_{m=0}^{M} [\,\bar{L}_m - L_m(p)\,]^2 \quad \text{for the tensile and fracture tests together,} \tag{4.9c}$$

where p is the parameter set (defined below), $\bar{\sigma}_n$ and $\sigma_n(p)$ are experimentally and numerically evaluated normal stresses, $\bar{L}_m$ are $L_m(p)$ experimental and numerical loads, w_Φ in Equation 4.8c is a weight factor with a value of 1×10^4 and w_ϕ in Equation 4.9c is a weight factor with a value of 1×10^6.

Five parameters are used in the optimization analyses:

$$p = (q_1, q_2, f_c, f_F, A) \tag{4.10}$$

where q_1, q_2, q_3 are GTN yield function coefficients and $q_3 = q_1^2$; f_c, f_F are critical and failure void volume fractions; void nucleation coefficient A is taken constant for the strain controlled void nucleation rate term.

From the numerical simulations of the tensile specimen output quantities are collected at every 1.25×10^{-3} strain intervals up to a total of 0.125 strain for each of the different irradiation time experiments ECO 5, ECO 42, and ECO 130. This yields a total number for N (the total number of points in Equations 4.8a, 4.9a, 4.8c and 4.9c) of 100. For the fracture specimen simulation data are collected at every 0.01 mm applied displacement intervals up to 5.9 mm, 4.9 mm, and 4.1 mm for ECO 5, ECO 42, and ECO 130, respectively. As a result M is 590, 490, and 410 in Equations 4.8b, 4.9b, 4.8c and 4.9c for ECO 5, ECO 42, and ECO 130.

4.2.1.2. Results and Discussion. In this section, optimal GTN model parameters which yield from optimization analyses using the objective functions Φ_i and ϕ_i given in Equations 4.8 - 4.9 for ECO 5, ECO 42 and ECO 130 are presented. Numerical results are plotted with experimental results both for tensile and fracture test specimens.

(i) 5 Hours UV Irradiated ECO: The results of the minimization process, experimental and numerical stress - strain response of tensile test specimen and load - applied displacement response of fracture test specimen for ECO 5 are shown in Figures 4.19, and 4.20, respectively where Φ_i is used as objective functions in Equation 4.8. Similarly response of tensile and fracture test specimens are plotted in Figures 4.21, and 4.22, respectively where ϕ_i is used as objective functions in Equation 4.9. Optimized GTN model parameters are tabulated in Tables 4.6 and 4.7 using Φ_i and ϕ_i as objective functions, respectively.

Table 4.6. Optimized Gurson model parameters and objective function values for ECO 5 simulations (Φ_i (i=1,2,3) are given in Equations 4.8a-c)

Case	Optimized Gurson Model Parameters					Objective Function Values		
	q_1	q_2	f_c	f_F	A	Φ_1	Φ_2	Φ_3
ϕ_1 minimization	3.041	1.073	0.148	0.247	0.1274	21.0	N/A	N/A
ϕ_2 minimization (row GTN)	2.674	0.895	0.221	0.288	0.1069	320	4311380	7511380
ϕ_2 minimization (full GTN)	3.365	0.657	0.194	0.295	0.1542	244	3769809	6209809
ϕ_3 minimization (row GTN)	3.135	0.656	0.176	0.299	0.1646	24.0	5238898	5479098
ϕ_3 minimization (full GTN)	3.365	0.655	0.189	0.293	0.1542	26.8	3790205	4058305

Table 4.7. Optimized GTN model parameters and objective function values for ECO 5 simulations (ϕ_i (i=1,2,3) are given in Equations 4.9a-c)

Case	Optimized GTN Model Parameters					Objective Function Values		
	q_1	q_2	f_c	f_F	A	ϕ_1	ϕ_2	ϕ_3
ϕ_1 minimization	3.044	1.073	0.152	0.246	0.1273	0.0539	N/A	N/A
ϕ_2 minimization (row GTN)	3.050	0.539	0.224	0.325	0.1586	348	678167	348678167
ϕ_2 minimization (full GTN)	3.047	0.547	0.218	0.328	0.1640	254	592887	254592887
ϕ_3 minimization (row GTN)	3.136	0.660	0.176	0.307	0.1649	0.0836	2229964	2313564
ϕ_3 minimization (full GTN)	3.136	0.660	0.178	0.318	0.1649	0.0853	1603151	1688451

Figures 4.19 and 4.21 show the nominal stress - strain relation measured during the uniaxial tension experiment along with the numerically predicted response using the optimized GTN properties with Equations 4.8a and 4.9a as a minimization function, i.e. minimizing solely based on this experimental stress - strain curve (square symbols). In addition to this, it is possible to make a combined minimization using both the tensile and the fracture results (Figures 4.19 - 4.22) through Equations 4.8c and 4.9c. In this case somewhat different GTN parameters are obtained, as is seen in Tables 4.6 and 4.7. In the combined function minimization case (Equations 4.8c and 4.9c) two cases have been considered, one where the softening elements are placed everywhere (crosses in Figures 4.19 and 4.21) and one where only one single row of softening elements is placed ahead of the crack-tip, i.e. the computational cells method, (circles in Figures 4.19 and 4.21). It is clear from Figures 4.19 and 4.21 that all three cases produce excellent agreement with the experimental results and are virtually indistinguishable from each other. This implies that attempting to use solely a single uniaxial tension test experimental results to uniquely identify the GTN failure parameters is difficult.

Figures 4.20 and 4.22 show results for the applied load vs. load line displacement for the ECO 5 case. If the tension test results are fitted on their own, Equations 4.8a and 4.9a, and the resulting properties are used to predict the fracture response, then the predicted results (square symbol) deviate considerably from the experimental results, so from now on Φ_1 and ϕ_1 minimization results will not be shown for SENT fracture specimen responses. If the fracture load - displacement curve is used on it own, i.e. Equations 4.8b and 4.9b are minimized, then the curves in Figures 4.20 and 4.22 are obtained shown as triangles (full GTN model for entire mesh) and pluses (single row GTN elements). As is seen, this predicted response is an improvement over the results obtained by solely optimizing stress - strain, but it over predicts the failure load considerably. Note however, that there is little difference between the full GTN model and the computational cells model. However when comparing the model prediction for a uniaxial response based on the Φ_2 and ϕ_2 minimizations only, the results, shown as plus symbols (single row GTN elements) and triangle symbols (full GTN model for entire mesh) in Figures 4.19 and 4.21, respectively, are poor compared to the previous ones, and from now on Φ_2 and ϕ_2 minimization results will not be shown for uniaxial specimen responses. Therefore one cannot obtain a consistent set of optimized properties by minimizing separately either the uniaxial response or the SENT fracture experimental data.

In an attempt to improve the fit quality, functions in Equations 4.8c and 4.9c are next minimized which performs a simultaneous minimization of the uniaxial and fracture test data. The results for the computational cells model (circle symbols) and the full model (cross symbols) are also plotted in Figures 4.20 and 4.22. The results agree quite well with the previous minimization up to about peak load, which is now better estimated, although maximum displacement is considerably underestimated with the combined peak properties. Comparing Figures 4.19 - 4.22 clearly shows that the fracture experiment is much more sensitive to the model parameters, particularly after peak load, than the uniaxial response, and it is especially difficult to accurately predict both peak load and peak displacement. However, the combined minimization does produce excellent agreement for the uniaxial response and reasonable agreement for the fracture response, and is therefore considered representative of the material.

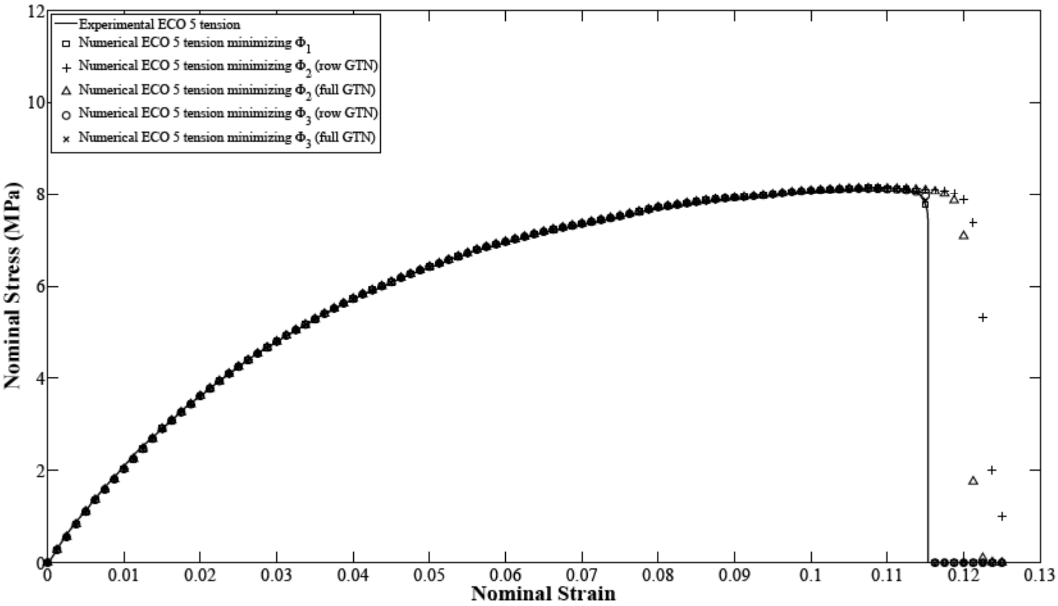

Figure 4.19. Stress - strain response for ECO 5 tension specimen where Φ_i (Equation 4.8) is used

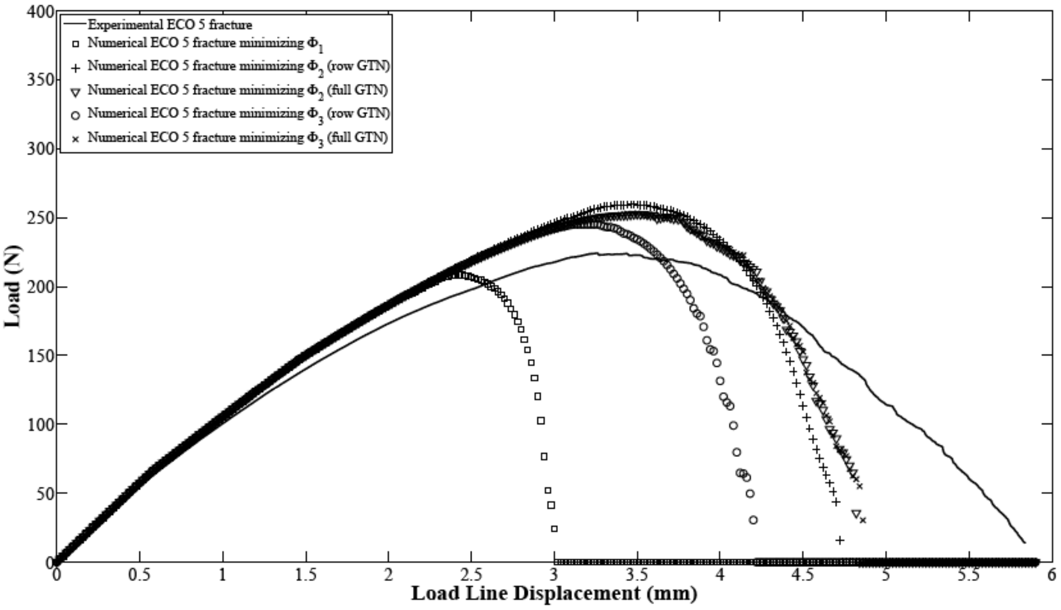

Figure 4.20. Load - displacement response for ECO 5 fracture specimen where Φ_i (Equation 4.8) is used

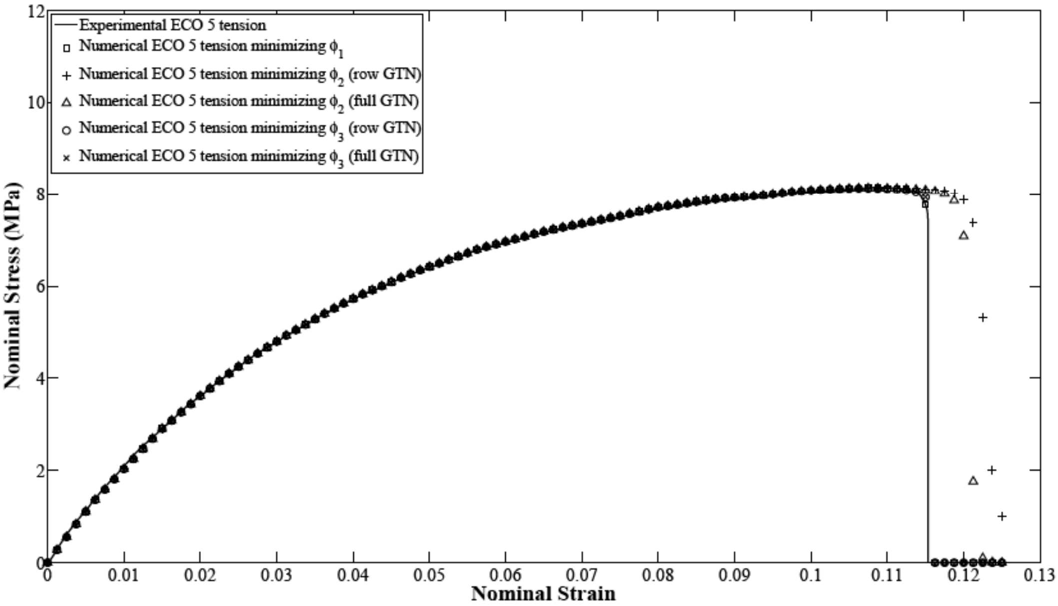

Figure 4.21. Stress - strain response for ECO 5 tension specimen where ϕ_i (Equation 4.9) is used

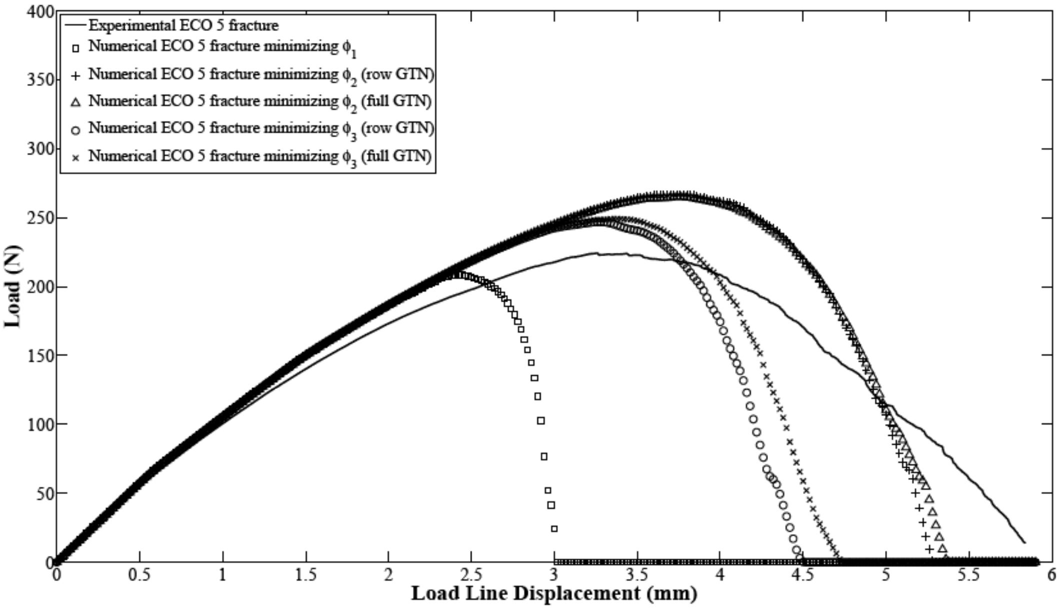

Figure 4.22. Load - displacement response for ECO 5 fracture specimen where ϕ_i (Equation 4.9) is used

(ii) 42 Hours UV Irradiated ECO: Experimental and numerical stress - strain response of tensile test specimen and load - applied displacement response of fracture test specimen for 42 hours UV irradiated ECO (ECO 42) are plotted in Figures 4.23, and 4.24, respectively where Φ_i is used as objective function Equation 4.8. Similarly response of tensile and fracture test specimens are plotted in Figures 4.25, and 4.26, respectively where ϕ_i is used as objective function Equation 4.9. Optimized Gurson model parameters are tabulated in Tables 4.8 and 4.9 using Φ_i and ϕ_i as objective functions, respectively.

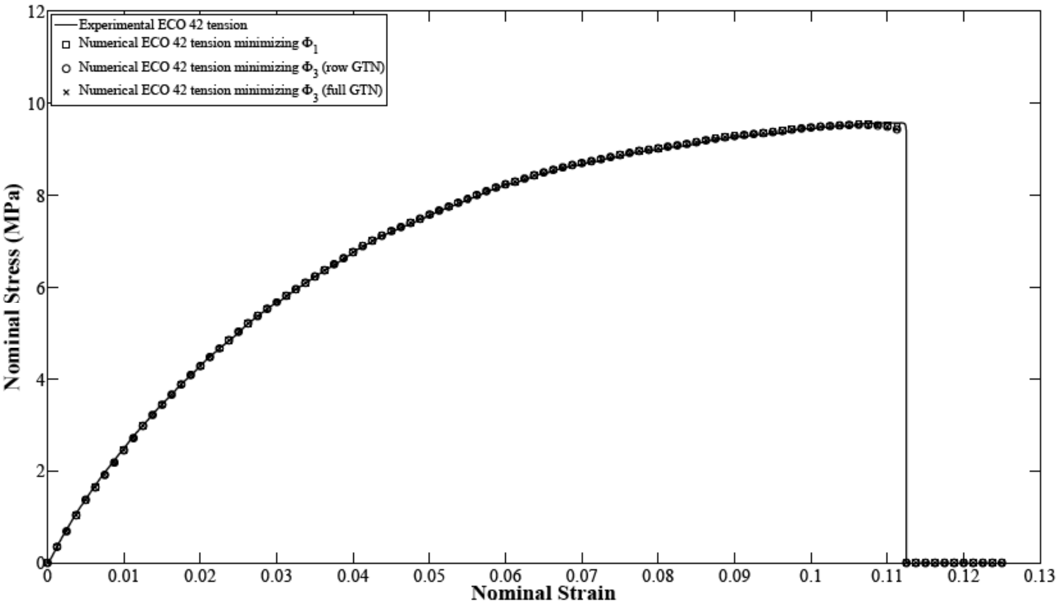

Figure 4.23. Stress - strain response for ECO 42 tension specimen where Φ_i (Equation 4.8) is used

Table 4.8. Optimized Gurson model parameters and objective function values for ECO 42 simulations (Φ_i (i=1,2,3) are given in Equations 4.8a-c)

Case	Optimized Gurson Model Parameters					Objective Function Values		
	q_1	q_2	f_c	f_F	A	Φ_1	Φ_2	Φ_3
ϕ_1 minimization	2.918	1.199	0.131	0.179	0.1312	29.4	N/A	N/A
ϕ_2 minimization (row GTN)	2.514	1.015	0.173	0.200	0.1151	N/A	4534136	N/A
ϕ_2 minimization (full GTN)	3.168	0.746	0.152	0.267	0.1579	N/A	4315588	N/A
ϕ_3 minimization (row GTN)	3.173	0.871	0.144	0.239	0.1558	30.9	6602284	6911684
ϕ_3 minimization (full GTN)	3.170	0.866	0.148	0.245	0.1562	30.9	5989934	6298634

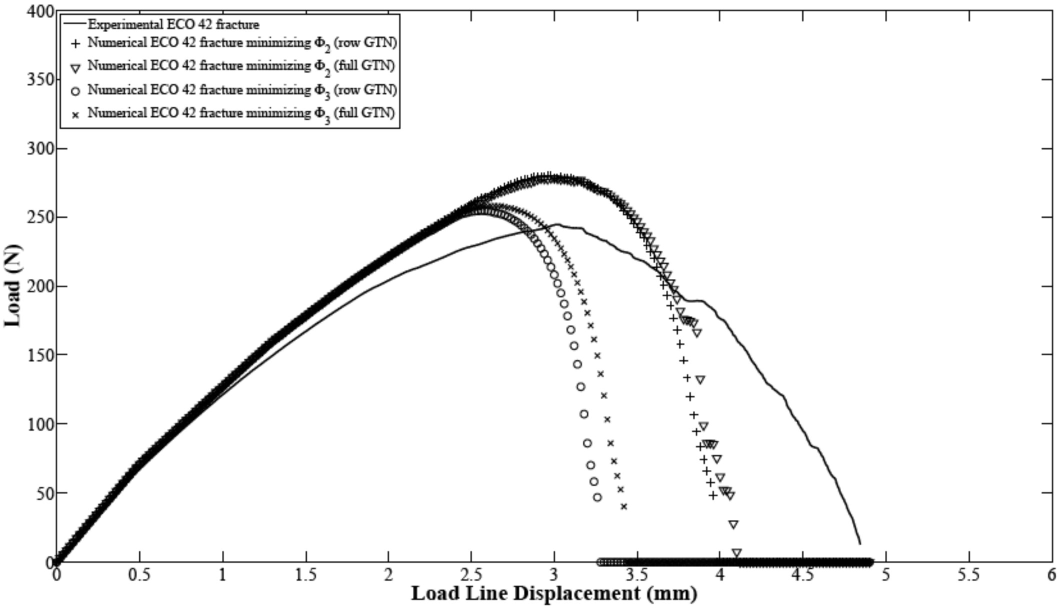

Figure 4.24. Load - displacement response for ECO 42 fracture specimen where Φ_i (Equation 4.8) is used

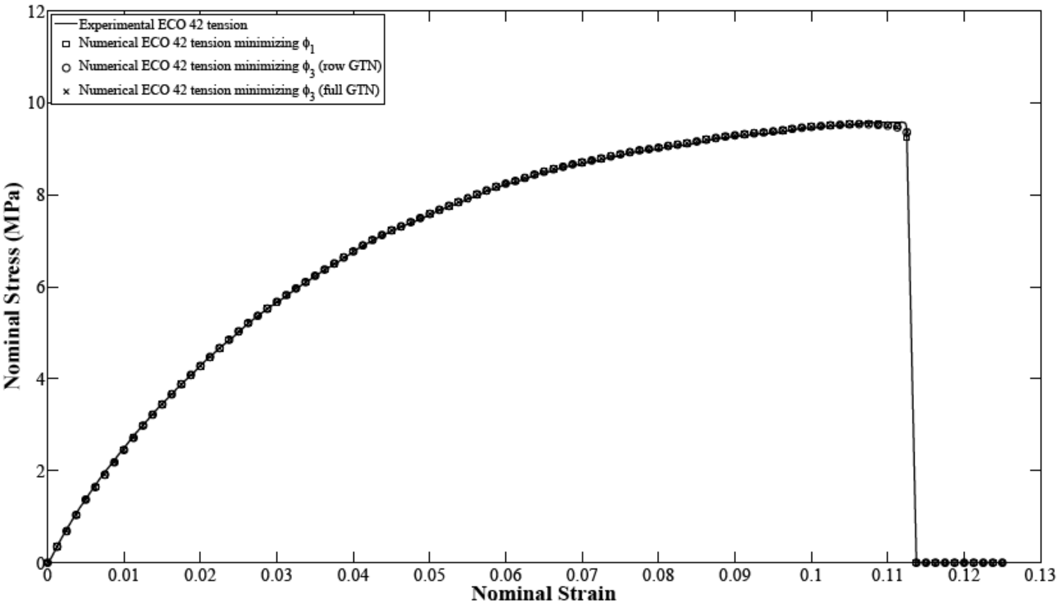

Figure 4.25. Stress - strain response for ECO 42 tension specimen where ϕ_i (Equation 4.9) is used

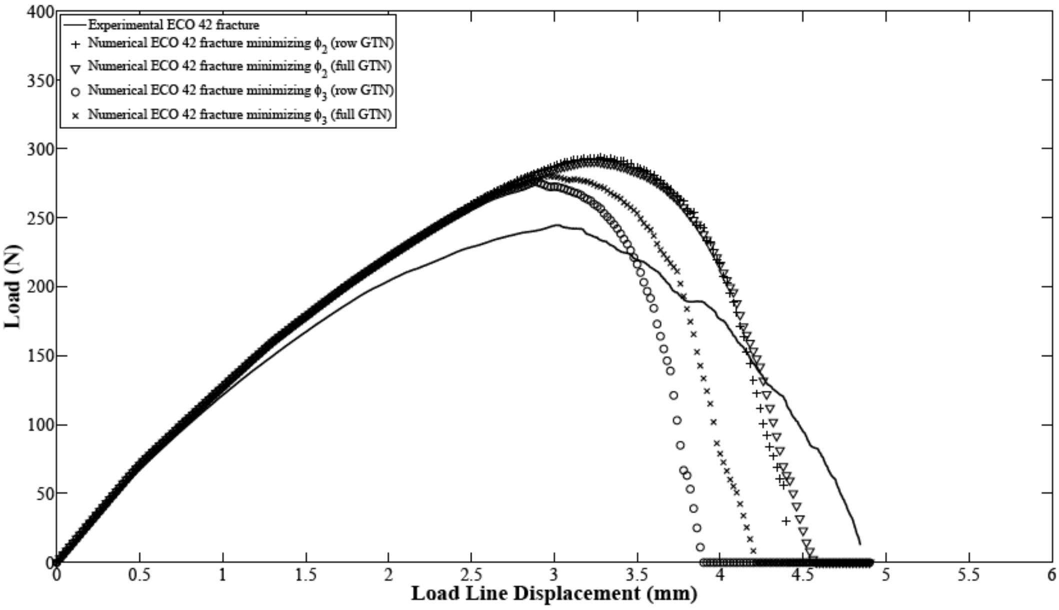

Figure 4.26. Load - displacement response for ECO 42 fracture specimen where ϕ_i (Equation 4.9) is used

Table 4.9. Optimized GTN model parameters and objective function values for ECO 42 simulations (ϕ_i (i=1,2,3) are given in Equations 4.9a-c)

Case	Optimized Gurson Model Parameters					Objective Function Values		
	q_1	q_2	f_c	f_F	A	ϕ_1	ϕ_2	ϕ_3
ϕ_1 minimization	3.122	1.104	0.153	0.163	0.1302	0.0592	N/A	N/A
ϕ_2 minimization (row GTN)	2.971	0.709	0.169	0.302	0.1533	N/A	779077	N/A
ϕ_2 minimization (full GTN)	2.919	0.755	0.171	0.308	0.1587	N/A	631883	N/A
ϕ_3 minimization (row GTN)	3.175	0.748	0.154	0.270	0.1650	0.0784	1945640	2024040
ϕ_3 minimization (full GTN)	3.128	0.735	0.158	0.278	0.1684	0.0817	1103666	1185366

(iii) 130 Hours UV Irradiated ECO: Experimental and numerical stress - strain response of tensile test specimen and load - applied displacement response of fracture test specimen for 130 hours UV irradiated ECO (ECO 130) are plotted in Figures 4.27, and 4.28, respectively where Φ_i is used as objective function Equation 4.8. Similarly response of tensile and fracture test specimens are plotted in Figures 4.29, and 4.30, respectively where ϕ_i is used as objective function Equation 4.9. Optimized Gurson model parameters are tabulated in Tables 4.10 and 4.11 using Φ_i and ϕ_i as objective functions, respectively.

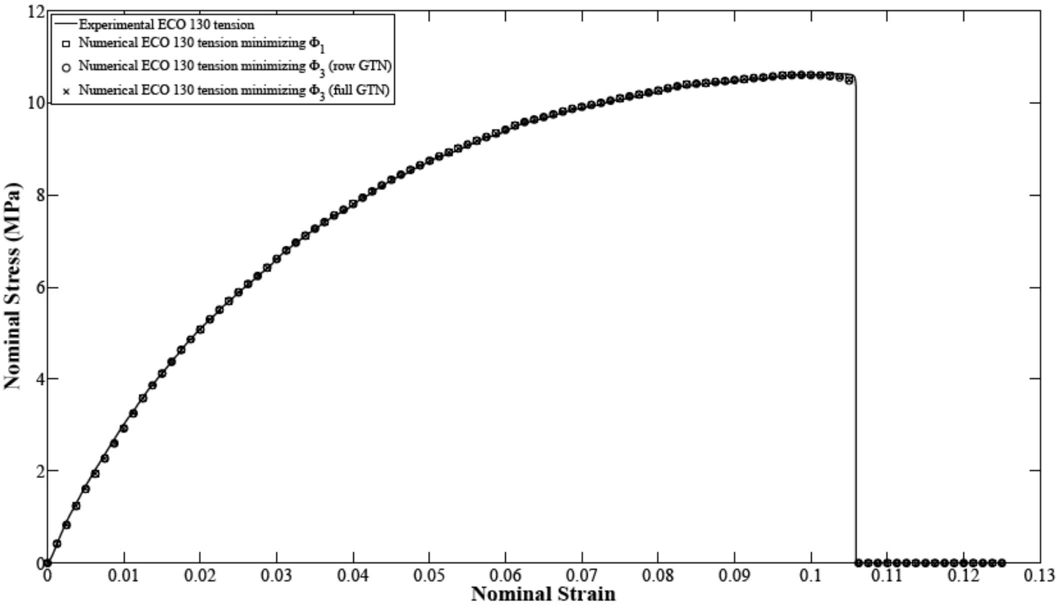

Figure 4.27. Stress - strain response for ECO 130 tension specimen where Φ_i (Equation 4.8) is used

Table 4.10. Optimized Gurson model parameters and objective function values for ECO 130 simulations (Φ_i (i=1,2,3) are given in Equations 4.8a-c)

Case	Optimized Gurson Model Parameters					Objective Function Values		
	q_1	q_2	f_c	f_F	A	Φ_1	Φ_2	Φ_3
ϕ_1 minimization	2.801	1.230	0.155	0.176	0.1272	31.9	N/A	N/A
ϕ_2 minimization (row GTN)	3.428	0.999	0.160	0.219	0.1198	N/A	3773723	N/A
ϕ_2 minimization (full GTN)	3.149	1.023	0.170	0.184	0.1338	N/A	3732422	N/A
ϕ_3 minimization (row GTN)	3.188	1.000	0.166	0.196	0.1338	33.1	3851951	4182751
ϕ_3 minimization (full GTN)	3.139	1.012	0.171	0.181	0.1344	32.8	3757219	4084919

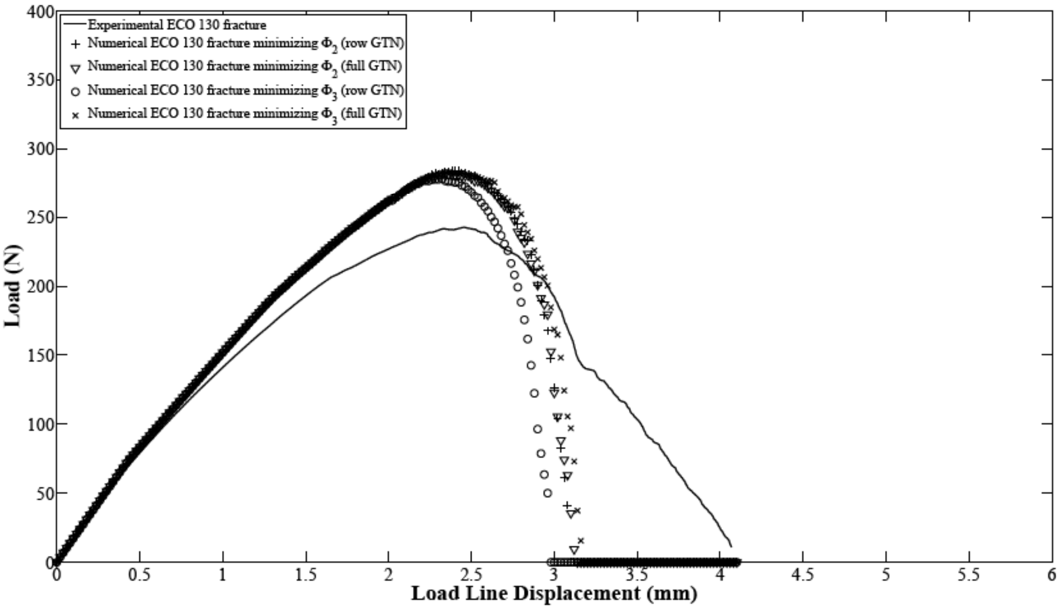

Figure 4.28. Load - displacement response for ECO 130 fracture specimen where Φ_i (Equation 4.8) is used

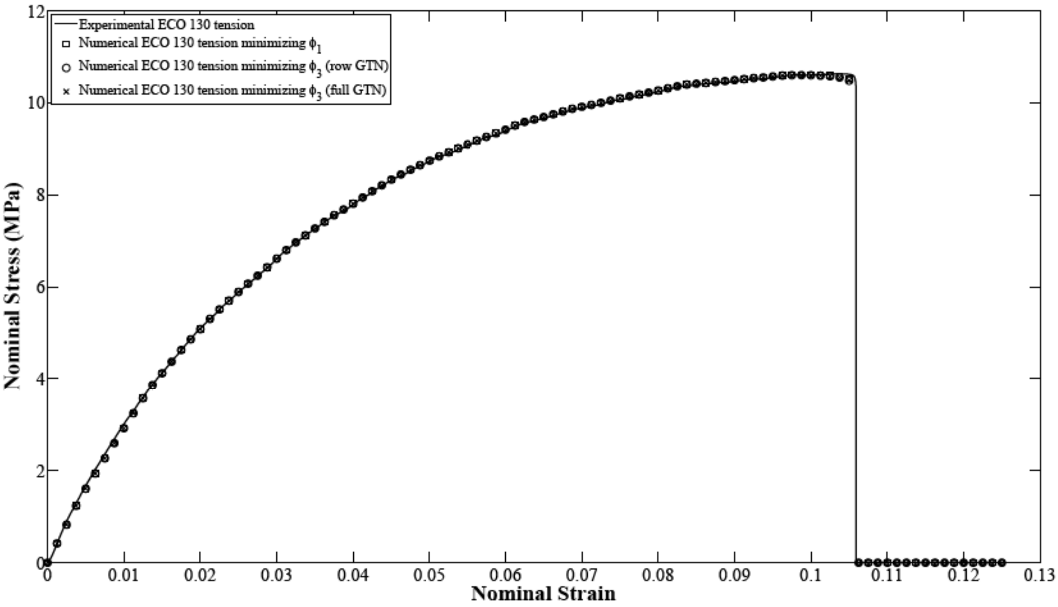

Figure 4.29. Stress - strain response for ECO 130 tension specimen where ϕ_i (Equation 4.9) is used

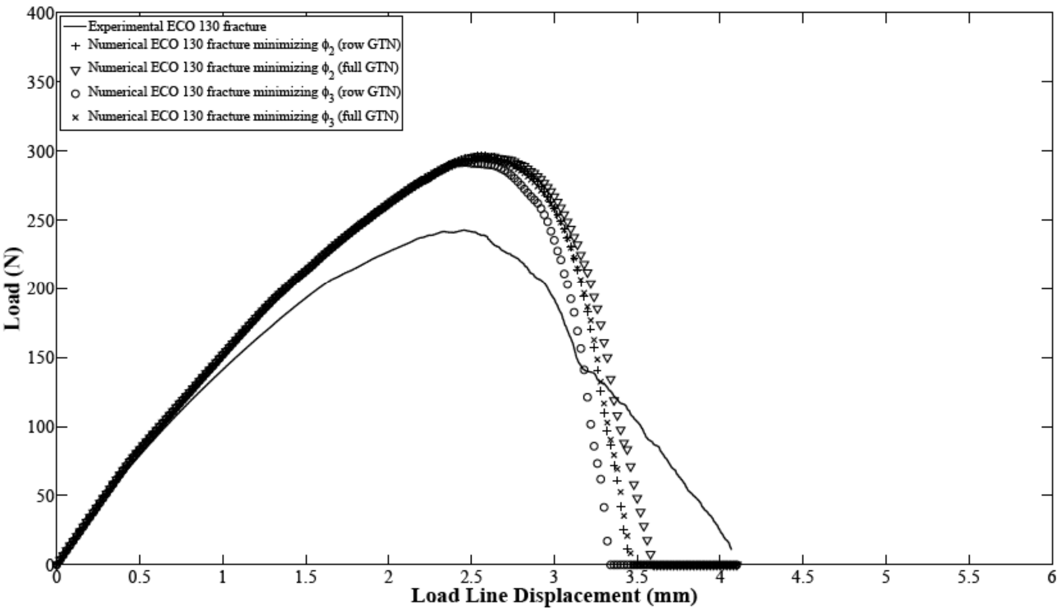

Figure 4.30. Load - displacement response for ECO 130 fracture specimen where ϕ_i (Equation 4.9) is used

Table 4.11. Optimized GTN model parameters and objective function values for ECO 130 simulations (ϕ_i (i=1,2,3) are given in Equations 4.9a-c)

Case	Optimized Gurson Model Parameters					Objective Function Values		
	q_1	q_2	f_c	f_F	A	ϕ_1	ϕ_2	ϕ_3
ϕ_1 minimization	3.130	1.109	0.155	0.166	0.1229	0.0916	N/A	N/A
ϕ_2 minimization (row GTN)	3.160	0.917	0.186	0.216	0.1344	N/A	804134	N/A
ϕ_2 minimization (full GTN)	3.248	0.873	0.186	0.227	0.1478	N/A	742139	N/A
ϕ_3 minimization (row GTN)	3.278	0.936	0.200	0.215	0.1359	0.1054	838478	943878
ϕ_3 minimization (full GTN)	3.280	0.937	0.200	0.219	0.1358	0.1060	769694	875694

The experiments corresponding to ECO 42 and ECO 130 essentially represent different materials, since nominally higher UV irradiation hours would further embrittle the polymer. So the minimization process is repeated separately for each one. Here results are shown for the case of either the individual or the combined minimizations. Similar results are seen, with the combined minimization generally able to better predict peak load, but less so peak displacement. Generally, as irradiation time increases parameters f_c and f_F decrease indicating an embrittlement of the material, as expected. However in the most brittle case, 130 hours of irradiation, the fit is also the worst, which perhaps is also expected since an increasingly brittle material is attempted to model with what is inherently a ductile failure model. Although the goal of this part is not to obtain a specific variation of the GTN parameters with irradiation time, there appears to be a reasonable trend in the results.

Equivalent stress contour plots for the ECO 42 SENT fracture specimen near the initial crack-tip are shown in Figures 4.31(a)-(d) for different loading values using GTN model parameters obtained by minimizing ϕ_3. Similarly, equivalent plastic strain contour plots are shown in Figures 4.32(a)-(d). Both sets of contour plots begin from a fully elastic deformation loading state (at 0.05 mm applied displacement), and end at total failure of the *first* element ahead the initial crack-tip (at 2.67 mm applied displacement). Contour levels are the same for each stress plot, but not for plastic strain plots. Note that, the elements where failure initiates deform significantly because they soften and loose their stress carrying capacity eventually. Therefore, the second contour level for the plastic strain plots is kept constant at 0.05 to clearly visualize the extent of plasticity developing above the failure zone directly ahead of the crack in Figures 4.32(c)-(d). Stress is clearly concentrated on around the “apparent” crack-tip. In Figures 4.31(a)-(b) for early loads, while deformation is still mainly elastic the apparent crack-tip is located at the original crack-tip position. As the elements at the interface accumulate plastic strain (see Figure 4.32(c)), they soften considerably thus causing the apparent crack-tip to move forward since that is where the stress carrying capacity of the material now resides, and consequently, where stress is concentrated. This is reminiscent of the formation and growth of a craze ahead of a crack-tip in a polymeric material. This happens before total failure of the first element which has not reached f_F yet. It is the severe softening that essentially causes the formation of this craze. A process such as this can also be modeled by the concept of a cohesive zone model (CZM), which clearly should be relatable to the GTN model used in this study. In fact, cohesive strength and energy have been predicted using the GTN model to simulate failure and relating the results to a cohesive zone model by Siegmund and Brocks [73], and Anvari [74]. It is the beyond the scope of this study to make such a relation. Figures 4.31-4.32(d) show the equivalent stress and plastic strain contour plots at the instant of total failure of the *first* element ahead the initial crack-tip. Softening is much more severe in this case, so the apparent crack-tip moves forward excessively and plastic strain spreads to a large region of the entire sample.

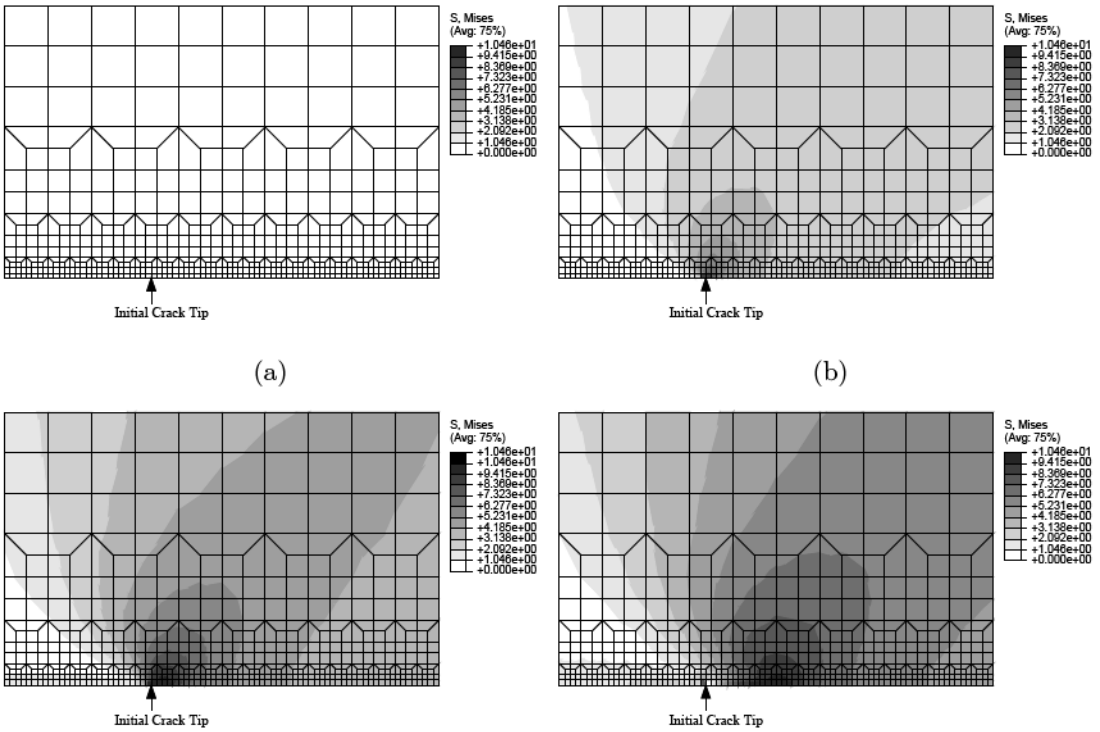

(a) (b)

(c) (d)

Figure 4.31. Evolution of equivalent stress near the crack-tip for ECO 42 SENT fracture specimen at load line displacements of (a) 0.05 mm, (b) 0.9 mm, (c) 1.8 mm, and (d) 2.67 mm using GTN model parameters obtained by minimizing ϕ_3

To compare the three different UV irradiation times, equivalent stress and equivalent plastic strain contour plots are shown in Figure 4.33 for ECO 5, ECO 42 and ECO 130 SENT fracture specimens at a constant applied load line displacement of 2 mm at which level in all three cases significant damage has accumulated ahead of the crack-tip. GTN model parameters obtained by minimizing the combined ϕ_3 have been used. The apparent crack-tip moves further and the magnitude of stresses increases as irradiation time increases, which is a consequence of the material getting more brittle (failure stain decreasing) but also stiffer (stress increases). Perhaps counter intuitively the extent of plasticity is larger for increasing irradiation time, which is due to the decreasing initial yield strain.

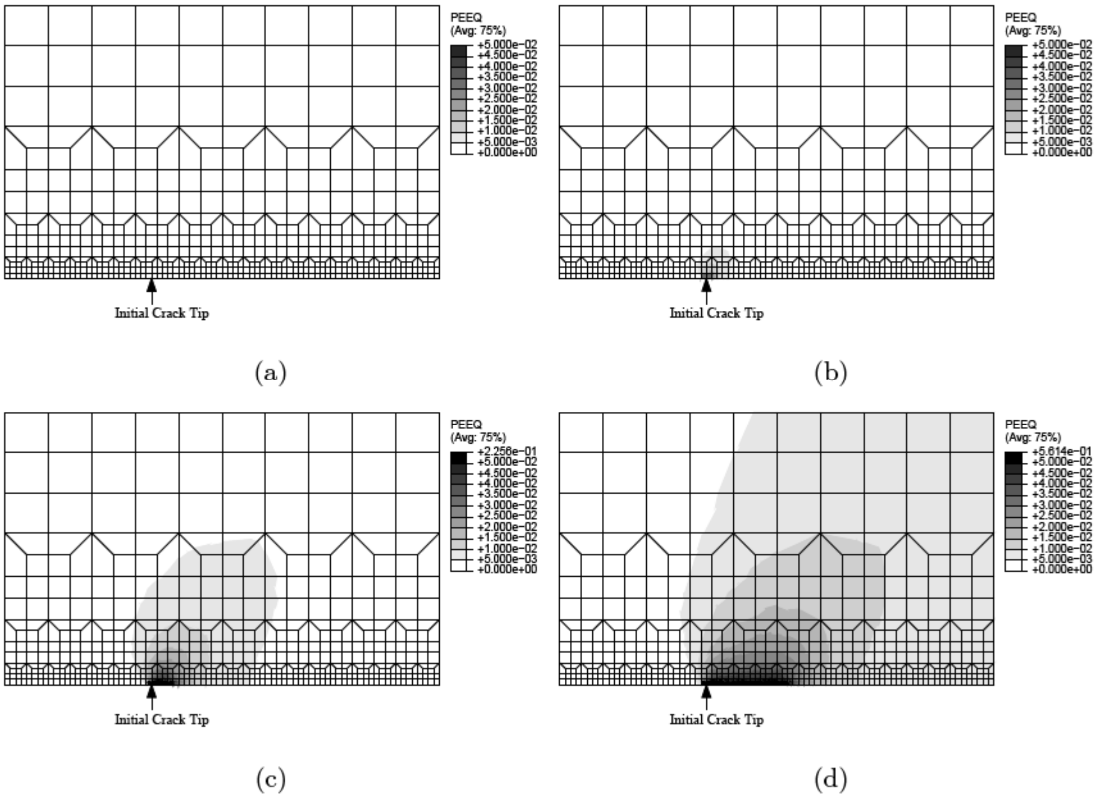

(a) (b)

(c) (d)

Figure 4.32. Evolution of equivalent plastic strain near the crack-tip for ECO 42 SENT fracture specimen at load line displacements of (a) 0.05 mm, (b) 0.9 mm, (c) 1.8 mm, and (d) 2.67 mm using GTN model parameters obtained by minimizing ϕ_3

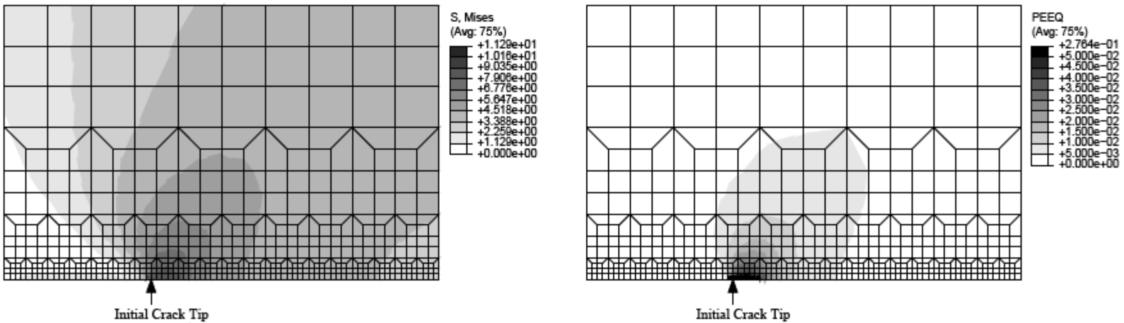

(a) ECO 5, σ_{eqv} (b) ECO 5, ϵ_{eqv}^P

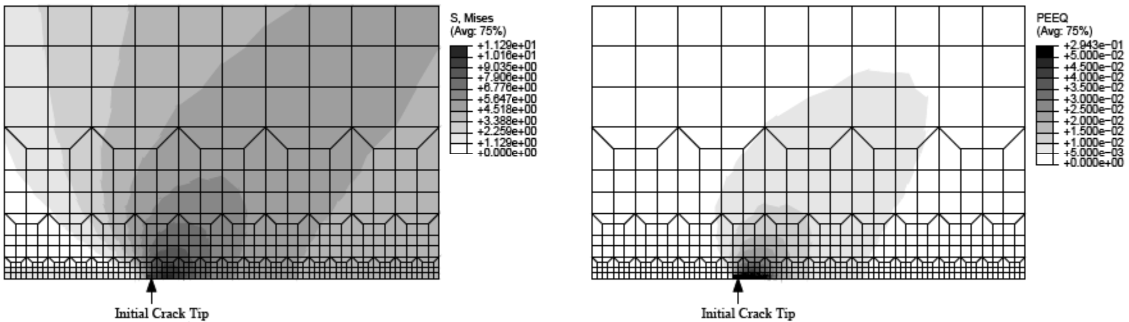

(c) ECO 42, σ_{eqv} (d) ECO 42, ϵ_{eqv}^P

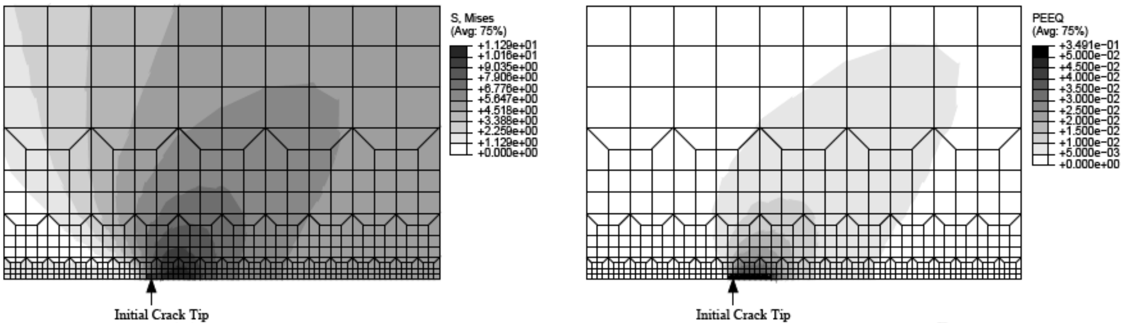

(e) ECO 130, σ_{eqv} (f) ECO 130, ϵ_{eqv}^P

Figure 4.33. Equivalent stress and equivalent plastic strain contour plots for ECO 5, ECO 42, ECO 130 SENT fracture specimens before the total failure of first element ahead the initial crack-tip where load line displacement is 2 mm

4.2.2. Failure of Ultraviolet Irradiated Polyethylene Carbon Monoxide Copolymer FGM Specimens

The FGM samples are manufactured using selective ultraviolet (UV) light irradiation on a photodegradable polyethylene carbon monoxide copolymer (ECO). Typically, a thin sheet (thickness of 0.406 mm) of in-plane dimensions 300 × 150 mm^2 which was irradiated for times varying from 5 h to 300 h. After irradiation, the sheet is cut in half parallel to the irradiation direction, and two samples of 150 × 150 mm^2 are obtained. One of these is then cut perpendicularly to the irradiation direction into 19 strips of roughly 8 mm width, which are used in uniaxial tension tests to measure elastic and failure property variation as a function of position on the sample. The remaining 150 × 150 mm^2 sample from the original sheet is then used for a single edge notch tension (SENT) fracture experiment. Therefore, the variation of local material properties such as elastic modulus, failure stress, and failure strain is measured independently of the fracture experiments, but originating from exactly the same manufacturing process. Mode I fracture of ECO - based FGM SENT specimens are studied experimentally by Abanto-Bueno [23] and numerically by Kandula *et al.* [22]. Failure is modeled using cohesive zone model in numerical studies of Kandula *et al.* [22]. The details of the experimental specimens are shown in Figure 4.34.

Uniaxial tensile tests provide the Young's modulus E, failure stress σ_f, and failure strain ϵ_f as a function of length along the ECO sheet. Figure 4.35 shows the spatial variation of these three quantities obtained for two particular FGMs (named FGM I and II) that are simulated in Kandula *et al.*'s work. Maximum values of material properties λ_{max} are tabulated in Table 4.12. Poisson's ratio for ECO is 0.45 [65].

Failure is simulated using GTN model for FGM II where plasticity is defined by power law hardening in section 4.2.2.1. In section 4.2.2.2, plastic material property variation of the material is taken from experimental uniaxial tension tests data up to ultimate tensile strength, σ_{UTS}, where necking initiates. After σ_{UTS}, the bulk behavior stress value is kept constant at the ultimate value in numerical calculations.

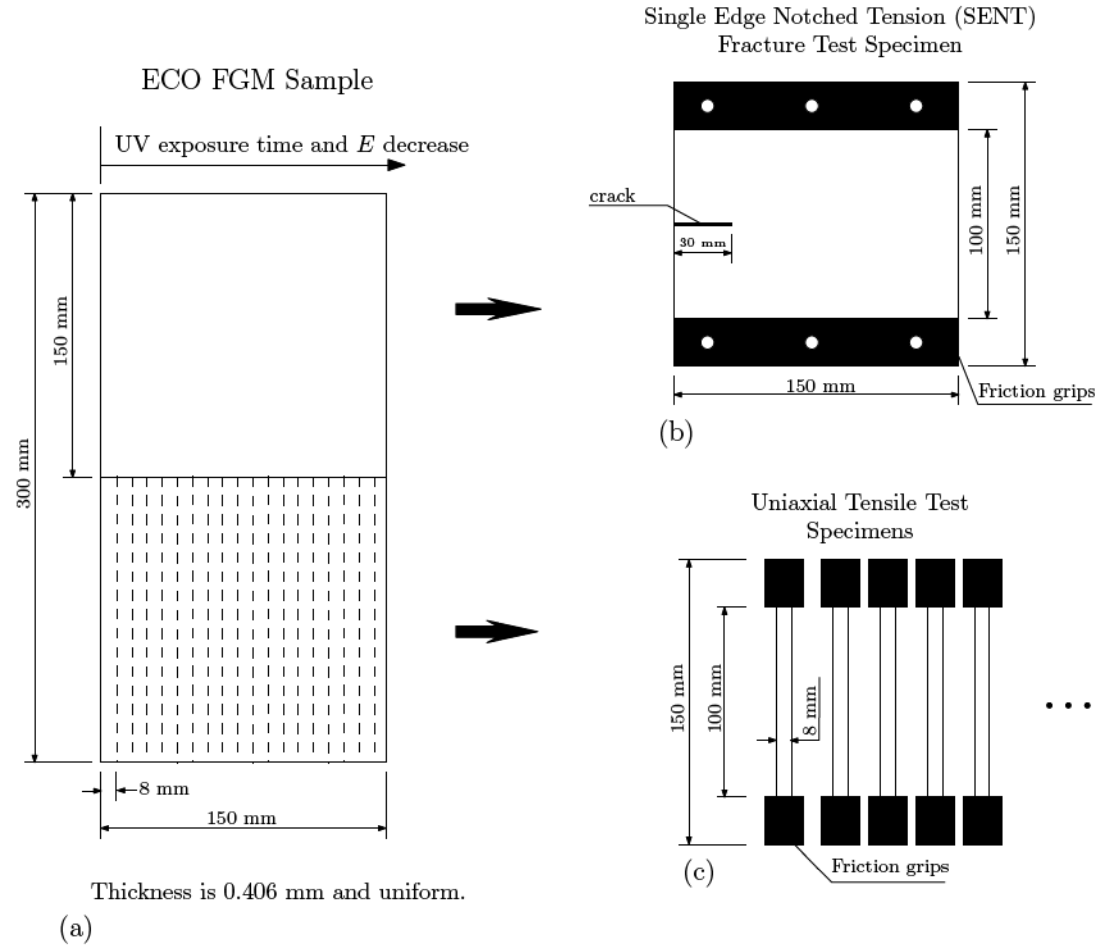

Figure 4.34. Geometry of (a) gradually UV irradiated FGM ECO sheet; (b) tensile and (c) fracture specimens obtained from this sheet [22, 23]

4.2.2.1. Power Hardening Plasticity. In this section, power hardening is assumed for the bulk plastic behavior of the material. GTN model parameters and power hardening exponent variations which results a good agreement between numerical and experimental stress-strain responses of uniaxial tension specimens, are obtained by trial and error. For less UV irradiated region (more ductile) of the material, numerical and experimental stress-strain responses deviate from each other since the material at this region does not exhibit a power hardening behavior. For this region, experimental failure strains are preferred to be captured numerically, and an agreement between strain energy (area under stress-strain curve) of numerical and experimental responses is watched out.

The resulting yield function coefficients and volume fraction of void nucleating particles are $q_1 = 6$, $q_2 = 1$, $q_3 = q_1^2 = 36$ and $f_n = 0.06$. They are kept constant along

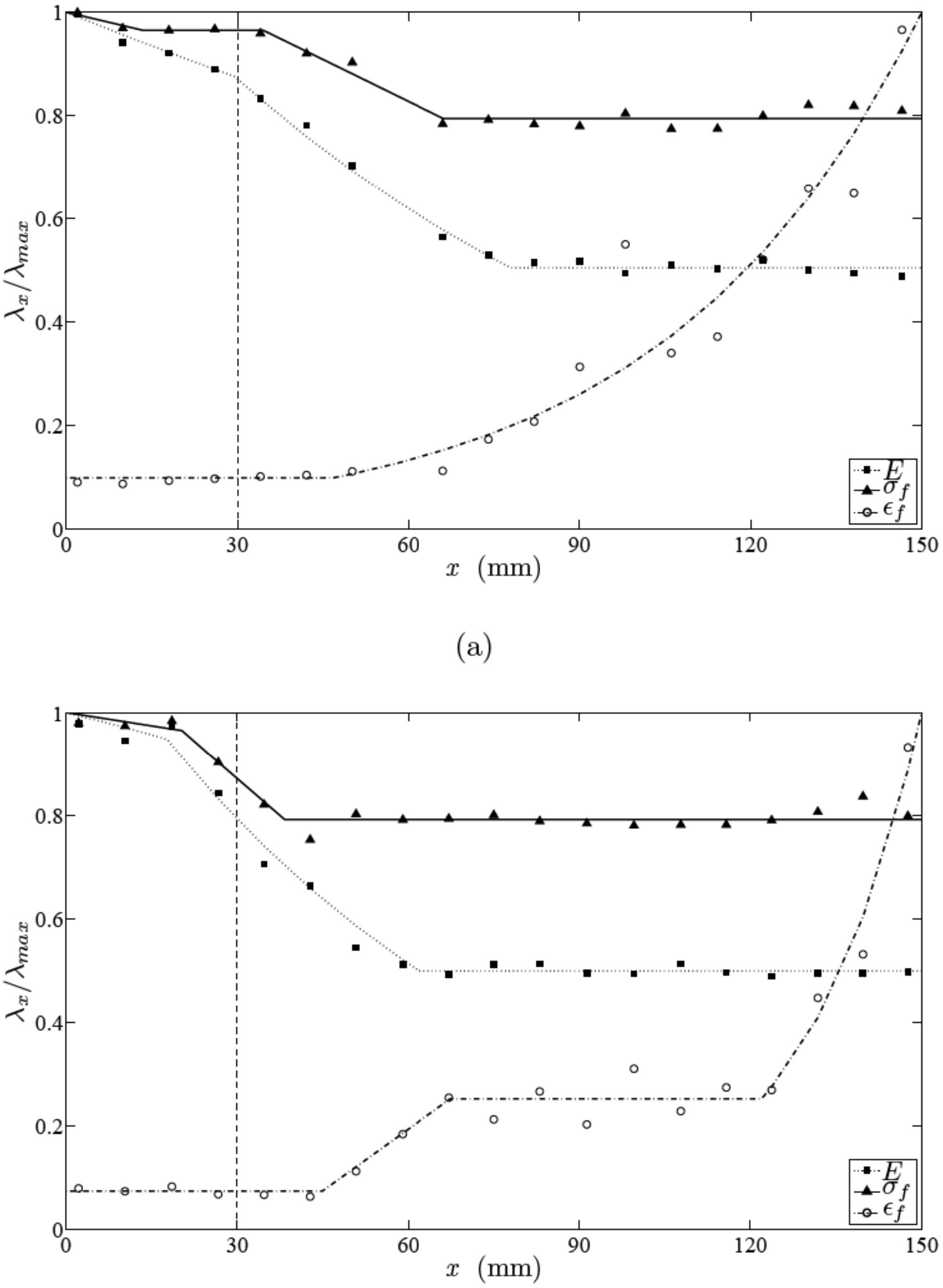

(a)

(b)

Figure 4.35. Spatial variation of normalized material properties along the material gradient direction of ECO (a) FGM I, (b) and FGM II SENT specimens. The dashed vertical lines mark the initial crack-tip location. The symbols represent the experimental data, and the curves correspond to their fit using piecewise exponential or linear functions [22, 23]

Table 4.12. Maximum values of material properties, λ_{max} in Figures 4.35 (a-b) for FGM I and II

	FGM I	FGM II
Max Young's modulus, E_{max} (MPa)	413	414
Max failure stress, $\sigma_{f_{max}}$ (MPa)	10.64	10.32
Max failure strain, $\epsilon_{f_{max}}$	0.91	0.98

the entire specimen. Mean nucleation strain ϵ_n and standard deviation s_n are varied along the width (gradation) of the specimen, and value of s_n is chosen to be quarter of the value of ϵ_n. The power hardening exponent and mean nucleation strain variations are plotted in Figure 4.36. The trends of mean nucleation strain, and power hardening exponent variations resemble to the failure strain, and failure stress variations of FGM II, respectively.

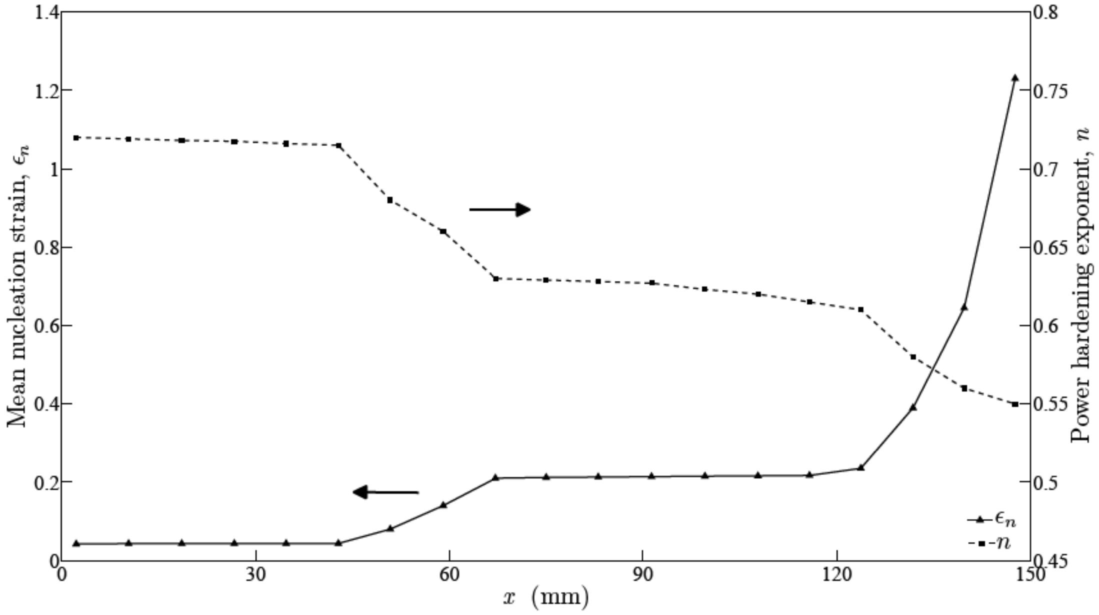

Figure 4.36. Spatial variation of mean nucleation strain and power hardening exponent for FGM II

The resulting stress - strain response using GTN model with the above mentioned failure parameters (dashed lines) are plotted in Figure 4.37 with the experimental data (solid lines). Failure stresses are overestimated since the GTN model parameters and power hardening exponents are enforced to capture experimental failure strains.

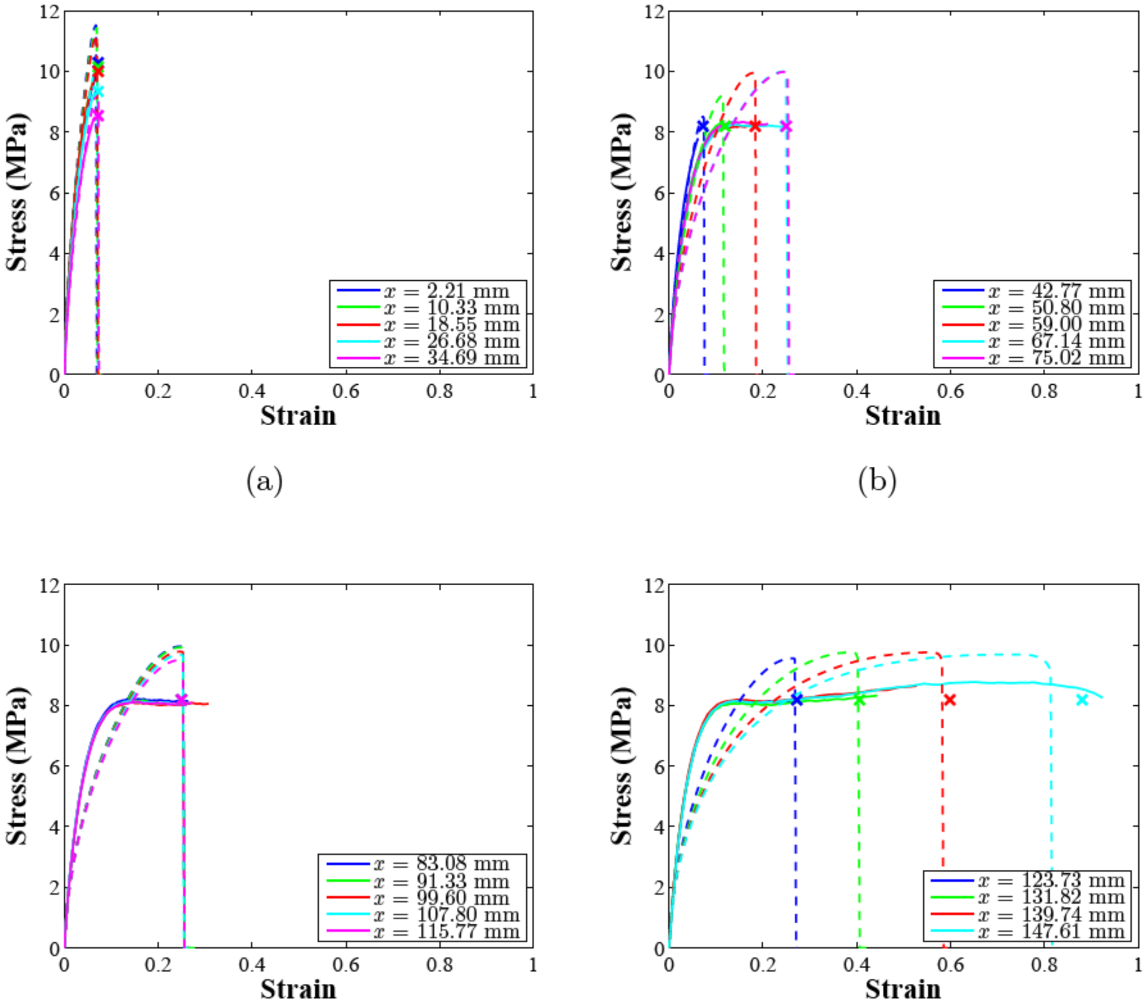

(a) (b)

(c) (d)

Figure 4.37. Stress - strain response of uniaxial tensile tests along FGM II ECO sheet. Solid lines are experimental data, dashed lines are GTN model results using GTN model parameter plotted in Figure 4.36, cross signs are fitted failure values

In - plane finite element mesh used for failure simulation of FGM II SENT specimen is shown in Figure 4.38. The mesh has 1625 linear hexahedral elements of type C3D8R with 3528 nodes, and it is same mesh used for homogeneously UV irradiated ECO SENT specimens. It is quarter of the entire specimen for 3-D finite element model. GTN model is imposed for a single layer of elements ahead the crack-tip similar to the computational cell method proposed by Xia and Shih [34, 35]. The length scale of application of the GTN model is taken to correspond to the craze half-size of the polymer, producing an in-plane mesh size of minimum element size 0.4 × 0.4 mm^2. This size is assumed to be the characteristic length scale for ECO which is also done for finite element analysis of homogeneous ECO specimens. Load vs load line displacement responses obtained numerically and experimentally for FGM II are plotted in Figure 4.39.

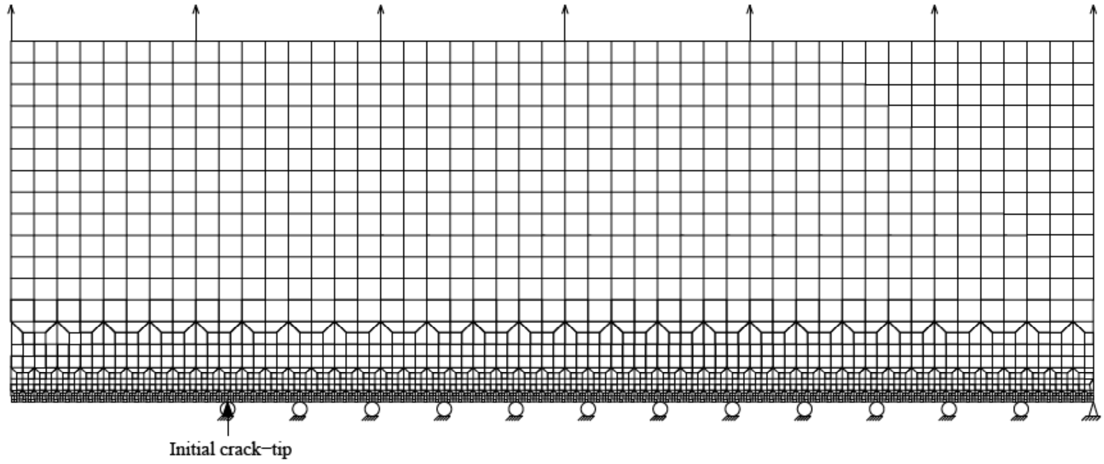

Figure 4.38. Finite element mesh for FGM ECO SENT fracture test specimen

Experimental and numerical responses exhibit similarity in shape, but the numerical load and displacement values are smaller than the ones for experiment as shown in Figure 4.39. Sensitivity analyses showed that load values increase as a result of increasing mean nucleation strain ϵ_n and increasing standard deviation s_n in failure simulations of SENT fracture specimens. Therefore, increasing mean nucleation strain ϵ_n and corresponding standard deviation s_n values is considered. FGM II SENT fracture specimen is re-simulated with increased nucleation parameters, and these parameters are plotted in Figure 4.40. One should note that standard deviation s_n is kept one fourth of mean nucleation strain values along the specimen. Power hardening exponent n variation is almost same as shown in Figure 4.36. Load and crack extension vs load line displacement responses of the FGM II ECO SENT specimen are plotted in Figure 4.41 using these parameters. A set of failure parameter variation along the specimen is obtained that shows a reasonable agreement with the experimental load

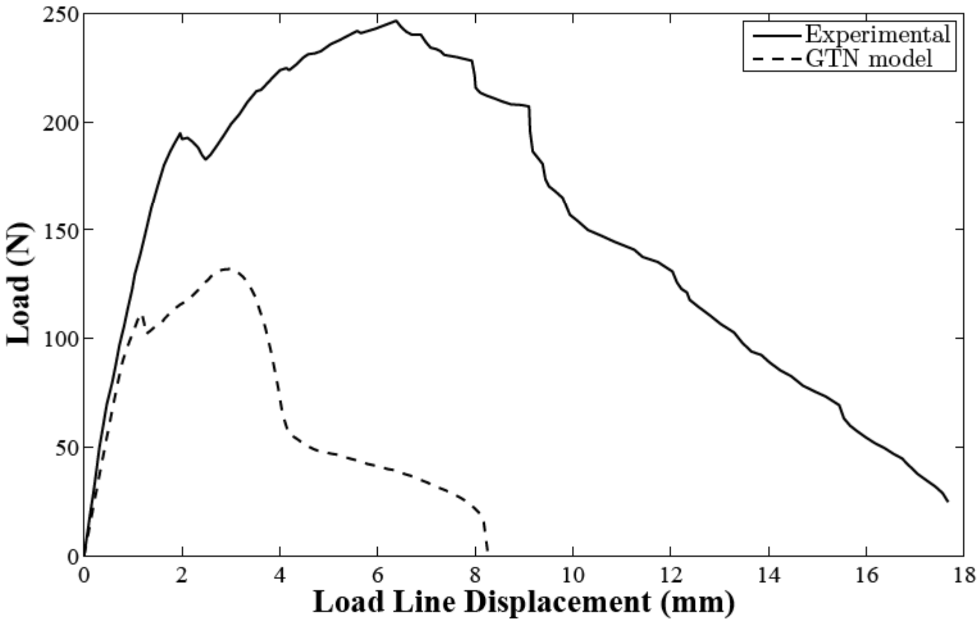

Figure 4.39. Experimental and numerical load vs load line displacement response of FGM II ECO SENT fracture test specimen using GTN model parameter plotted in Figure 4.36

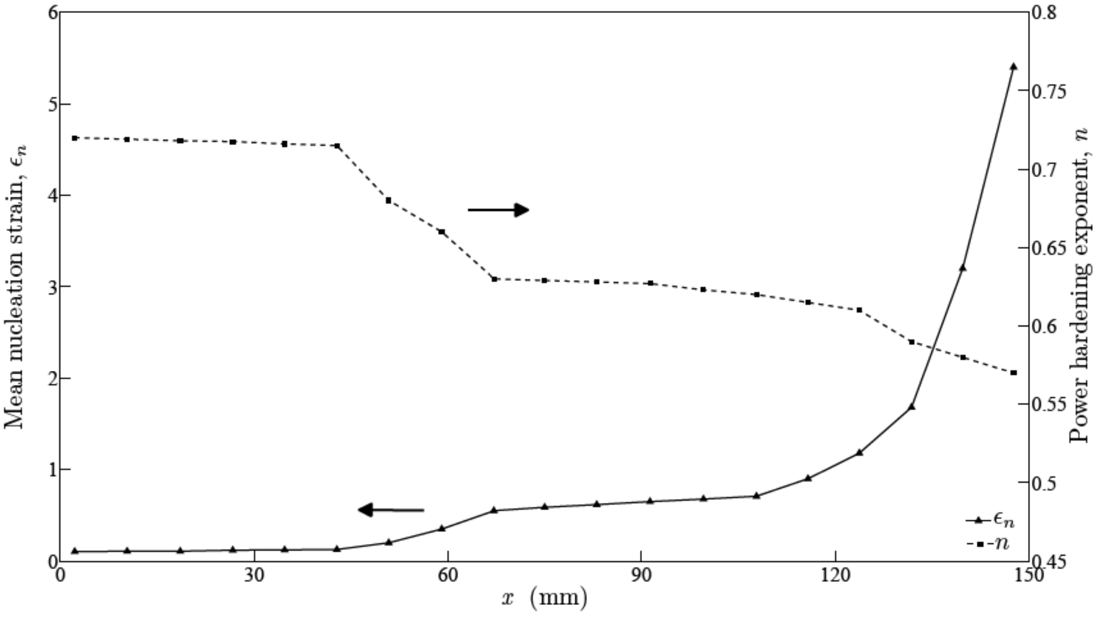

Figure 4.40. Spatial variation of increased mean nucleation strain and power hardening exponent for FGM II

and crack extension vs load line displacement. Stress-strain responses calculated using GTN model with this set of parameters are plotted in Figure 4.42, but experimental tensile stress-strain responses could not be captured numerically with those failure parameter variation using power hardening plasticity.

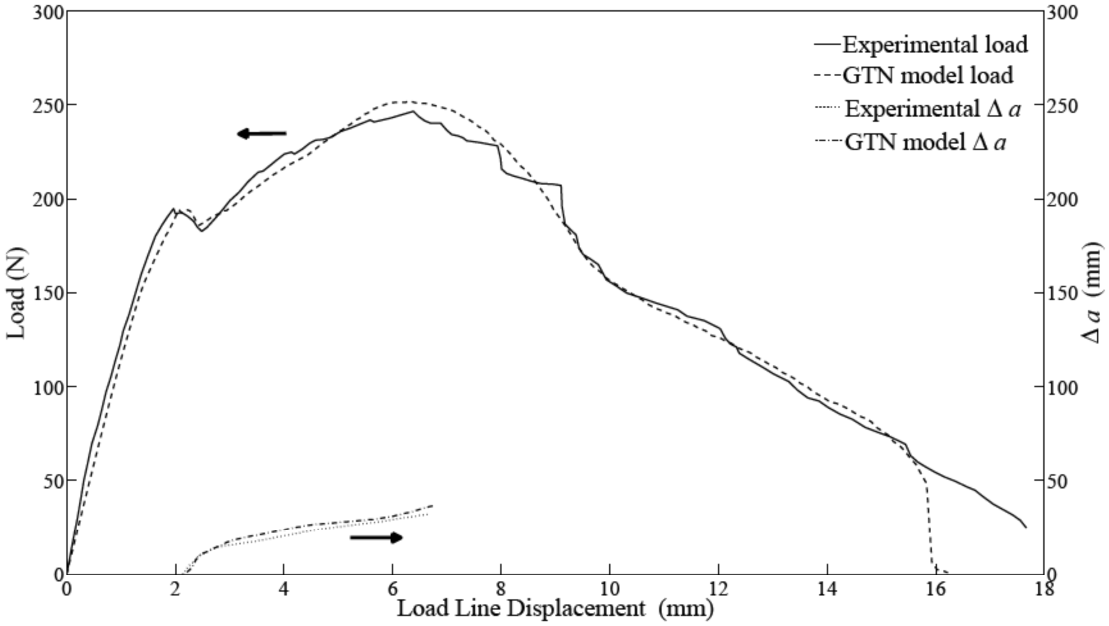

Figure 4.41. Experimental and numerical, load and crack extension vs load line displacement responses of FGM II ECO SENT fracture test specimen using GTN model parameter plotted in Figure 4.40

4.2.2.2. Experimental Plastic Data. Instead of power hardening law for the plastic response of the material, using the experimental tensile test data is considered as it is done for homogeneously UV irradiated ECOs. Bulk elastic and plastic material properties are taken from experimental results up to ultimate tensile strength, σ_{UTS}, where necking initiates. After σ_{UTS}, the bulk behavior stress value is kept constant at the ultimate value, as observed in the experiments until failure. Yield function coefficients and volume fraction of void nucleating particles are chosen to be $q_1 = 6$, $q_2 = 1$, $q_3 = q_1^2 = 36$ and $f_n = 0.06$ along the specimen as it was done in previous section. Mean nucleation strain ϵ_n and corresponding standard deviation s_n are varied along the width of the specimen, and value of s_n is one quarter of the value of ϵ_n. Figure 4.43 shows mean

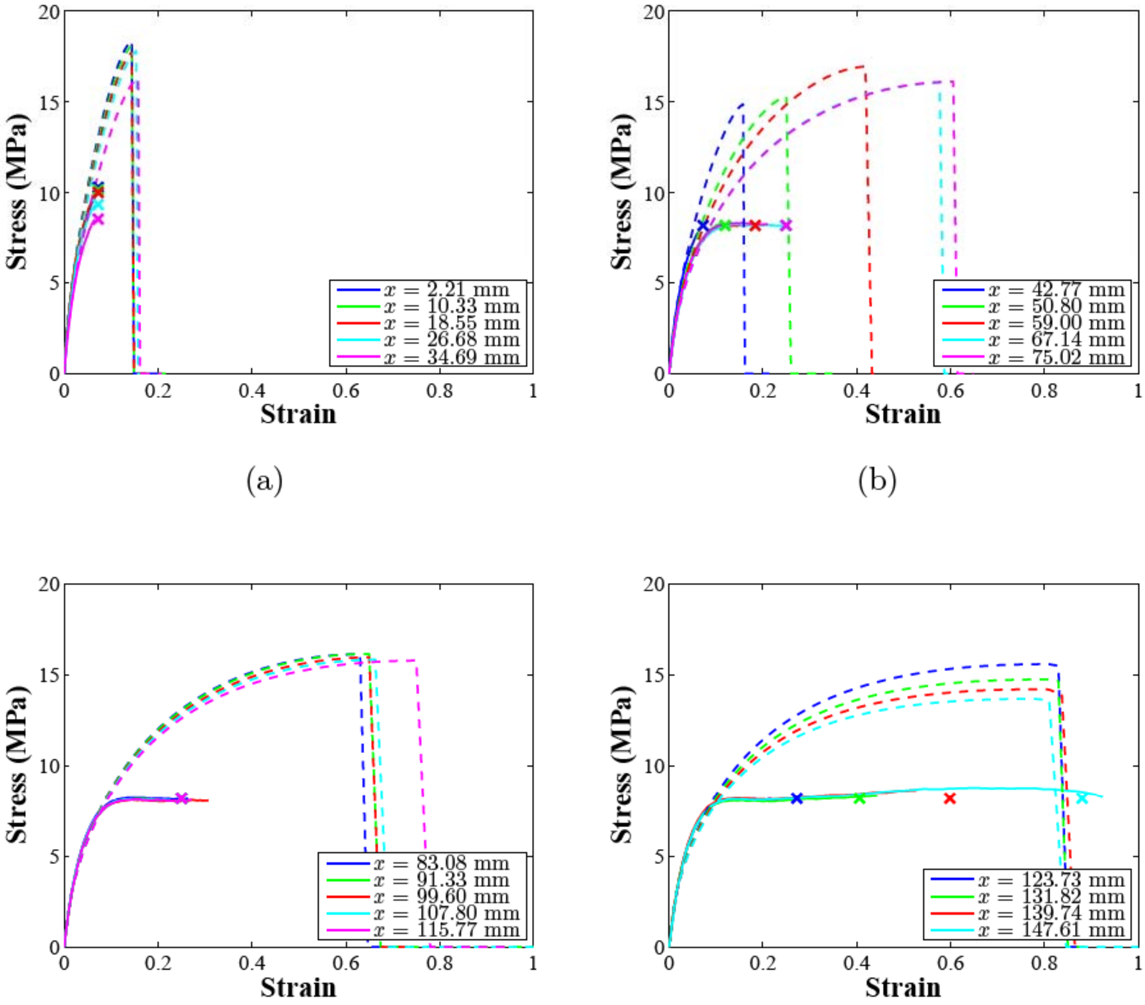

(a) (b)

(c) (d)

Figure 4.42. Stress - strain response of uniaxial tensile tests along FGM II ECO sheet. Solid lines are experimental data, dashed lines are GTN model results using GTN model parameter plotted in Figure 4.40, cross signs are fitted failure values

nucleation strain variation along the specimen. This is obtained by trial and error to capture stress-strain response of experimental uniaxial tensile tests data, and resulting numerical stress-strain responses are plotted in Figure 4.44. Experimental stress-strain response of the tensile tests is captured very well numerically using experimental data for plastic behavior of the constituents of the FGM in simulations.

Load and crack extension vs load line displacement response of FGM II SENT fracture specimen is simulated using the failure parameters and material properties obtained from experimental uniaxial tension tests data, and it is plotted in Figure

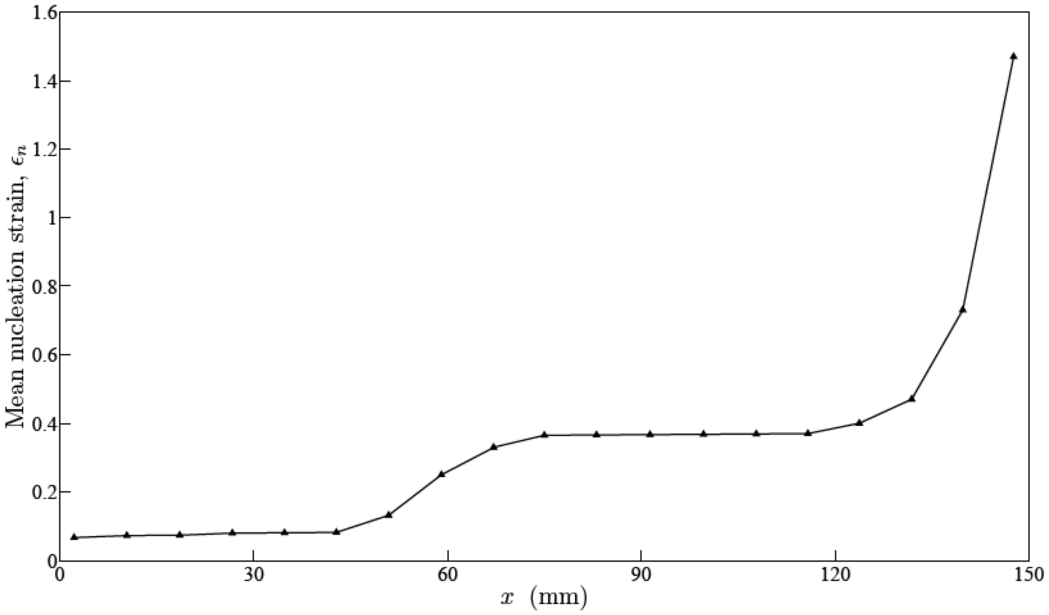

Figure 4.43. Spatial variation of mean nucleation strain for FGM II using experimental uniaxial tension tests data for elastic-plastic response

4.45. Trends of numerical and experimental results are similar, but the values are not agree as it was the case while using power hardening law.

Mean nucleation strain variation (also standard deviation s_n) is increased as shown in Figure 4.46, and the other GTN model parameters and elasto-plastic properties are kept same as which were obtained from experimental tension tests. Figure 4.47 shows that a better agreement can be achieved between experimental and numerical load and crack extension vs load line displacement responses of FGM II ECO SENT fracture specimen. Resulting uniaxial tensile test responses are plotted in Figure 4.48 using above mentioned GTN model parameters and material properties. Numerical failure stresses for uniaxial tensile test responses are well agree with the experimental ones. Predicted numerical failure strains are also in a reasonable agreement with experimental failure strains in ranges of x = [0 59] mm and x = [131 150] mm, but the numerical failure strains are overestimated with respect to the experimental ones in the range of x = [59 131] mm.

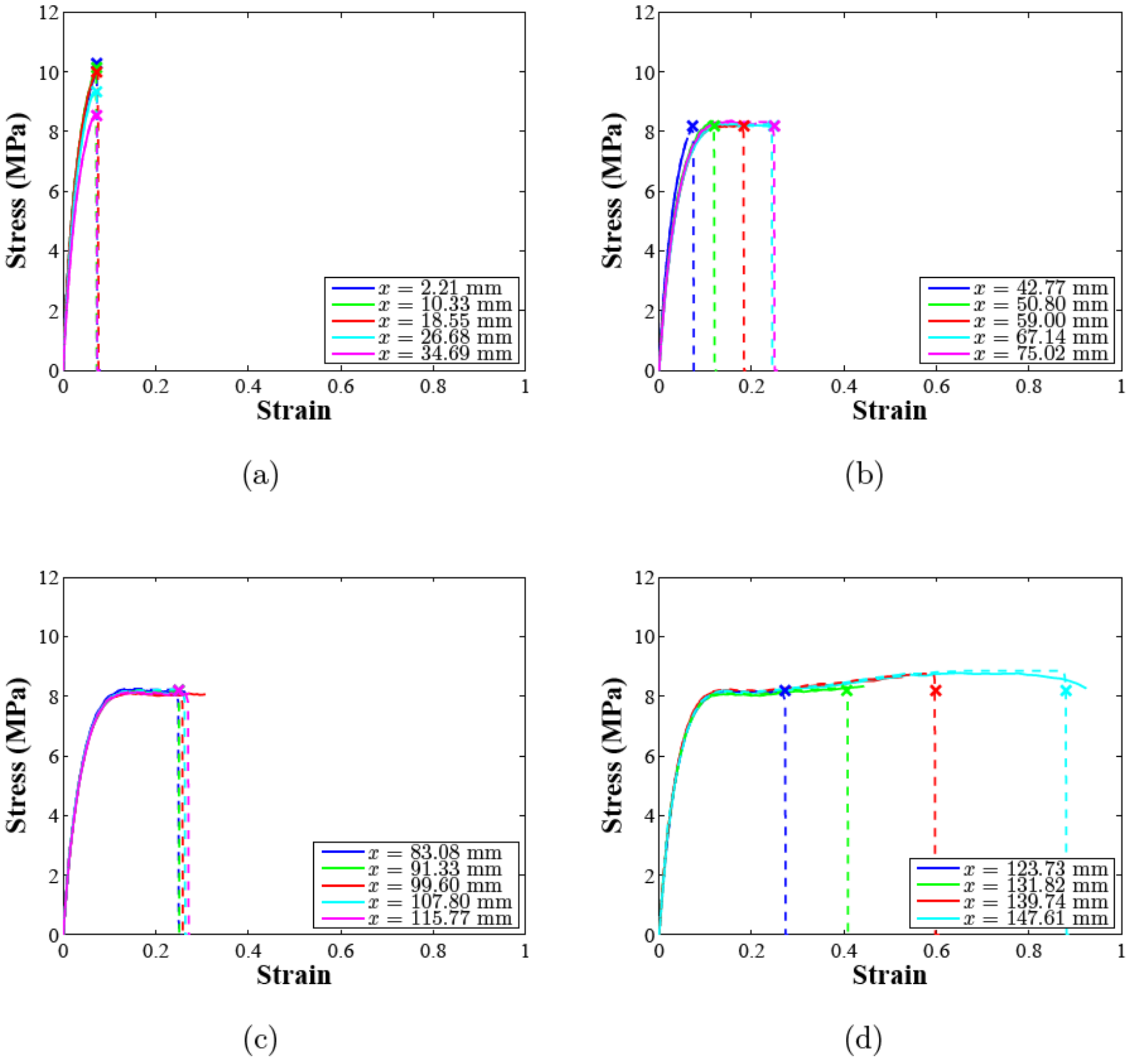

(a) (b)

(c) (d)

Figure 4.44. Stress - strain response of uniaxial tensile tests along FGM II ECO sheet. Solid lines are experimental data, dashed lines are GTN model results using ϵ_n plotted in Figure 4.43 and experimental uniaxial tension tests data for elastic-plastic response, cross signs are fitted failure values

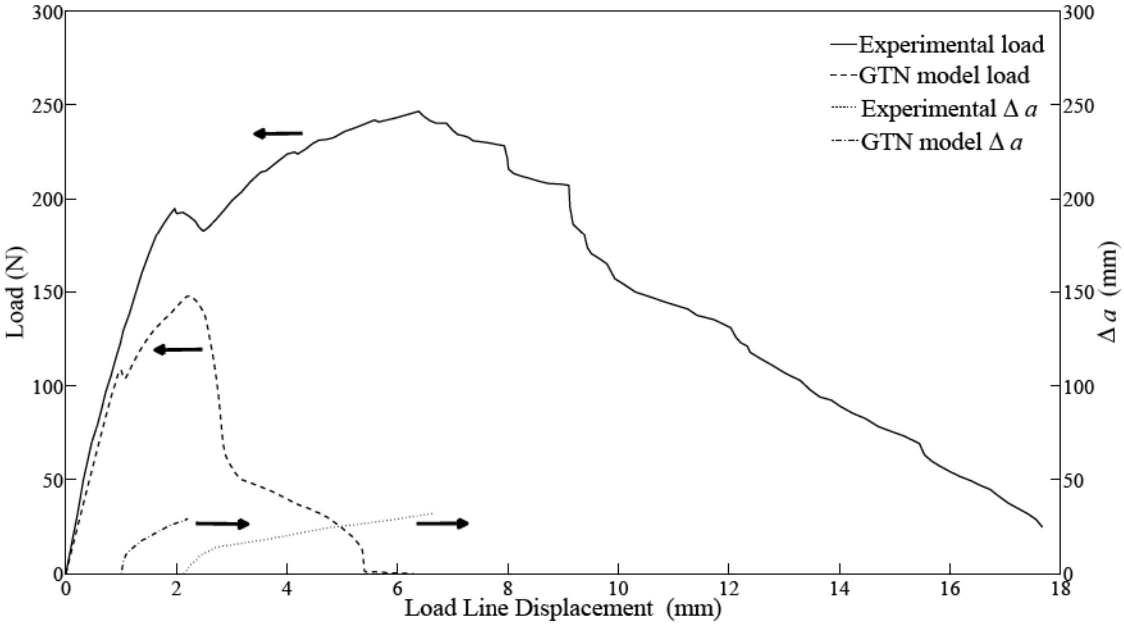

Figure 4.45. Experimental and numerical, load and crack extension vs load line displacement responses of FGM II ECO SENT fracture test specimen using ϵ_n plotted in Figure 4.43 and experimental uniaxial tension tests data for elastic-plastic response

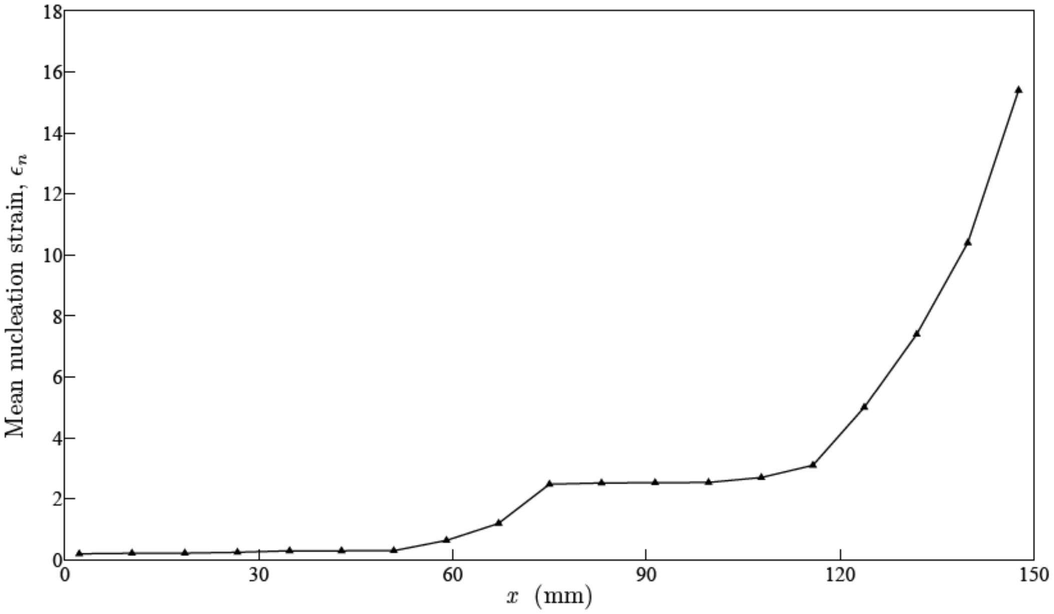

Figure 4.46. Spatial variation of increased mean nucleation strain for FGM II using experimental uniaxial tension tests data for elastic-plastic response

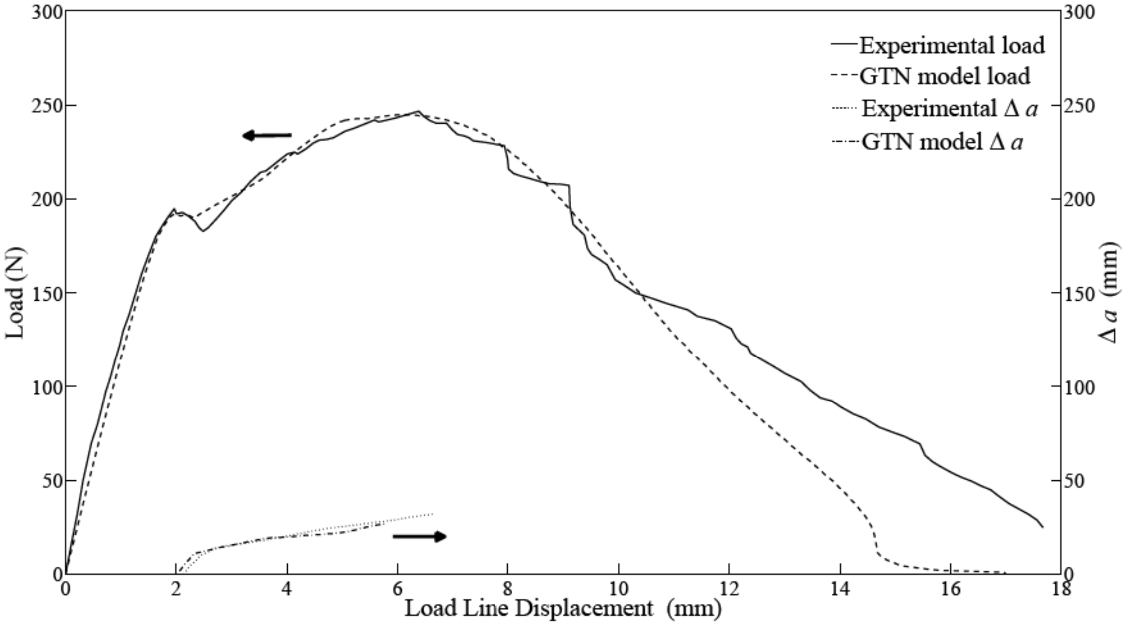

Figure 4.47. Experimental and numerical, load and crack extension vs load line displacement responses of FGM II ECO SENT fracture test specimen using increased ϵ_n values plotted in Figure 4.46 and experimental uniaxial tension tests data for elastic-plastic response

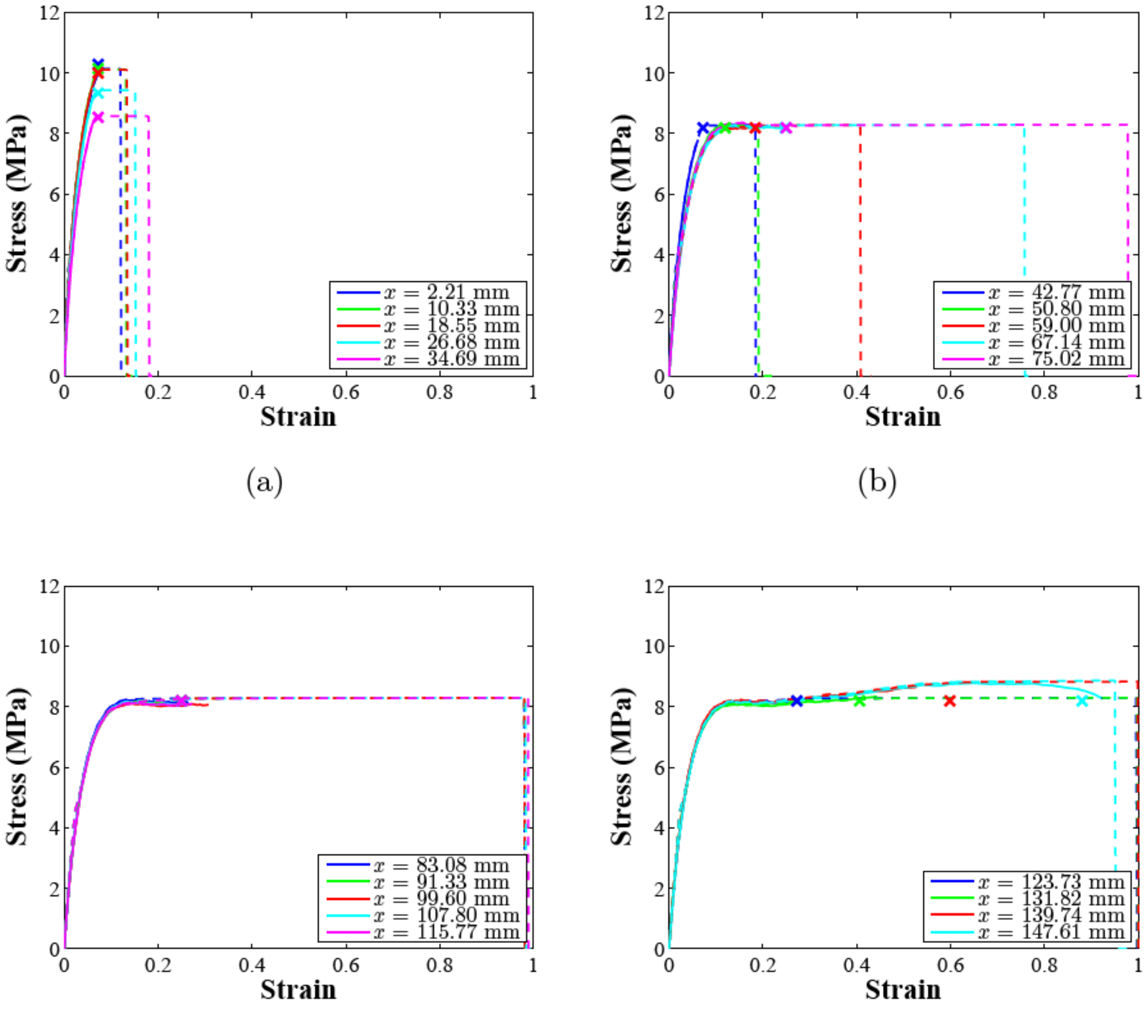

(a) (b)

(c) (d)

Figure 4.48. Stress - strain response of uniaxial tensile tests along FGM II ECO sheet. Solid lines are experimental data, dashed lines are GTN model results using increased ϵ_n values plotted in Figure 4.46 and experimental uniaxial tension tests data for elastic-plastic response, cross signs are fitted failure values

5. SUMMARY AND CONCLUSIONS

Functionally graded materials which possess continuous variation of material properties from one material point to another are a new kind of composite materials. They attracted attention of researchers because of their superiorities on other types of composites. Researches on failure of FGMs are limited. There are a few attempts to predict failure of FGMs using cohesive zone models. In this dissertation, one of the continuum damage models that is GTN model proposed by Gurson, Tvergaard and Needleman is investigated in detail and its implementation to failure of FGMs is studied.

GTN model consists of a pressure sensitive yield function and evolution laws for void volume function. This model was used for homogeneous materials. GTN model and its numerical implementation are investigated. For this purpose, the pressure sensitive yield functions for cylindrical and spherical voids are derived. Then, it is attempted to derive a closed form analytical yield function for a cylindrical void with a radially varying (power law variation) shear modulus, but it could not be achieved. Even it has been achieved, this yield function will be valid only for a specific material's property variation, and it will not be applicable to other FGMs. Therefore, numerical implementation of GTN model is considered. Abaqus that has a built-in GTN model module is chosen for simulating failure. Abaqus GTN model module is verified by comparing the Abaqus' results to the results of a failure of three point bending specimen from literature. GTN model parameters consists of (i) yield function coefficients (q_i), (ii) void volume fraction parameters (f_0, f_c, f_F), and (iii) nucleation parameters (ϵ_n, s_n, f_n). The effects of these parameters are investigated on stress-strain response of a uniaxial tension specimen. It is observed that the most sensitive parameter is yield function coefficients (q_i). When $q_2 = 1$ and $q_3 = q_1^2$ is chosen which was done in most of the studies in literature, the effect of q_1 on ultimate stress and failure strain is significant. The complete loss of stress carrying capacity occurs when $f{=}1/q_1$ for above mentioned q_2, q_3 assignment. Ultimate stress and failure strain decrease while the value of q_1 increases. This makes sense when inverse proportionality between q_1 and total failure void volume fraction is considered. Pressure sensitive yield function is plotted for different q_1 values for a constant void volume fraction f in Figure 5.1. In this figure, constant triaxial stress (ratio of hydrostatic stress and equivalent stress) curves are also included to observe the effect of triaxial stress on failure. It can be concluded that a material with a higher value of q_1 is more sensitive to failure for increasing triaxial stress, because the yield surface shrinks more rapidly with increasing q_1 value while triaxial stress is greater than 1. Void nucleation parameters ϵ_n, s_n and f_n also effect ultimate stress and failure strain. Increasing ϵ_n, s_n and decreasing f_n values result increasing failure strain, but results for s_n are not eye catching.

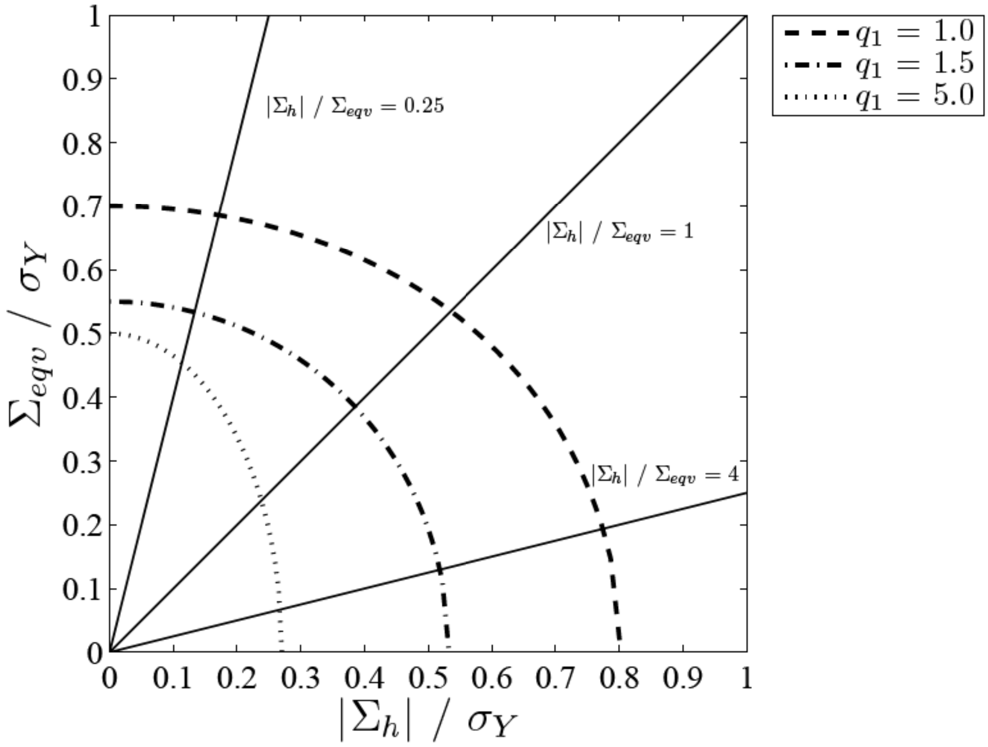

Figure 5.1. GTN yield function for different q_1 values where f=0.3

The most common problem encountered was mesh size dependency while using continuum damage mechanics (CDM) models such as GTN model. This problem is noticed in sections 3.4 and 4.1. In section 3.4, failure simulation obtained by mesh refinement resulted a bifurcating crack growth which is not realistic. In section 4.1, decreasing failure initiation loads are predicted as mesh size near the crack-tip decreases for pure titanium (Ti) and titanium monoboride / titanium (TiB / Ti) FGM single edge bending specimens. Mesh size is accepted as a material characteristic length scale.

Two numerical and experimental studies in literature are revisited for simulating failure for FGMs using GTN model. One of these studies is failure of a pure titanium (Ti) and a titanium monoboride / titanium (TiB / Ti) functionally graded material (FGM) single edge notched bending specimens investigated by Paulino *et al.* [41] and Jin *et al.* [17, 18], respectively. The other one is fracture of homogeneously and gradually ultraviolet irradiated polyethylene carbon monoxide co-polymer (a polymer based laboratory scaled FGM) uniaxial and single edge notched tension specimens investigated by Abanto-Beuno [23], Abanto-Bueno and Lambros [47] and Kandula *et al.* [22].

For the failure study of pure Ti and TiB / Ti FGM specimens, first GTN model parameters for pure Ti are determined from experimental stress-strain response of uniaxial tension specimen by trial and error. Non-uniqueness of the GTN model parameters which was first emphasized by Zhang [37] is observed while obtaining these parameters for pure Ti. Different set of parameters yield almost indistinguishable stress-strain responses. Therefore, it is required more experimental data obtained from specimens under different stress triaxialities to determine GTN model parameters more accurately for a material. One of these parameters set is used for failure simulation of pure Ti single edge notched bending specimen. Predicted failure initiation loads are sensitive to mesh size as mentioned before, but a good agreement is achieved between numerical and experimental results with a proper choice of GTN model parameters of set and mesh size. Elastic-plastic response of the constituents in TiB / Ti FGM are not available experimentally, so an extended form of original Tamura - Totmota - Ozawa (TTO) model which is based on rule of mixtures is used to describe the elastic-plastic response of the constituents. An excellent agreement is achieved between analytical response and numerical response which is obtained using Abaqus for the extended TTO elastic-plastic model. Yield function coefficient q_1 is varied in a manner that is higher for more brittle region to result a lower failure strain, and the void nucleation parameters ϵ_n, s_n and f_n obtained for pure Ti are kept constant for failure simulation of TiB / Ti FGM single edge bending specimen. Predicted failure initiation loads are also sensitive to mesh size. GTN model results compared to the ones obtained by using cohesive zone model in literature, and results are quite off from each other. On the other hand, results obtained using cohesive zone model in literature starts to deviate from the results of stationary crack without cohesive zone model which is given in the same research paper while the loads are very small. It is believed that this is not physically admissible. Detailed experimental results for this fracture problem are not published in literature, therefore studying with TiB / Ti FGM specimens is ceased.

Another FGM specimen which was manufactured using a novel technique by Lambros *et al.* [46] is preferred for the investigation of failure using GTN model because of the accessibility of experimental results given by Abanto-Bueno [23]. The experiments showed a ductile-to-brittle transition occurring with increasing amounts of ultraviolet (UV) light irradiation of a photodegradable 1% wt carbon monoxide polyethylene co-polymer (ECO). For low amounts of irradiation (less than 10 hours) shear yielding was the dominant failure mode, as is typical of ductile polymers. For higher amounts of irradiation times brittle like failure mechanism was observed locally, although globally significant ductility was still maintained. Before studying failure of FGM ECO specimens, the applicability of GTN model for failure of homogeneously UV irradiated ECO polymers is investigated. The characteristic length scale of application of the GTN model is taken to correspond to the craze half-size of the polymer, producing an in-plane mesh size of minimum element size 0.4×0.4 mm^2. Six different optimization calculations are performed; *i*) the tensile specimen, *ii*) the fracture specimen, and *iii*) the tensile and fracture specimens together using *two* different objective functions to determine GTN model parameters, for each different UV irradiation time (5, 42 and 130 h.), corresponding to varying amounts of ductility. Numerical results of tensile test specimens are in good agreement with experimental ones. Results obtained using different objective functions overlap and do not exhibit a significant difference except at perhaps near the failure point. However, this is not the case for the fracture experiments, although the results of different minimizations agree well up to a certain load point. A scheme where *both* the uniaxial tension and the SENT fracture data are simultaneously used in the GTN parameter determination is proposed. In the combined cases numerical results of ultimate load overshoot the experimental ones by approximately 10%, and the corresponding displacements are predicted well, although with less accuracy. In general the shapes of the response curves are also similar to the experimental ones for fracture specimens. Regarding the specific GTN parameters obtained, as the UV irradiation time is increased, f_c and f_F values generally decrease. This is reasonable since the increase in brittleness of ECO is consistent with increasing UV irradiation time. In the literature, the GTN model has been widely used to study failure of metals, e.g., steel, aluminum, copper [26, 28, 32, 33, 36, 38, 67, 69–72, 75, 76]. From such a wide variety of studies, the GTN model parameters for metals can be seen to lay in the ranges:

$$\begin{gathered} 1.1 \leq q_1 \leq 1.9, \quad 0.8 \leq q_2 \leq 1, \\ 0.002 \leq f_c \leq 0.17, \quad 0.15 \leq f_F \leq 0.25. \end{gathered} \tag{5.1}$$

In this study these parameters are obtained as:

$$\begin{gathered} 2.919 \leq q_1 \leq 3.280, \quad 0.539 \leq q_2 \leq 1.109, \\ 0.152 \leq f_c \leq 0.224, \quad 0.163 \leq f_F \leq 0.328. \end{gathered} \tag{5.2}$$

The difference in q_1's between the polymer and metals is striking, although for the remaining values this is less so. A higher value for q_1 has been calculated than metals. This indicates that ECO is more sensitive to stress triaxiality. A comparable q_1 value of 2.6, was obtained from true stress-strain and volume variation data for a rubber toughened PMMA tensile specimen by [52] who used a viscoplastic-damage constitutive model. In conclusion it is shown that the GTN model is promising for damage simulations of polymeric materials.

The outcomes of homogeneously UV irradiated ECO specimens' simulations were encouraging to use the GTN model for failure simulations of gradually UV irradiated ECO FGM specimens. Parameter determination technique that is proposed for homogeneous ECO is not carried out for ECO FGM specimens since the current available computational power is not sufficient to solve such a problem in a reasonable time. GTN models parameters are determined by trial and error. First, the GTN model parameters are predicted comparing the experimental uniaxial tension test data with the numerical results. Some of the GTN model parameters are kept constant while void nucleation parameters ϵ_n and s_n are varied through the graded material. It is observed that plastic behavior of the ECO does not obey power hardening law, especially for the more ductile (less UV irradiated) zone. The failure of ECO FGM SENT specimen is simulated using these parameters obtained from tension tests. Load and crack extension vs load line displacement responses of these simulations are compared to the experimental ones. Similarity between the trends of these results are promising. Sensitivity analyses showed that increasing mean nucleation strain yields increasing load values for SENT fracture specimen. A reasonable agreement between numerical and experimental responses of uniaxial tension and SENT fracture tests is achieved with a selection of proper GTN model parameters. It is believed that this agreement between numerical and experimental results can be improved using the parameters determination technique that is proposed for for homogeneous ECO. Therefore, further studies are necessary to improve the agreement between numerical and experimental results.

In conclusion, GTN model capabilities are well understood, and it is shown that GTN model is promising for failure simulations of FGMs with selection of proper GTN model parameters.

APPENDIX A: PRANDTL-REUSS STRESS STRAIN RELATION

The Lévy-Mises equations, as they are known, may be expressed in the form

$$\frac{\mathrm{d}\epsilon_{xx}}{\sigma'_{xx}} = \frac{\mathrm{d}\epsilon_{yy}}{\sigma'_{yy}} = \frac{\mathrm{d}\epsilon_{zz}}{\sigma'_{zz}} = \frac{\mathrm{d}\gamma_{yz}}{\sigma_{yz}} = \frac{\mathrm{d}\gamma_{xz}}{\sigma_{xz}} = \frac{\mathrm{d}\gamma_{xy}}{\sigma_{xy}} \tag{A.1}$$

or, more compactly, as

$$\mathrm{d}\epsilon_{ij} = \sigma'_{ij}\mathrm{d}\lambda \tag{A.2}$$

where where σ'_{ij} is deviatoric stress tensor and $\mathrm{d}\lambda$ is a scalar factor of proportionality which varies throughout the deformation history. Since Lévy and von Mises used the total strain increment, and not the plastic strain increment, the equations are strictly applicable only to a fictitious material in which the elastic strain are zero. Accordingly Young's modulus must be regarded as infinitely large, the material remaining rigid when unloaded. The extension of the Lévy-Mises equations to allow for the elastic component of the strain was carried out by Prandtl for the plane problem, and in complete generality by Reuss. Reuss assumed that

$$\mathrm{d}\epsilon^p_{ij} = \sigma'_{ij}\mathrm{d}\lambda \tag{A.3}$$

where ϵ^p_{ij} is plastic strain. Hill [77] showed that increment of plastic work per unit volume for the von Mises yield criterion is

$$\mathrm{d}W^p = \sigma'_{ij}\mathrm{d}\epsilon^p_{ij} = \sigma_Y \mathrm{d}\epsilon^p_{eqv} \tag{A.4}$$

where

$$\sigma_Y = \sqrt{\frac{3}{2}\sigma'_{ij}\sigma'_{ij}} \quad \text{(equivalent stress)} \tag{A.5a}$$

$$\mathrm{d}\epsilon^p_{eqv} = \sqrt{\frac{2}{3}\mathrm{d}\epsilon^p_{ij}\mathrm{d}\epsilon^p_{ij}} \quad \text{(equivalent plastic strain increment)} \tag{A.5b}$$

Substituting Equation A.3 into Equation A.4, gives

$$\begin{aligned} \mathrm{d}\lambda &= \frac{\sigma_Y \mathrm{d}\epsilon^p_{eqv}}{\sigma'_{ij}\sigma'_{ij}} \\ &= \frac{3}{2}\frac{\mathrm{d}\epsilon^p_{eqv}}{\sigma_Y} \end{aligned} \tag{A.6}$$

Using Equations A.5b and A.6, Prandtl-Reuss relation Equation A.3 results

$$\begin{aligned} \sigma'_{ij} &= \frac{2}{3}\frac{\sigma_Y}{\mathrm{d}\epsilon^p_{eqv}}\mathrm{d}\epsilon^p_{ij} \\ &= \sqrt{\frac{2}{3}}\frac{\sigma_Y \dot{\epsilon}^p_{ij}}{(\dot{\epsilon}^p_{kl}\dot{\epsilon}^p_{kl})^{1/2}} \end{aligned} \tag{A.7}$$

where superimposed dot indicates the time derivative and $\dot{\epsilon}$ is strain rate.

APPENDIX B: INTEGRATION WITH RESPECT TO Ω

By definition

$$\mu = \frac{\dot{E}'_{rr}}{\sqrt{\frac{2}{3}\dot{E}'_{kl}\dot{E}'_{kl}}} \tag{B.1}$$

After coordinate transformation, $\dot{E}'_{rr} = C_{ri}C_{rj}\dot{E}'_{ij}$. On the unit sphere, $C_{ri} = n_i = x_i$. Therefore,

$$\mu = \frac{\dot{E}'_{ij}n_i n_j}{\sqrt{\frac{2}{3}\dot{E}'_{kl}\dot{E}'_{kl}}} \tag{B.2}$$

The Gauss theorem states that

$$\int_{\Omega} n_i F_j d\Omega = \int_V \frac{\partial}{\partial x_i}(F_j)dV \tag{B.3}$$

v is the volume of the unit sphere, x_i are components of cartesian coordinates and F_j are the cartesian components of any vector. The following calculations are self explanatory.

$$\int_{\Omega} d\Omega = \int_0^{2\pi}\int_0^{\pi}\sin(\phi)d\phi d\theta = 4\pi \tag{B.4}$$

$$\begin{aligned}\int_{\Omega}\mu d\Omega &= \frac{\dot{E}'_{ij}}{\sqrt{\frac{2}{3}\dot{E}'_{kl}\dot{E}'_{kl}}}\int_{\Omega} n_i x_j d\Omega = \frac{\dot{E}'_{ij}}{\sqrt{\frac{2}{3}\dot{E}'_{kl}\dot{E}'_{kl}}}\int_V \frac{\partial x_j}{\partial x_i}dV \\ &= \frac{\dot{E}'_{ij}\delta_{ij}}{\sqrt{\frac{2}{3}\dot{E}'_{kl}\dot{E}'_{kl}}} = 0 \end{aligned} \tag{B.5}$$

$$\begin{aligned}
\int_\Omega \mu^2 d\Omega &= \frac{3\dot{E}'_{ij}\dot{E}'_{mn}}{2\dot{E}'_{kl}\dot{E}'_{kl}} \int_\Omega n_i x_j x_m x_n d\Omega = \frac{3\dot{E}'_{ij}\dot{E}'_{mn}}{2\dot{E}'_{kl}\dot{E}'_{kl}} \int_V \frac{\partial}{\partial x_i}(x_j x_m x_n) dV \\
&= \frac{3\dot{E}'_{ij}\dot{E}'_{mn}}{2\dot{E}'_{kl}\dot{E}'_{kl}} \int_V [\delta_{ij} x_m x_n + \delta_{im} x_j x_n + \delta_{in} x_j x_m] dV \\
&= \frac{3\dot{E}'_{pq}\dot{E}'_{pr}}{\dot{E}'_{kl}\dot{E}'_{kl}} \int_V x_q x_r dV = \frac{\dot{E}'_{pq}\dot{E}'_{pr}}{\dot{E}'_{kl}\dot{E}'_{kl}} \delta_{qr} \int_V (x_1^2 + x_2^2 + x_3^2) dV \\
&= \int_V r^2 dV = \int_0^{2\pi}\int_0^{\pi}\int_0^1 r^4 \sin(\phi) dr d\phi d\theta = \frac{4}{5}\pi \qquad \text{(B.6)}
\end{aligned}$$

REFERENCES

1. Delale, F. and F. Erdogan, “The Crack Problem for a Nonhomogeneous Plane”, *Journal of Applied Mechanics-Transactions of the ASME*, Vol. 50 (3), pp. 609-614, 1983.

2. Eischen, J. W., “Fracture of Nonhomogeneous Materials”, *International Journal of Fracture*, Vol. 34 (1), pp. 3-22, 1987.

3. Erdogan, F., “Fracture Mechanics of Functionally Graded Materials”, *Composites Engineering*, Vol. 5 (7), pp. 753-770, 1995.

4. Erdogan, F. and B. H. Wu, “The Surface Crack Problem for a Plate with Functionally Graded Properties”, *Journal of Applied Mechanics-Transactions of the ASME*, Vol. 64 (3), pp. 449-456, 1997.

5. Anlas, G., M. H. Santare and J. Lambros, “Numerical Calculation of Stress Intensity Factors in Functionally Graded Materials”, *International Journal of Fracture*, Vol. 104, pp. 131-143, 2000.

6. Kim, J. H. and G. H. Paulino, “Finite Element Evaluation of Mixed Mode Stress Intensity Factors in Functionally Graded Materials”, *International Journal for Numerical Methods in Engineering*, Vol. 53 (8), pp. 1903-1935, 2002.

7. Gu, P. and R. J. Asaro, “Crack Deflection in Functionally Graded Materials”, *International Journal of Solids and Structures*, Vol. 34, pp. 3085-3098, 1997.

8. Becker, T. L. Jr., R. M. Cannon and R. O. Ritchie, “Finite Crack Kinking and T-Stresses in Functionally Graded Materials”, *International Journal of Solids and Structures*, Vol. 38, pp. 5545-5563, 2001.

9. Kim, J. H. and G. H. Paulino, “T-Stress, Mixed-Mode Stress Intensity Factors, and

Crack Initiation Angles in Functionally Graded Materials: A Unified Approach Using the Interaction Integral Method", *Computer Methods in Applied Mechanics and Engineering*, Vol. 192 (11-12), pp. 1463-1494, 2003.

10. Abanto-Bueno, J. and J. Lambros, "An Experimental Study of Mixed Mode Crack Initiation and Growth in Functionally Graded Materials", *Experimental Mechanics*, Vol. 46 (2), pp. 179-196, 2006.

11. Oral, A., J. Lambros and A. Gunay, "Crack Initiation in Functionally Graded Materials Under Mixed Mode Loading: Experiments and Simulations", *Journal of Applied Mechanics - Transactions of the ASME*, Vol. 75, pp. 051110-1-8, 2008.

12. Barenblatt, G. I., "Equilibrium Cracks Formed on a Brittle Fracture", *Doklady Akademii Nauk SSSR*, Vol. 127 (1), pp. 47-50, 1959.

13. Barenblatt, G. I., "The Mathematical Theory of Equilibrium Cracks in Brittle Materials", *Advances in Applied Mechanics*, Vol. 7, pp. 55-129, 1962.

14. Dugdale, D. S., "Yielding of Steel Sheets Containing Slits", *Journal of the Mechanics and Physics of Solids*, Vol. 8 (2), pp. 100-104, 1960.

15. van den Bosch, M. J., P. J. G. Schreurs and M. G. D. Geers, "An Improved Description of the Exponential Xu and Needleman Cohesive Zone Law for Mixed-Mode Decohesion", *Engineering Fracture Mechanics*, Vol. 73, pp. 1220-1234, 2006.

16. Tvergaard, V., "Theoretical Investigation of the Effect of Plasticity on Crack Growth along a Functionally Graded Region between Dissimilar Elastic-Plastic Solids", *Engineering Fracture Mechanics*, Vol. 69 (14-16), pp. 1635-1645, 2002.

17. Jin, Z. H., G. H. Paulino and R. H. Dodds, "Finite Element Investigation of Quasi-Static Crack Growth in Functionally Graded Materials Using a Novel Cohesive Zone Fracture Model", *Journal of Applied Mechanics - Transactions of the ASME*, Vol. 69 (3) pp. 370-379, 2002.

18. Jin, Z. H., G. H. Paulino and R. H. Dodds, “Cohesive Fracture Modeling of Elastic-Plastic Crack Growth in Functionally Graded Materials”, *Engineering Fracture Mechanics*, Vol. 70 (14), pp. 1885-1912, 2003.

19. Wang, Z. Q. and T. Nakamura, “Simulations of Crack Propagation in Elastic-Plastic Graded Materials”, *Mechanics of Materials*, Vol. 36 (7), pp. 601-622, 2004.

20. Zhang, Z. Y. J. and G. H. Paulino, “Cohesive Zone Modeling of Dynamic Failure in Homogeneous and Functionally Graded Materials”, *International Journal of Plasticity*, Vol. 21 (6), pp. 1195-1254, 2005.

21. Kandula, S. S. V., J. Abanto-Bueno, P. H. Geubelle and J. Lambros, “Cohesive Modeling of Dynamic Fracture in Functionally Graded Materials”, *International Journal of Fracture*, Vol. 132 (3), pp. 275-296, 2005.

22. Kandula, S. S. V., J. Abanto-Bueno, J. Lambros and P. H. Geubelle, “Cohesive Modeling of Quasi-Static Fracture in Functionally Graded Materials ”, *Journal of Applied Mechanics - Transactions of the ASME*,Vol. 73, pp. 783-791, 2006.

23. Abanto-Bueno, J., *Fracture of a Model Functionally Graded Material Manufactured From a Photo-Sensitive Polyethylene*, Ph.D. Thesis, University of Illinois at Urbana-Champaign, 2004.

24. Gurson, A. L., *Plastic Flow and Fracture Behavior of Ductile Materials Incorporating Void Nucleation, Growth and Interaction*, Ph.D. Dissertation, Brown University, 1975.

25. Gurson, A. L., “Continuum Theory of Ductile Rupture by Void Nucleation and Growth: Part I - Yield Criteria and Flow Rules for Porous Ductile Media”, *Journal of Engineering Materials and Technology - Transactions of the ASME*, Vol. 99 (1), pp. 2-15, 1977.

26. Tvergaard, V., “Influence of Voids on Shear Band Instabilities under Plane Strain

Conditions", *International Journal of Fracture*, Vol. 17 (4), pp. 389-407, 1981.

27. Tvergaard, V., "Influence of Void Nucleation on Ductile Shear Fracture at a Free Surface", *Journal of the Mechanics and Physics of Solids*, Vol. 30 (6), pp. 399-425, 1982.

28. Tvergaard, V. and A. Needleman, "Analysis of the Cup-Cone Fracture in a Round Tensile Bar", *Acta Metallurgica*, Vol. 32 (1), pp. 157-169, 1984.

29. Aoki, S., K. Kishimoto, A. Takeya and M. Sakata, "Effects of Microvoids on crack Blunting and Initiation in Ductile Materials", *International Journal of Fracture*, Vol. 24, pp. 267-278, 1984.

30. Aravas, N. and R. M. Mcmeeking, "Microvoid Growth and Failure in the Ligament between a Hole and a Blunt Crack Tip", *International Journal of Fracture*, Vol. 29, pp. 21-38, 1985.

31. Aravas, N., "On the Numerical Integration of a Class of Pressure-Dependent Plasticity Models", *International Journal for Numerical Methods in Engineering*, Vol. 24, pp. 1395-1416, 1987.

32. Sun, D.Z., D., Siegle, B., Voss and W. Schmitt, "Application of Local Damage Models to the Numerical Analysis of Ductile Rupture", *Fatigue & Fracture of Engineering Materials & Structures*, Vol. 12(3), pp. 201-212, 1989.

33. Narasimhan, R., A. J. Rosakis and B. Moran, "A Three Dimensional Numerical Investigation of Fracture Initiation by Ductile Failue Mechanincs in a 4340 Steel", *International Journal of Fracture*, Vol. 56 (1), pp. 1-24, 1992.

34. Xia L. and C. F. Shih, "Ductile Crack Growth– Part I: A Numerical Study Using Computational Cells with Microstructurally-based Length Scales", *Journal of the Mechanics and Physics of Solids*, Vol. 43 (2), pp. 233-259, 1995.

35. Xia L. and C. F. Shih, "Ductile Crack Growth– Part II: Void Nucleation and

Geometry Effects on Macroscopic Fracture Behavior", *Journal of the Mechanics and Physics of Solids*, Vol. 43 (12), pp. 1953-1981, 1995.

36. Kuna, M. and D. Z. Sun, "Three-Dimensional Cell Model Analyses of Void Growth in Ductile Materials", *International Journal of Fracture*, Vol. 81, pp. 235-258, 1996.

37. Zhang, Z. L., "A Sensitivity Analysis of Material Parameters for the Gurson Constitutive Model", *Fatigue & Fracture of Engineering Materials & Structures*, Vol. 19(5), pp. 561-570, 1996.

38. Pardoen, T., I. Doghri and F. Delannay, "Experimental and Numerical Comparison of Void Growth Models and Void Coalescence Criteria for the Prediction of Ductile Fracture in Copper Bars", *Acta Materialia*, Vol. 46(2), pp. 541-552, 1998.

39. Wen, J. and K. C. Hwang, "Correction of the Gurson Yield Criterion", *Acta Mechanica Solida Sinica*, Vol. 15 (4), pp. 371-373, 2002.

40. Chu, C. C. and A. Needleman, "Void Nucleation Effects in Biaxially Stretched Sheets", *Journal of Engineering Materials and Technology - Transactions of the ASME*, Vol. 102, pp. 249-256, 1980.

41. Paulino, G. H., R. D. Carpenter, W. W. Liang, Z. A. Munir and J. C. Gibeling, "Fracture Testing and Finite Element Modeling of Pure Titanium", *Engineering Fracture Mechanics*, Vol. 68, pp. 1417-1432, 2001.

42. Samal, M. K., M. Seidenfuss, E. Roos, B. K. Dutta and H. S. Kushwaha, "Finite Element Formulation of a Newnonlocal Damage Model", *Finite Elements in Analysis and Design*, Vol. 44, pp. 358-371, 2008.

43. Peerlings, R. H. J., M. G. D. Geers, R. De Borst and W. A. M. Brekelmans, "A Critical Comparison of Nonlocal and Gradient-Enhanced Softening Continua", *International Journal of Solids and Structures*, Vol. 38, pp. 7723-7746, 2001.

44. Reusch, F., B. Svendsen and D. Klingbeil, "Local and Non-Local Gurson-Based

Ductile Damage and Failure Modelling at Large Deformation", *European Journal of Mechanics A/Solids*, Vol. 22, pp. 779-792, 2003.

45. Drabek, T. and H.J. Böhm, "Micromechanical Finite Element Analysis of Metal Matrix Composites Using Nonlocal Ductile Failure Models", *Computational Materials Science*, Vol. 37, pp. 29-36, 2006.

46. Lambros, J., M.H. Santare, H. Li and G. Sapna III, "A Novel Technique for the Fabrication of Laboratory Scale Functionally Graded Materials", *Experimental Mechanics*, Vol. 39, pp. 183-189, 1999.

47. Abanto-Bueno, J. and J. Lambros, "Mechanical and Fracture Behavior of an Artificially Ultraviolet-Irradiated Poly(ethylene-carbon monoxide) Copolymer", *Journal of Applied Polymer Science*, Vol. 92, pp. 139-148, 2004.

48. Tamura, I., Y. Tomota and H. Ozawa, "Strength and Ductility of Fe-Ni-C Alloys Composed of Austenite and Martensite with Various Strength", *Proceedings of the Third International Conference on Strength of Metals and Alloys*, Cambridge: Institute of Metals, Vol. 1, pp. 611-615, 1973.

49. Carpenter, R. D., W. W. Liang, G. H. Paulino, J. C. Gibeling and Z. A. Munir, "Fracture Testing and Analysis of a Layered Functionally Graded Ti/TiB Beam in 3-point Bending", *Materials Science Forum*, Vol.s 308-311, pp. 837-842, 1999.

50. Jeong, H.Y., "A New Yield Function and a Hydrostatic Stress-Controlled Void Nucleation Model for Porous Solids With Pressure-Sensitive Matrices", *International Journal of Solids and Structures*, Vol. 39, pp. 1385-1403, 2002.

51. Imanaka, M., Y. Nakamura, A. Nishimura and T. Iida, "Fracture Toughness of Rubber-Modified Epoxy Adhesives: Effect of Plastic Deformability of the Matrix Phase", *Composites Science and Technology*, Vol. 63, pp. 41-51, 2003.

52. Zaïri, F., M. Naït-Abdelaziz, K. Woznica and J.M. Gloaguen, "Constitutive Equa-

tions for the Viscoplastic-Damage Behaviour of a Rubber-Modified Polymer", *European Journal of Mechanics A/Solids*, Vol. 24, pp. 169-182, 2005.

53. Zaïri, F., M. Naït-Abdelaziz, K. Woznica and J.M. Lefebvre, "Modelling of the Elasto-Viscoplastic Damage Behaviour of Glassy Polymers", *International Journal of Plasticity*, Vol. 24, pp. 945-965, 2008.

54. Zaïri, F., B. Aour, J.M. Gloaguen, M. Naït-Abdelaziz and J.M. Lefebvre, "Steady Plastic Flow of a Polymer During Equal Channel Angular Extrusion Process: Experiments and Numerical Modeling", *Polymer Engineering and Science*, Vol. 48, pp. 1015-1021, 2008.

55. Challier, M., J. Besson, L. Laiarinandrasana and R. Piques, "Damage and fracture of polyvinylidene fluoride (PVDF) at 20°C: Experiments and Modelling", *Engineering Fracture Mechanics*, Vol. 73, pp. 79-90, 2006.

56. Laiarinandrasana, L., J. Besson, M. Lafarge and G. Hochstetter, "Temperature Dependent Mechanical Behaviour of PVDF: Experiments and Numerical Modelling, *International Journal of Plasticity*, Vol. 25, pp. 1301-1324, 2009.

57. Riku, I., K. Mimura and Y. Tomita, "Studies on Micro- to Macroscopic Mechanical Behavior of Porous Polymer under Compaction", *International Journal of Damage Mechanics*, Vol. 19, pp. 271-283, 2010.

58. Aoki, S., K. Amaya, M. Sahashi and T. Nakamura, "Identification of Gurson's Material Constants by Using Kalman Filter", *Computational Mechanics*, Vol. 19, pp. 501-506, 1997.

59. Corigliano, A., S. Mariani and B. Orsatti, "Identification of Gurson-Tvergaard Material Model Parameters via Kalman Filtering Technique. I. Theory", *International Journal of Fracture*, Vol. 104, pp. 349-373, 2000.

60. Mahnken, R., "Aspects on the Finite-Element Implementation of the Gurson Model

Including Parameter Identification", *International Journal of Plasticity*, Vol. 15, pp. 1111-1137, 1999.

61. Springmann, M. and M. Kuna, "Identification of Material Parameters of the Gurson-Tvergaard-Needleman Model by Combined Experimental and Numerical Techniques", *Computational Materials Science*, Vol. 33, pp. 501-509, 2005.

62. Springmann, M. and M. Kuna, "Determination of Ductile Damage Parameters by Local Deformation Fields: Measurement and Simulation", *Archive of Applied Mechanics*, Vol. 75, pp. 775-797, 2006.

63. Broggiato, G.B., F. Campana and L. Cortese, "Identification of Material Damage Model Parameters: An Inverse Approach Using Digital Image Processing", *Meccanica*, Vol. 42, pp. 9-17, 2007.

64. Schirrer, R., *Handbook of Materials Behavior Models*, J. Lemaitre (editor) In: Damage Mechanisms in Amorphous Glassy Polymers: Crazing, Section 6.12, Vol. 2, ISBN: 0-12-443343-X, Academic Press, USA, 2001.

65. Domininghaus, H., Plastic for Engineers: Materials, Properties and Applications. Munich: Hanser Gardner Publications, 1993.

66. Patel, J.K., *Digital Image Correlation for Microscale and Nanoscale Deformation Measurements*, M.S. Thesis, University of Illinois at Urbana-Champaign, USA, 2005.

67. Brocks, W., D. Z. Sun and A. Honig, "Verification of Micromechanical Models for Ductile Fracture by Cell Model Calculations", *Computational Materials Science*, Vol. 7, pp. 235-241, 1996.

68. Gao, X., J. Faleskog, C. F. Shih and R. H. Dodds, "Ductile Tearing in Part-Through Cracks: Experiments and Cell-Model Predictions", *Engineering Fracture Mechanics*, Vol. 59 (6), pp. 761-777, 1998.

69. Gullerud, A.S., X. Gao, R. H. Dodds and R. Haj-Ali, "Simulation of Ductile Crack Growth Using Computational Cells: Numerical Aspects", *Engineering Fracture Mechanics*, Vol. 60, pp. 65-92, 2000.

70. Faleskog, F., X. Gao and C. F. Shih, "Cell Model for Nonlinear Fracture Analysis - I. Micromechanics Calibration", *International Journal of Fracture*, Vol. 89, pp. 355-373, 1998.

71. Steglich, D. and W. Brocks, "Micromechanical Modelling of Damage and Fracture of Ductile Materials", *Fatigue & Fracture of Engineering Materials & Structures*, Vol. 21 (10), pp. 1175-1188, 1998.

72. Xia, L. and L. Cheng, "Transition from Ductile Tearing to Cleavage Fracture: A Cell-Model Approach", *International Journal of Fracture*, Vol. 87 (3), pp. 289-306, 1997.

73. Siegmund, T. and Brocks, W., "Prediction of the Work of Separation and Implications to Modeling", *International Journal of Fracture*, Vol. 99, pp. 97-116, 1999.

74. Anvari, M., Liu, J. and Thaulow, C., "Dynamic Ductile Fracture in Aluminum Round Bars: Experiments and Simulations", *International Journal of Fracture*, Vol. 143(4), pp. 317-332, 2007.

75. Benseddiq, N. and A. Imad, "A Ductile Fracture Analysis Using a Local Damage Model", *International Journal of Pressure Vessels and Piping*, Vol. 85, pp. 219-227, 2008.

76. Skallerud, B. and Z. L. Zhang, "A 3D Numerical Study of Ductile Tearing and Fatigue Crack Growth under Nominal Cyclic Plasticity", *International Journal of Solids and Structures*, Vol. 34(24), pp. 3141-3161, 1997.

77. Hill, R., *The Mathematical Theory of Plasticity*, Oxford Univ. Press, London, 1950.